Photoacoustic & Pulsed-Laser Doppler Monitoring of Blood Concentration and Perfusion in Tissue

_____

PHOTOACOUSTIC & PULSED LASER-DOPPLER MONITORING OF BLOOD CONCENTRATION AND PERFUSION IN TISSUE

PROEFSCHRIFT

ter verkrijging van
de graad van doctor aan de Universiteit Twente,
op gezag van de rector magnificus,
prof. dr. F.A. van Vught,
volgens besluit van het College voor Promoties
in het openbaar te verdedigen
op vrijdag 6 december 2002 te 16.45 uur.

door

Roy Gerardus Maria Kolkman
geboren op 22 juli 1974
te Lichtenvoorde

Dit proefschrift is goedgekeurd door

de promotor: prof. dr. J. Greve

de assistent-promotor: dr. ir. F.F.M. de Mul

Contents

1 Introduction

In this chapter an overview of photoacoustic signal generation and laser Doppler flowmetry is given. Both methods are described, together with an overview of clinical applications. The purpose of the research is given, followed by an outline of this thesis.

1.1 General Introduction

In this thesis two non-invasive biomedical-optic methods are described: laser Doppler flowmetry (LDF) and photoacoustics (PA). These methods reveal information about the blood flow and blood content, respectively, in situations that require continuous (bedside) monitoring.

Information about blood flow or blood content can also be obtained with methods like ultrafast computed tomography (CT), magnetic resonance imaging (MRI) or single-photon emission computed tomography (SPECT).[1] However, these methods cannot easily be applied in bedside monitoring. Information about blood flow can also be acquired with Doppler ultrasound. This technique is limited in the Doppler assessment of low velocity and low volume blood flows, as the Doppler effect from solid tissue motion is stronger than of the flowing blood and echoes from the small blood volumes are too weak. A promising development is grey-scale harmonic imaging in ultrasound. This method makes use of ultrasound contrast agents (UCA), consisting of microbubbles (e.g. Levovist™, SonoVue™, Optison™), to obtain information about the perfusion. Qualitative assessment of the perfused areas is possible with UCA bolus injection, analyzing the wash-out curve.[2] Another approach is to use a continuous infusion of UCA, providing a steady state. The reappearance rate after microbubble destruction by ultrasound energy gives information about the mean tissue microbubble velocity, correlating with the flow rate within the tissue (refill kinetics).[3,4,5] As these methods require the use of contrast agents, they cannot be applied during continuous monitoring.

Laser Doppler flowmetry is commonly used to obtain information about the microvascular blood flow in tissue.[6,7,8] Photoacoustics is a rather new technique, which can be used to image the absorbing, blood containing, compartments inside the tissue.[9]

This chapter first gives an introduction into the background of photoacoustics, together with current applications and ongoing developments using photoacoustics. Then, laser Doppler flowmetry will be introduced, followed by the objective of this research. Finally the outline of this thesis will be described.

1.2 Photoacoustics

The term photoacoustics or optoacoustics refers to the generation of acoustic waves by modulated optical radiation. Both terms have the same meaning and are in common usage. Photoacoustics can also be used in a broader sense, as it refers to generation of acoustic waves by any type of energetic radiation (including electromagnetic radiation from radiofrequency to X-ray, electrons, protons, ions and other particles).[10] A.G. Bell discovered the

photoacoustic effect in 1880.[11] He observed an audible sound generated by chopped sunlight, incident on absorbing materials. Although this effect has been known for already more than a century, the development of lasers and other high energy light sources (such as arc lamps), during the last few decades, caused a renewed interest in the photoacoustic effect.

There are two effects that are closely related to photoacoustic signal generation, which are sonoluminescence (reverse PA effect) and the inverse photoacoustic effect. Sonoluminescence is a process where single bubbles of gas or vapour emit light once they are trapped in sufficiently intense acoustic fields.[12] The inverse photoacoustic effect is the generation of sound due to radiation being *lost* from the sample instead of being deposited in the sample, as in the usual PA effect. This radiation loss can be achieved by exposing the sample to a surface at a lower temperature. While modulating this exposure, sound is generated inside the sample.[13]

Most photoacoustic generation is due to deposition of heat by light, the so-called photothermal effect. Other mechanisms of photoacoustic generation are possible as well.[10] Some of these mechanisms are listed below, in order of increasing efficiency (= acoustic energy generated / light energy absorbed):

Electrostriction is the effect where the volume of the sample changes proportional to the optical intensity. The electric field associated with the light causes a decrease in relative electric permittivity, resulting in a movement of molecules towards regions with higher optical intensity. An acoustic transient is generated when molecules move into these regions.

Thermal expansion is a mechanism where absorption of light in a restricted volume is followed by thermal relaxation. For pulsed photoacoustic excitation, the ratio of electrostrictive pressure over thermal expansion pressure in typical liquids like water or ethanol is[10]

$$\frac{|P_{el}|}{|P_{th}|} \leq \frac{10^{-12}}{\mu_a \tau_a} \tag{1.1}$$

with μ_a the optical absorption coefficient [mm^{-1}] and τ_a the pulse duration of the acoustic signal [sec]. The contribution of electrostrictive pressure can be neglected in most cases, except when the absorption of the sample is very low. The efficiency of electrostrictive and thermal expansion[10] is typically in the order of 10^{-12} to 10^{-8}.

Photochemical effect is the effect where light induces formation or dissociation of molecules, which produces acoustic waves due to volumetric changes

Vaporization or ablation: when in liquids the deposited energy causes a temperature rise above the boiling temperature, vaporization will occur. The efficiency of the photoacoustic generation will increase when the boiling temperature is achieved, since the thermal expansion coefficient of vapor is larger

than that of liquid. In solids the material can melt and vaporization or ablation can occur.

Dielectric breakdown, optical breakdown or plasma formation: at high laser intensities, with the electric field strength exceeding the insulation threshold of the medium, an electrical discharge will occur. The breakdown, which is accompanied by plasma formation, generates a shock wave. This effect is the most efficient photoacoustic generation and can have efficiencies up to 30%.

Thermal expansion is most suitable for non-invasive tissue imaging, as it is non-destructive, while the last three above-mentioned mechanisms induce changes in the sample. The difference in absorption between tissue-constituents and the tissue itself can be used to reveal information about these constituents. A well-known absorber in tissue is blood (hemoglobin), which enables localization and monitoring of blood content in tissue, using photoacoustics.

The generation of photoacoustic waves can be done with two types of excitation: continuous wave (CW) modulation or pulsed excitation.[10] CW modulation uses modulated light (near 50% duty cycle, usually 10^0-10^3 Hz) to generate acoustic waves. Analysis is typically carried out in frequency domain. Pulsed excitation uses pulsed (very low duty cycle, typical pulse-width ≤ 1 μs) light, with high peak powers. Analysis is usually carried out in time-domain. The efficiency is higher for pulsed than for modulated photoacoustic generation. In this thesis we will use pulsed photoacoustic generation to reveal information about the blood content in tissue.

In the next paragraph the most commonly used mechanism to generate photoacoustic signals in tissue is explained. Subsequently an overview of various applications of photoacoustics in tissue will be given.

1.2.1 Biomedical photoacoustics

In pulsed biomedical-photoacoustics a light pulse heats absorbers inside the tissue, producing a temperature rise proportional to the deposited energy. The light pulse is so short that the heating of the absorber occurs instantaneously without expansion (adiabatic heating), resulting in a pressure rise. The resulting pressure wave (acoustic wave) will propagate through the tissue and can be detected at the tissue surface. The distance from the photoacoustic source to the detector can be determined by measuring the time between generation of the acoustic wave (determined by the light pulse) and the arrival of the acoustic wave at the tissue surface, using the speed of sound in tissue. In case of stress confinement, where the laser pulse duration is much shorter compared to the time of stress propagation through the acoustic source, the initially generated pressure rise can be described by[14]

$$P = \frac{\beta v^2}{c_p} \Phi \mu_a = \Gamma \Phi \mu_a \qquad (1.2)$$

where β [K^{-1}] is the thermal expansion coefficient, v [m/s] the speed of sound, c_p [J kg^{-1} K^{-1}] the specific heat capacity at constant pressure, Φ [mJ/m^2] the fluence rate at the location of the absorber, and μ_a [mm^{-1}] the absorption coefficient. The efficiency of photoacoustic excitation is given by the dimensionless quantity Γ, called the Grüneisen coefficient. This simple expression shows that the acoustic wave contains information about the optical properties of the photoacoustic source. As mentioned above, this equation requires stress-confinement, which is fulfilled for light pulse durations of several nanoseconds for typical absorption coefficients (e.g. of blood, melanine) and velocities of sound in tissue.

1.2.2 Clinical applications

High-resolution 3D imaging

Hoelen et al. have applied photoacoustics to 3D-image artificial blood vessels, with sub millimeter sizes, in real tissue samples, with high resolution,[9,15,16,17] using 532 nm light pulses with a typical duration of about 10 ns. While scanning a sensor over the tissue surface, photoacoustic time traces were recorded. A 3D-photoacoustic reconstruction of blood vessels was calculated using a synthetic beam-forming algorithm. Absorbing structures, down to a depth of 10 mm, have been imaged with a resolution in depth of 20 μm. The lateral resolution depends on the detection geometry and is limited by its detector diameter to about 200 μm. Besides artificial blood vessels, also other absorbing structures like 10 μm diameter carbon fibres[9,16] and human hairs[17,18] have been imaged, proving the above mentioned resolution. Using the same kind of set-up and imaging algorithm, Pilatou et al. have recently presented a photoacoustic reconstruction of the cast of a branched epigastic artery of a wistar rat, surrounded by a tissue-like medium.[19,20] This shows that photoacoustics is able to image such complex structures.

Tumor detection

Development of tumors creates a micro-vascular network inside and around the affected area (angiogenesis). This can be used for photoacoustic detection and localization of these tumors.

Oraevsky et al. have developed a laser optoacoustic imaging system (LOIS) for breast cancer detection.[21,22] Their system consists of a 32-element arc-shaped transducer array. The resolution of the system is about 0.4 mm in depth, and 1-2 mm lateral, depending on the position relative to the transducer array. Optical inhomogeneities (tumors) with millimeter sizes, have been imaged in

phantoms as well as *in vivo* on a human breast containing tumors, using a wavelength of 1064 nm. In phantom measurements in a material with optical properties resembling those of breast tissue (μ_{eff}=0.14 mm^{-1}), a 2 mm blood vessel at a depth of 7.5 cm could be detected.

Kruger et al. are applying radiofrequency (434 MHz) waves to generate photoacoustic signals in their thermoacoustic tomographic (TCT) device for breast cancer screening.[23,24,25] They conducted a pilot study of 78 patients.[25] It appeared that TCT image quality was dependent on both patient age and breast "density", improving with increasing breast density and decreasing patient age. Most cysts seen on ultrasound were visualized with TCT as well, but only four of seven cancers were visualized, which was attributed to inadequate image quality. With future improvements of the TCT scanner, it is expected to overcome these technical difficulties.

Besides the LOIS system for mammography, Oreavsky et al. have also constructed a confocal optoacoustic transducer (COAT),[22] which is able to image layered tissue structures with an axial (depth) resolution of 18 μm and a lateral resolution of 60 μm, up to a depth of 600 μm, using 10-12 ns light pulses at 1064, 532 and 355 nm. This system has been applied to detect structural changes in mucosal tissue. Recent studies confirmed the feasibility of the COAT to differentiation of normal mucosa from cancerous, and in characterisation of early stages of squamous cell carcinoma in an animal model.

Port wine stains

Viator et al. have developed a probe for port wine stain depth determination.[26] Treatment of port wine stains is aimed at photothermal coagulation of the port wine stain vessels, without causing epidermal damage. When the depth of port wine stains is known, laser treatment can be optimised, using e.g. cryogen spray cooling of the epidermal melanin layer. They have shown that their system is able to determine port wine stain depth in human skin up to 570 μm, using 4 ns laser pulses at 532 nm. Based on signal to noise considerations the authors have estimated that their probe can be used to probe human skin deeper than a millimeter, which is sufficient for most port wine stains.

Layered tissue structures

Paltauf et al. together with Frenz et al. have studied layered tissue structures.[27,28,29] Images of biological tissues *in vivo* have been generated by scanning an annular detector over the tissue surface.[27] Using tunable laser light (500-600 nm) with a pulse-duration of 5 ns, skin structures like epidermis, blood capillaries and deeper blood vessels could be localized and identified by their spectral characteristics. Furthermore, a value for the oxygenation of blood in capillaries has been estimated.

Karabutov et al. have imaged layered structures like chicken cockscomb, and human hand.[30] Using the chicken cockscomb as a model for human vascular lesions such as port wine stains, different layers could be visualized using photoacoustics. Measurements at the human arm showed time traces from which different layers could be distinguished as well.

Our group has presented images of the fingernail as well as images of tissue-structures above bone.[19] We were able to detect tissue thickness above bone, using the reflection of the direct signal from the skin at the bone surface.

Tissue coagulation

Laser treatment of tissue becomes a more common tool in minimal invasive surgery. The control of this treatment can be carried out monitoring/measuring the tissue coagulation.

Köstli et al. have shown that it is possible to detect coagulation of tissue.[29] Using photoacoustics at a wavelength of 532 nm with 8 ns pulses, they imaged the effect of coagulation on a piece of chicken breast tissue by scanning an annular transducer over the tissue surface, before and after coagulation.

Karabutov et al. also showed changes in photoacoustic signals before and after coagulation of *in vitro* chicken breast covered with skin, using a wavelength of 532 nm.[30] A larger photoacoustic signal was observed after coagulation of the muscle, which is explained by increased scattering in the tissue due to coagulation, causing a larger amount of light to be absorbed.

Oberheide et al. developed a system to localize the ciliary body in the eye, which is located in the anterior part of the eye below the sclera.[31,32] This part is of importance for treatment of glaucoma, where the ciliary body is coagulated. They have localized the ciliary body in porcine and rabbit eyes with photoacoustics, using a wavelength in the near infrared spectral range (800-1064nm). After coagulation, the point of coagulation in the ciliary body could be detected.

Esenaliev et al. have shown that the photoacoustic technique is sensitive to changes in optical properties and speed of sound induced by coagulation or freezing of *in vitro* canine liver slabs, using 1064 nm light pulses.[33] Furthermore, a photoacoustic system has been developed to monitor temperature changes during thermotherapy to control boundaries of hyperthermia or coagulation in diseased tissue, and to minimize damage to surrounding normal tissues.[34,35]

Burn depth estimation

Sato et al. have studied burn wound depth in a rat model using photoacoustics.[36] They were able to distinguish between deep burn, deep dermal burn and healthy skin. Information related to the depth of injury could be obtained from the photoacoustic time signals, generated by 500 nm light pulses, with a pulse-duration of 4-6 ns.

Glucose monitoring

The group of Oraevsky has studied the detection of glucose *in vivo*.[37] As the optical scattering coefficient of tissue changes as a result of changing glucose concentration, the effective optical attenuation coefficient changes as well. The measured photoacoustic transient contains information about the effective attenuation coefficient, which reflects the glucose concentration. Measurements *in vivo* in the sclera of a rabbit eye showed that changes in glucose concentration could be detected using photoacoustics.

Zhao et al. used the change in reduced scattering coefficient of the blood to determine the glucose concentration with photoacoustics.[38] The change in scattering coefficient influences the photoacoustic signal. Using a cuvet with flowing blood, they measured the photoacoustic signals for various glucose concentrations. The signals were generated using a 905 nm laserdiode, producing 160 ns pulses. An almost linear relationship between the amplitude of the photoacoustic signal and the glucose concentration has been observed. The minimal detectable concentration was about 100 mg/100 ml, whereas the normal concentration of glucose in human tissue varies between 70-110 mg/100 ml.[39] So the sensitivity of this system has to be improved.

Tissue optical properties

The group of Oraevsky has applied photoacoustics to determine optical properties of turbid media.[14,40] As the temporal course of the photoacoustic signal is determined by the optical absorption coefficient and the spatial distribution of light fluence in the medium, information about the optical properties is included in the signal. The effective optical attenuation coefficient and reduced optical scattering coefficient could be determined in weakly absorbing turbid media, when the efficiency of photoacoustic generation (Grüneisen coefficient) is known.

Endoscopy

Jacques et al. developed a photoacoustic probe to image tissue blanching during photodynamic therapy (PDT) of oesophageal cancer.[41,42] Photodynamic therapy is a light activated chemotherapy where light activates a photosensitive drug to cause damage to a target tissue such as in a tumor. PDT treatment results in a blanched, necrotic layer of cancerous tissue over a healthy, deeper layer of perfused tissue. The photoacoustic probe can be used to determine the thickness of the blanched tissue, which corresponds to PDT-treatment depth. This depth has been measured in phantoms with a photoacoustic probe, consisting of a fiber for light delivery of 532 nm pulses (photoacoustic generation), and a piezofilm for detection of the acoustic transients. The probe has a diameter less than 2.5 mm, so it fits within the lumen of an endoscope.

The group of Mills has developed an all optical, fiber, photoacoustic sensor using a miniature Fabry-Perot interferometer, bonded to a fiber-end.[43,44] Its

small size enables endoscopic as well as intravascular applications. Besides measuring acoustic waves, it is also sensitive to temperature changes and can be used as a photothermal probe as well.[43,45]

Oxygenation of blood

As the optical absorption of blood is dependent on the wavelength as well as on oxygenation level, the oxygenation can in principle be determined using photoacoustic spectroscopy (excitation at different wavelengths).

Fainchtein et al. determined relative changes in the concentration of oxy- and de-oxyhemoglobin by pulsed photoacoustic spectroscopy in a wavelength range from 710-890 nm.[46,47]

Paltauf et al. have shown that estimation of the oxygenation of blood in capillaries is possible. They used a tuneable laser providing 5 ns pulses in the wavelength range from 500-600 nm.[27]

Imaging using an optical detection system

The group of Frenz together with the group of Paltauf has developed an optical detection system for photoacoustic signals.[48] Their detection system is based on pressure-induced changes of optical reflectance at a glass-liquid interface, imaged with a time-gated video camera. With this system blood vessels embedded in a piece of cartilage tissue have been imaged, with a lateral resolution of 200 μm and a depth resolution of 20 μm.[49,50]

Beard et al. used a sensing mechanism based upon the detection of acoustically-induced variations in the optical thickness of a Fabry Perot polymer film interferometer.[51] As the film is optically addressed, the spot of the interferometer laser beam determines the size of the acoustic sensor elements. With this system, absorbing structures in a tissue phantom were imaged.[52]

Enhancing contrast

The group of Oreavsky is studying the use of absorbing nanoparticles to enhance the optoacoustic tissue contrast.[53,54] The nanoparticles are chosen such that, after absorption of light, evaporation will occur. This evaporation will take place only at extremely small absorbing centers (nanoparticles), with no more than 1 degree temperature rise to avoid damage to the tissue. Based on theoretical estimations, an enhancement of the contrast up to three orders in magnitude is expected. In phantom experiments an enhancement of contrast could be obtained when these nanoparticles were heated up to evaporation.

1.3 *Laser Doppler Flowmetry (LDF)*

In 1975 Stern[55] described an instrument to assess *in vivo* the microcirculation in tissue, using the Doppler effect. When coherent light is scattered in tissue, a part of the light will be scattered by moving red blood cells causing a frequency shift Δf, called Doppler shift. This Doppler shift is dependent on the velocity of the moving red blood cells:

$$\Delta f = \frac{2vn}{\lambda_0}\cos\theta \tag{1.3}$$

where v is the velocity of the moving red blood cell, n is the refractive index of the medium, λ_0 is the wavelength of the incident light, and θ is the angle between the direction of incidence of the photon on the red blood cell and the direction of scattering. The frequency broadened light, together with light scattered from static tissue, mixes on the detector. This mixing causes intensity fluctuations with Doppler frequencies. Information about the velocity of the moving red blood cells can be obtained by analyzing the photocurrent. As light is scattered in all directions in tissue, not one single Doppler frequency will be obtained, but a whole spectrum. The spectral power density $S(\omega)$ of the photocurrent, with the angular frequency ω defined as $\omega=2\pi f$, gives information about the moving red blood cells. The moments M_i or weighted moments $M_{i,w}$ of the spectral power density are used to characterize $S(\omega)$:

$$M_i = \int_a^b \omega^i S(\omega)d\omega \tag{1.4}$$

$$M_{i,w} = \frac{M_i}{M_0} \tag{1.5}$$

where a and b are the low and high cut-off frequencies. Typical values are about 20-50 Hz for the low cut-off frequency, minimizing the effect of bulk motion of the tissue relative to the probe, and 20-30 kHz for the high cut-off frequency in case of measurements on the microcirculation of human skin.

Bonner and Nossal[56] have shown that the weighted first moment is proportional to the root-mean-square (rms) velocity of the red blood cells:

$$\sqrt{\langle v^2 \rangle} \sim M_{1,w}. \tag{1.6}$$

Furthermore, the average concentration of moving red blood cells is proportional to the zero order moment M_0, provided this concentration is small. The first moment M_1 is proportional to the perfusion, defined as the product of average red blood cell velocity times concentration. In general the perfusion is defined as blood volume flow per unit time and unit of tissue mass (e.g. ml/min per 100 gr. tissue).

Based on this principle, laser Doppler flowmetry (LDF) instruments have been developed.[57,58] Currently, in Europe the three main manufacturers of LDF instruments are Perimed AB, Moor Instruments Ltd, and Oxford Optronix Ltd. In all these instruments fibers are used for light delivery to the tissue, as well as for detection of the (Doppler-) scattered light. As movement of the fibers introduces artifacts in the measurements, de Mul et al. have developed an integrated probe consisting of a laserdiode and a photodetector.[59] Recently this has been miniaturized into a fully integrated optoelectronic chip probe by Serov et al.[7,60]

Besides perfusion monitoring, also laser Doppler imaging (LDI) has been developed.[61,62,63,64] In this case a scanning laser beam is used to map the perfusion at different spots of the tissue. Without any mechanical contact with the tissue, these systems provide an image showing a perfusion map providing information about the perfusion in different areas of the tissue. Recently Serov et al.[7,65] demonstrated the use of a CMOS-camera to image the perfusion. Using an expanded beam, illuminating a large area, it is no longer necessary to scan the laser beam over the tissue surface. Advantages of this system are that there is no need for mechanical movement. Also the perfusion map can be obtained together with a normal photo of the tissue, using the same camera.

The above-mentioned LDF methods do not provide information about the depth inside the tissue from which the signals stem, or over which volume it is averaged. Information about perfusion for different path-lengths of the light in the tissue can be obtained using path-length-resolved low coherence Doppler interferometry, as described by Petoukhova et al.[8,66,67]

In the next paragraph we will give an overview of some clinical applications of laser Doppler flowmetry.

1.3.1 Clinical applications

Laser Doppler flowmetry has been introduced in the medical field during the eighties. Research is still going on to improve the method and instruments. This is very different from photoacoustics, which is a relatively new technique that still is being developed.

Sheperd and Öberg[6] have given an extensive review of laser Doppler flowmetry describing the instrument as well as applications. A short overview of some main applications is given below.[6]

In pharmacology and anaesthesiology LDF is used to monitor the effect of drugs or anaesthetic agents on blood perfusion. These effects include sympathetic blockade and changes in peripheral blood perfusion.

In dermatology skin irritation in patch tests or in erythematous diseases can be determined by visual inspection. The result is then heavily dependent on the examiner's experience, and the subjects skin color and skin type. The degree

of irritation can however be quantitatively determined if one measures with LDF the skin perfusion.

The success of transplantation of a skin flap in plastic surgery is dependent on adequate blood supply. LDF can provide helpful information in these situations as it gives an early sign of microcirculation failure. In plastic surgery LDF can also be used to distinguish deep burns from superficial burns, so that the treatment can be adapted to the type of burn. Another application in plastic surgery is the monitoring of wound healing.

In neurosurgery, information about brain microcirculation can be obtained measuring directly on the dura or by using implantable probes. Monitoring the microcirculation during and after surgery can be helpful for detection of impaired circulation. Early treatment of this impaired circulation may minimize brain damage.

1.4 *Purpose of the research*

Many children are born prematurely in the Netherlands, i.e. after a pregnancy of 37 weeks or shorter. Those who survive have a high risk to develop a handicap, varying from a severe psychomotoric handicap (e.g. cerebral palsy) to educational and behavioral problems during adolescence. This is most likely caused by cerebral damage due to hemorrhage (internal bleeding) or hypoxic-ischemic injury related to perturbation of cerebral hemodynamics and/or oxygenation in the perinatal period (from about 22 weeks of pregnancy till the first 28 days after delivery).[68]

Local monitoring of perfusion, oxygenation and blood volume can provide important information for preventive treatment of those children. The same holds for detection of not optimally perfused brain tissue in full-term or near-term neonates at-risk (e.g. those born asphyxiated).

Monitoring of *changes* in oxygenation is possible using near-infrared spectroscopy (NIRS).[68] In this thesis the feasibility of using photoacoustics to localize and monitor blood content will be explored. This requires the development of a photoacoustic probe in which both the illumination system as well as acoustic sensors are integrated. Furthermore we will make adaptations to the laser Doppler system, to make it suitable for measurement of perfusion in the neonatal brain. Evaluation of the combination of NIRS, photoacoustics and LDF is carried out in close cooperation with the University Medical Center Nijmegen.

1.5 Outline of this thesis

This first introductory chapter gives an overview of photoacoustic generation and laser Doppler flowmetry. Both methods are described, together with an overview of clinical applications. The purpose of the research is given.

In the second chapter first a background on detection of photoacoustic waves is given. Then the design of the photoacoustic sensor is described followed by the construction of the sensor. The calculated detector characteristics are compared with measurements.

In the third chapter measurements with the photoacoustic sensor are presented. 2D photoacoustic reconstructions of cross-sections of artificial blood vessels are shown. The algorithm used to reconstruct these cross-sections is explained. Results from *in-vivo* imaging in a rabbit ear and human arm are presented. Furthermore the ability of photoacoustics to monitor changes in vessel size ("blood content") is demonstrated.

In chapter four we describe the design of the pulsed laser Doppler flowmetry system. Measurements are presented in which pulsed and continuous wave laser Doppler are compared. The maximum achievable depth is predicted using phantom measurements and Monte-Carlo simulations.

In the fifth chapter the results of a combined measurement of the circulation in the brain of a piglet, using near-infrared spectroscopy, laser Doppler flowmetry and photoacoustics are shown.

In chapter six the complementarity of photoacoustics, near-infrared spectroscopy, and laser Doppler flowmetry is discussed. A possible design for a combined probe is presented.

In the last chapter the final conclusions of the work presented in this thesis will be drawn. We will quote future applications and potentials of the described methods.

1.6 References

1. S. Webb, "The physics of medical imaging", Institute of Physics Publishing, Bristol and Philadelphia, 1988.
2. L. Claassen, G. Seidel, and C. Algermissen, "Quantification of flow rates using harmonic gray-scale imaging and an ultrasound contrast agent: an in vitro and in vivo study", *Ultrasound in Med. & Biol.*, vol. 27, pp. 83-88, 2001.
3. G. Seidel, L. Claassen, K. Meyer, and M. Vidal-Langwasser, "Evaluation of blood flow in the cerebral microcirculation: analysis of the refiill kinetics during ultrasound contrast agent infusion", *Ultrasound in Med. & Biol.*, vol. 27, pp. 1059-1064, 2001.

4. G. Seidel, K. Meyer, V. Metzler, D. Toth, M. Vida-Langwasser, and T. Aach, "Human cerebral perfusion analysis with ultrasound contrast agent constant infusion: a pilot study on healthy volunteers", *Ultrasound in Med. & Biol.*, vol. 28, pp. 183-189, 2002.

5. K. Wei, A.R. Jayaweera, S. Firoozan, A. Linka, D.M. Skyba, S. Kaul, "Quantification of myocardial blood flow with ultrasound-induced destruction of microbubbles administered as a constant venous infusion", *Circulation*, vol. 97, pp. 473-483, 1998.

6. A.P. Sheperd, and P.Å. Öberg, "Laser-Doppler Blood Flowmetry", Kluwer Academic Publishers, Dordrecht, 1990.

7. A. Serov, "Novel instruments for remote and direct-contact laser Doppler perfusion imaging and monitoring", *Ph.D. Thesis*, University of Twente, Enschede, 2002.

8. A.L. Pethoukhova, "Path-length-resolved low coherence Doppler interferometry and standardization of traditional laser Doppler perfusion monitors for clinical use", *Ph.D. Thesis*, University of Twente, Enschede, 2002.

9. C.G.A. Hoelen, F.F.M. de Mul, R. Pongers, and A. Dekker, "Three-dimensional photoacoustic imaging of blood vessels in tissue", *Optics Letters*, vol. 23, 1998.

10. A.C. Tam, "Applications of photoacoustic sensing techniques", *Rev. Mod. Phys.*, vol. 58, pp. 381-431, 1986.

11. A.G. Bell, "On the production and reproduction of sound by light", *Am. J. Sci.*, vol. 20, pp. 305-324, 1880.

12. L.A. Crum, and R.A. Roy, "Sonoluminescence", *Science*, vol. 266, pp. 233-234, 1994.

13. R.B. Steward, S.M. Didascalou, and G.J. Diebold, "The inverse optoacoustic effect: sound generation through emission of blackbody radiation", *Optics Communications*, vol. 58, pp. 103-107, 1986.

14. A.A. Oraevsky, S.L. Jacques, and F.K. Tittel, "Measurement of tissue optical properties by time-resolved detection of laser-induced transient stress", *Applied Optics*, vol. 36, pp. 402-415, 1997.

15. C.G.A. Hoelen, and F.F.M. de Mul, "Image reconstruction for photoacoustic scanning of tissue structures", *Applied Optics*, vol. 39, pp. 5872-5883, 2000.

16. C.G.A. Hoelen, "3-D photoacoustic tissue imaging – towards non invasive medical photoacoustic diagnosis", *Ph.D. Thesis*, University of Twente, Enschede, 1998.

17. C.G.A. Hoelen, R.G.M. Kolkman, M. Letteboer, R. Berendsen, and F.F.M. de Mul, "Photoacoustic tissue scanning (PATS)", in *Optical Tomography and Spectroscopy of Tissue III*, B. Chance, R.R. Alfano, and B.J. Tromberg Eds., Proc. SPIE vol. 3597, pp. 352-363, 1999.

18. R.G.M. Kolkman, C.G.A. Hoelen, M.M.J. Letteboer, R.C.M. Berendsen, and F.F.M. de Mul, "Photoacoustic mapping of hidden tissue structures", in *Biomedical Optics: New Concepts in Therapeutic Laser Applications, Novel Biomedical Optical Spectroscopy, Imaging, and Diagnosis, Advances in Optical Imaging, Photon Migration and Tissue Optics*, OSA Technical Digest, pp. 239-241, 1999.

19. M.C. Pilatou, R.G.M. Kolkman, E. Hondebrink, R.A. Bolt, and F.F.M. de Mul, "Photoacoustic imaging of blood perfusion in tissue and phantoms", in *Biomedical Optoacoustics II*, A.A. Oraevsky Ed., Proc. SPIE vol. 4256, pp. 28-33, 2001.

20. M.C. Pilatou, N. Voogd, F.F.M. de Mul, E. Marani, and L.N.A. van Adrichem, "Photoacoustic imaging in phantom materials and *in vivo*", in *Hybrid and Novel Imaging and New Optical Instrumentation for Biomedical Applications*, A. Bocarra, A.A. Oraevsky Eds., Proc. SPIE vol. 4434, pp. 96-98, 2001.

21. A.A. Oraevsky, A.A. Karabutov, S.V. Solomatin, E.V. Savateeva, V.G. Andreev, Z. Gatalica, H. Singh, and R.D. Fleming, "Laser optoacoustic imaging of breast cancer *in vivo*", in *Biomedical Optoacoustics II*, A.A. Oraevsky Ed., Proc. SPIE vol. 4256, pp. 6-15, 2001.

22. A.A. Karabutov, V.G. Andreev, B. Bell, R.D. Fleming, Z. Gatalica, M. Motamedi, E.V. Savateeva, H. Singh, S.V. Solomatin, S.L. Thomsen, P.M. Henrichs, and A.A. Oraevsky, "Optoacoustic images of early cancer in forward and backward modes", in *Hybrid and Novel Imaging and New Optical Instrumentation for Biomedical Applications*, A. Bocarra, A.A. Oraevsky Eds., Proc. SPIE vol. 4434, pp. 13-27, 2001.

23. R.A. Kruger, K.D. Miller, H.E. Reynolds, W.L. Kiser, Jr., D.R. Reinecke, and G.A. Kruger, "Breast cancer *in vivo*: Contrast enhancement with thermoacoustic CT at 434 MHz – feasibility study", *Radiology*, vol. 216, pp. 279-283, 2000.

24. R.A. Kruger, W.L. Kiser, Jr., K.D. Miller, and H.E. Reynolds, "Thermoacoustic CT: Imaging Principles", in *Biomedical Optoacoustics*, A.A. Oraevsky Ed., Proc. SPIE vol. 3916, pp. 150-159, 2000.

25. R.A. Kruger, and W.L. Kiser, Jr., "Thermoacoustic CT of the breast: Pilot study observations", in *Biomedical Optoacoustics II*, A.A. Oraevsky Ed., Proc. SPIE vol. 4256, pp. 1-5, 2001.

26. J.A. Viator, G. Au, G. Paltauf, S.L. Jacques, S.A. Prahl, H. Ren, Z. Chen, and J.S. Nelson, "Clinical testing of a photoacoustic probe for port wine stain depth determination", *Lasers Surg. Med.*, vol. 30, pp. 141-148, 2002.

27. G. Paltauf, K.P. Köstli, D. Frauchiger, and M. Frenz, "Spectral optoacoustic imaging using a scanning transducer", in *Hybrid and Novel*

Imaging and New Optical Instrumentation for Biomedical Applications, A. Bocarra, A.A. Oraevsky Eds., Proc. SPIE vol. 4434, pp. 81-88, 2001.

28. G. Paltauf, and H. Schmidt-Kloiber, "Pulsed optoacoustic characterization of layered media", *J. Appl. Phys.*, vol. 88 (3), pp. 1624-1631, 2000.

29. K.P. Köstli, M. Frenz, H.P. Weber, G. Paltauf, and H. Schmidt-Kloiber, "Pulsed optoacoustic tomography of soft tissue with a piezoelectric ring sensor", in *Biomedical Optoacoustics*, A.A. Oraevsky Ed., Proc. SPIE vol. 3916, pp. 67-74, 2000.

30. A.A. Karabutov, E.V. Savateeva, and A.A. Oraevsky, "Imaging of layered structures in biological tissues with opto-acoustic front surface transducer", in *Laser-Tissue Interaction X*, S.L. Jacques Ed., Proc. SPIE vol. 3601, pp. 284-296, 1999.

31. U. Oberheide, B. Jansen, I. Bruder, H. Lubatschowski, and H. Welling, "Optoacoustic online control for laser cyclophotocoagulation", in *Biomedical Optoacoustics II*, A.A. Oraevsky Ed., Proc. SPIE vol. 4256, pp. 53-60, 2001.

32. U. Oberheide, B. Jansen, I. Bruder, H. Lubatschowski, and H. Welling, "Optoacoustic imaging for ophthalmology", in *Hybrid and Novel Imaging and New Optical Instrumentation for Biomedical Applications*, A. Bocarra, A.A. Oraevsky Eds., Proc. SPIE vol. 4434, pp. 1-7, 2001.

33. R. Esenaliev, I. Larina, K. Larin, and M. Motamedi, "Real-time optoacoustic monitoring during thermotherapy", in *Biomedical Optoacoustics*, A.A. Oraevsky Ed., Proc. SPIE vol. 3916, pp. 302-310, 2000.

34. R.O. Esenaliev, A.A. Oraevsky, K.V. Larin, I.V. Larina, and M. Motamedi, "Real-time optoacoustic monitoring of temperature in tissues", in *Laser-Tissue Interaction X*, S.L. Jacques Ed., Proc. SPIE vol. 3601, pp. 268-276, 1999.

35. K. Larin, I. Larina, M. Motamedi, and R. Esenaliev, "Monitoring of temperature distribution in tissues with optoacoustic technique real tissue", in *Biomedical Optoacoustics*, A.A. Oraevsky Ed., Proc. SPIE vol. 3916, pp. 311-321, 2000.

36. S. Sato, T. Shimeda, T. Arai, M. Kikuchi, M. Obara, and H. Ashida, "Measurement of photoacoustic signals from skin: Potential application to burn depth estimation", in *Hybrid and Novel Imaging and New Optical Instrumentation for Biomedical Applications*, A. Bocarra, A.A. Oraevsky Eds., Proc. SPIE vol. 4434, pp. 8-12, 2001.

37. A. Bednov, A. Karabutov, E. Savateeva, W. March, and A. Oraevsky, "Glucose monitoring *in vivo* by measuring laser-induced acoustic profiles", in *Biomedical Optoacoustics*, A.A. Oraevsky Ed., Proc. SPIE vol. 3916, pp. 9-18, 2000.

38. Z. Zhao, and R. Myllyla, "Photoacoustic determination of glucose concentration in whole blood by a near-infrared laser diode", in *Biomedical Optoacoustics II*, A.A. Oraevsky Ed., Proc. SPIE vol. 4256, pp. 77-83, 2001.

39. Stedman, "Stedman's medical dictionary", 27th edition, Lippincott Williams & Wilkins, Baltimore, 2000.

40. A.A. Karabutov, N.B. Podymova, I.M. Pelivanov, S.E. Skipetrov, A.A. Oraevsky, "Direct measurement of axial distribution of absorbed optical energy in turbid media by time-resolved optoacoustic method", in *Biomedical Optoacoustics*, A.A. Oraevsky Ed., Proc. SPIE vol. 3916, pp. 112-121, 2000.

41. S.L. Jacques, J.A. Viator, and G. Paltauf, "Optoacoustic imaging of tissue blanching during photodynamic therapy of esophageal cancer", in *Biomedical Optoacoustics*, A.A. Oraevsky Ed., Proc. SPIE vol. 3916, pp. 322-330, 2000.

42. J.A. Viator, G. Paltauf, S.L. Jacques, and S.A. Prahl, "Design and testing of an endoscopic photoacoustic probe for determination of treatment depth after photodynamic therapy", in *Biomedical Optoacoustics II*, A.A. Oraevsky Ed., Proc. SPIE vol. 4256, pp. 16-27, 2001.

43. P.C. Beard, F. Pérennès, E. Draguioti, and T.N. Mills, "Optical fiber photoacoustic-photothermal probe", *Optics Letters*, vol. 23, pp. 1235-1237, 1998.

44. P.C. Beard, A.M. Hurrel, and T.N. Mills, "Characterization of a polymer film optical fiber hydrophone for use in the range 1 to 20 MHz: A comparison with PVdF needle and membrane hydrophones", *IEEE Trans. Ultrason., Ferroelect., Freq. Contr.*, vol 47 (1), pp. 256-264, 2000.

45. J.G. Laufer, P.C. Beard, S.P. Walker, and T.N. Mills, "Photothermal determination of tissue phantoms using an optical fibre probe", *Phys. Med. Biol.*, vol. 46, pp. 2515-2530, 2001.

46. R. Fainchtein, B.J. Stoyanov, J.C. Murphy, D.A. Wilson, and D.F. Hanley, "Local determination of hemoglobin concentration and degree of oxygenation in tissue by pulsed photoacoustic spectroscopy", in *Biomedical Optoacoustics*, A.A. Oraevsky Ed., Proc. SPIE vol. 3916, pp. 19-33, 2000.

47. R. Fainchtein, B.J. Stoyanov, J.C. Murphy, D.A. Wilson, and D.F. Hanley, "In-vivo photoacoustic spectroscopy of hemoglobin in cerebral tissue", *Prog. Nat. Sci.*, vol. 6, pp. S589-S593, 1996.

48. G. Paltauf, H. Schmidt-Kloiber, K.P. Köstli, and M. Frenz, "Optical method for two-dimensional ultrasonic detection", *Appl. Phys. Lett.*, vol. 75 (8), pp. 1048-1050, 1999.

49. D. Frauchiger, K.P. Köstli, G. Paltauf, M. Frenz, and H.P. Weber, "Optoacoustic tomography using a two dimensional optical pressure

transducer and two different reconstruction algorithms", in *Hybrid and Novel Imaging and New Optical Instrumentation for Biomedical Applications*, A. Bocarra, A.A. Oraevsky Eds., Proc. SPIE vol. 4434, pp. 74-80, 2001.

50. K.P. Köstli, M. Frenz, H.P. Weber, G. Paltauf, and H. Schmidt-Kloiber, "Optoacoustic tomography: time gated measurement of pressure distributions and image reconstruction", *Applied Optics*, vol. 40, pp. 3800-3809, 2001.

51. P.C. Beard, and T.N. Mills, "An optical detection system for biomedical photoacoustic imaging", in *Biomedical Optoacoustics*, A.A. Oraevsky Ed., Proc. SPIE vol. 3916, pp. 100-109, 2000.

52. P.C. Beard, and T.N. Mills, "2D line-scan photoacoustic imaging of absorbers in a scattering tissue phantom", in *Biomedical Optoacoustics II*, A.A. Oraevsky Ed., Proc. SPIE vol. 4256, pp. 34-42, 2001.

53. A.A. Karabutov, E.V. Savateeva, and A.A. Oraevsky, "Optoacoustic supercontrast for early cancer detection", in *Biomedical Optoacoustics II*, A.A. Oraevsky Ed., Proc. SPIE vol. 4256, pp. 179-187, 2001.

54. A.A. Oraevsky, A.A. Karabutov, and E.V. Savateeva, "Enhancement of optoacoustic tissue contrast with absorbing nanoparticles", in *Hybrid and Novel Imaging and New Optical Instrumentation for Biomedical Applications*, A. Bocarra, A.A. Oraevsky Eds., Proc. SPIE vol. 4434, pp. 60-69, 2001.

55. M.D. Stern, "*In vivo* evaluation of microcirculation by coherent light scattering", *Nature*, vol. 254, pp. 56-58, 1975.

56. R. Bonner, and R. Nossal, "Model for laser Doppler measurements of blood flow in tissue", *Applied Optics*, vol. 20 (12), pp. 2097-2107, 1981.

57. G.E. Nilsson, T. Tenland, and P.Å. Öberg, "A new instrument for continuous measurement of tissue blood flow by light beating spectroscopy", *IEEE Trans. Biomed. Eng.*, vol. 27 (1), pp. 12-19, 1980.

58. G.A. Holloway Jr., and D.W. Watkins, "Laser Doppler measurement of cutaneous blood flow", *J. Invest. Dermatol.*, vol. 69, pp. 306-309, 1977.

59. F.F.M. de Mul, J. van Spijker, D. van der Plas, J. Greve, J.G. Aarnoudse, and T.M. Smits, "Mini laser-Doppler (blood) flow monitor with diode laser source and detection integrated in the probe", *Applied Optics*, vol. 23 (17), pp. 2970-2973, 1984.

60. A.N. Serov, S. Oosterbaan, J. Nieland, H. van Kranenburg, F.F.M. de Mul, and W. Steenbergen, "Integrated probes containing a VCSEL and a multidetector chip, for laser Doppler tissue perfusion monitoring", in *Biomedical Diagnostic, Guidance, and Surgical-Assist Systems III*, T. Vo-Dinh, W.S. Grundfest, D.A. Benaron, Eds., Proc. SPIE vol. 4254, pp. 119-127, 2001.

61. K. Wårdell, A. Jakobsson, and G. Nilsson, "Laser Doppler perfusion imaging by dynamic light scattering", *IEEE Trans. Biomed. Eng.*, vol. 40(4), pp. 309-316, 1993.

62. K. Wårdell, and G. Nilsson, "Laser Doppler imaging of skin", in *Handbook of Non-invasive methods and the skin*, J. Serup, B.E. Jemec, Eds., CRC Press, Boca Raton, 1995.

63. T.J.H. Essex, and P.O. Byrne, "A laser Doppler scanner for imaging blood flow in skin", *J. Biomed. Eng.*, vol. 13, pp. 189-194, 1991.

64. E.J. Droog, W. Steenbergen, and F. Sjöberg, "Measurment of depth of burns by laser Doppler perfusion imaging", *Burns*, vol. 27, pp. 561-568, 2001.

65. A. Serov, W. Steenbergen, and F. de Mul, "Laser Doppler perfusion imaging with a complimentary metal oxide semiconductor image sensor", *Optics Letters*, vol. 27 (5), pp. 300-302, 2002.

66. A.L. Petoukhova, W. Steenbergen, and F.F.M. de Mul, "Low coherence Doppler interferometry to determine path length distribution of multiple-scattered photons", in *Coherence Domain Optical Methods in Biomedical Science and Clinical Applications IV*, V.V. Tuchin, J.A. Izatt, and J.G. Fujimoto Eds., Proc. SPIE vol. 3915, pp. 121-128, 2000.

67. A.L. Petoukhova, W. Steenbergen, and F.F.M. de Mul, "Path-length distribution and path-length-resolved Doppler measurements of multiply scattered photons by use low coherence interferometry", *Optics Letters*, vol. 29, pp. 1492-1494, 2001.

68. K.D. Liem, "Neonatal cerebral oxygenation and hemodynamics. A study using near infrared spectrophotometry", *Ph.D. Thesis*, Catholic University of Nijmegen, Nijmegen, 1996.

2 Design of a double-ring photoacoustic sensor

In this chapter an overview is given of the basics of piezoelectric detection of acoustic waves, after which the design and construction of a piezoelectric sensor is described. A cross-correlation method is presented, which is used to reduce the opening angle of the sensor. In the final paragraph the design and construction of a non-contact optical detection method is shown, based on a dual-polarization interferometer.

2.1 Introduction

Ultrasonic or photoacoustic waves in tissue can be detected by measurement of the pressure or displacement at the tissue surface. Measurement of pressure using piezoelectric sensors is the most commonly used method in photoacoustics.[1-4] Optical methods for detection of acoustic waves have been developed as well.[5-12]

Piezoelectric detection has the advantage that it can have a large bandwidth (up to 100 MHz) with a high sensitivity. Broadband optical detection systems have been reported by Beard et al.[5-7] with a bandwidth up to 25 MHz, and a sensitivity comparable to a piezoelectric polyvinylidene difluoride (PVdF) sensor. As broadband piezoelectric sensors are easier to construct and have a slightly better sensitivity than optical detection systems, the piezoelectric sensors are the best choice for our application.

2.2 Background on piezoelectric detection

Piezoelectric sensors are based on the piezoelectric effect, discovered by Pierre and Jacques Curie in 1880. Piezoelectric behaviour of certain materials is caused by their non centro-symmetric crystal structure.[13,14] If these materials are exposed to stress, a net polarisation of the crystal occurs, due to a separation of the centres of positive and negative charge. Before these materials become piezoelectric active, they have to be poled by applying an external electric field to these materials. All dipole moments are then directed in the poling-direction of the external electric field. This piezoelectric activity is not permanent, as at a temperature above a certain level, called Curie temperature, the non centro-symmetric crystal structure will undergo a phase change to a centro-symmetric crystal structure, accompanied by a loss of piezoelectric properties.

After polarisation of the piezoelectric material, it can be used both as a sensor and transducer (Figure 2.1).
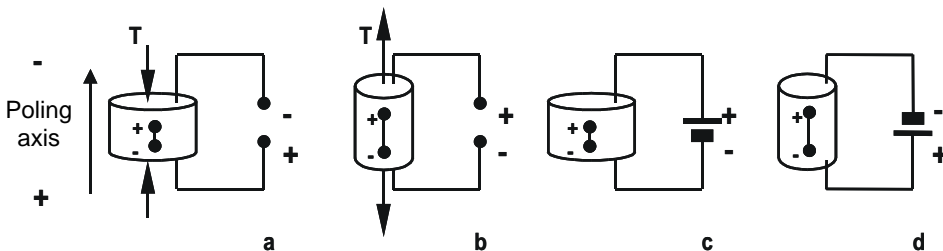

Figure 2.1 *Piezoelectric material used as sensor (a and b) and as transducer (c and d).*

If the poled piezoelectric material is compressed (applied stress T>0, along z-axis), the generated voltage is positive (polarity the same as that of the original

poling voltage) and the material acts as a sensor (Figure 2.1a). The generated voltage is negative if the piezoelectric material is stretched (T<0, Figure 2.1b). When a voltage is applied, the piezoelectric material will be deformed (Figure 2.1c,d) i.e. compressed (c) or stretched (d) depending on the polarity of the applied voltage.

Detection of ultrasonic waves makes use of the effect that deformation of the crystal creates an electric field across the crystal and thus a voltage. This voltage can be measured and reflects the characteristics of the pressure wave at the tissue surface.

2.2.1 Piezoelectric constants

The definition of axes in piezoelectric materials is usually chosen such that the z-axis is in the direction of positive polarization. The x,y and z-axis are denoted by the numbers 1,2 and 3 respectively. The rotations are denoted by 4,5 and 6 (Figure 2.2).
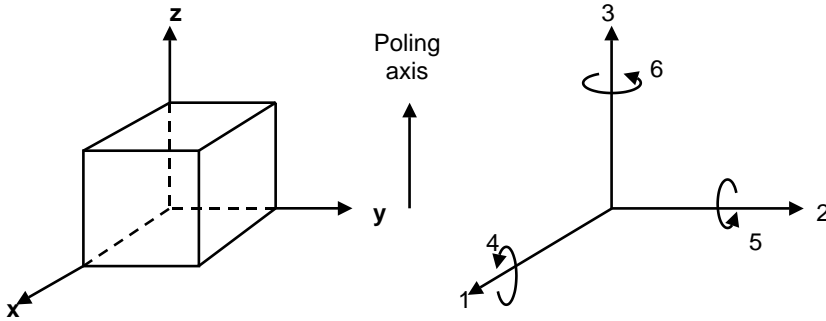
Figure 2.2 *Definition of axes and deformation directions.*

The relationship between the electrical (electric field – E , dielectric displacement – D) and mechanical (strain – S, applied stress – T) variables are given by the piezoelectric constitutive relations.[13] The permittivity ε and the piezoelectric voltage constant g describe the relation between the generated electric field E and the applied stress T, while the relation between the strain S and the dielectric displacement D are described by g and the compliance or stiffness coefficient s:

$$E = \frac{1}{\varepsilon^T} D - gT \quad ; \quad S = s^D T + gD \tag{2.1}$$

where the superscript refers to the quantity kept constant. The first equation describes the effect of the piezoelectrically induced electric field to the total

electric field. Beside the piezoelectric voltage constant g there is also a piezoelectric charge constant d, which is related to ε^T and g by

$$d = \varepsilon^T g \,. \tag{2.2}$$

The piezoelectric constants g,d and ε^T are tensors, which are generally denoted by two subscripts, indicating the components of the tensor. For g_{ij} the first subscript indicates the direction of the electric field, generated by the applied stress which direction is indicated by the second subscript. For d_{ij} the first subscript refers to the direction of the polarization, induced by the applied stress, which direction is indicated by the second subscript. For ε^T_{ij} the first subscript indicates the direction of the dielectric displacement, while the second refers to the electric field. The directions are denoted by numbers as given in Figure 2.2.

When piezoelectric materials are used as sensor, the generated charge or voltage can be calculated using the piezoelectric constants d or g respectively. When the thickness of the piezoelectric material is smaller than the wavelength of the generated photoacoustic wave, only d_{33} and g_{33} have to be taken into account to calculate the generated voltage or charge. The generated voltage or charge is by definition positive if the polarity is the same as the original poling polarity. This implies that when a stress is applied to the piezoelectric material along the 3-axis in negative direction, the resulting voltage or charge is positive (Figure 2.1a).

2.2.2 Piezoelectric materials

There are various piezoelectric materials which are frequently used to detect acoustic waves e.g. polyvinylidene-difluoride (PVdF), piezoelectric ceramics (PZT), Quartz, and Lithium Niobate (LiNbO$_3$).[1,2,13] The overall sensitivity of a piezoelectric sensor is dependent on the required frequency range, the properties of the used piezoelectric material, such as the piezoelectric voltage coefficient g, the transmission of sound from tissue to the piezoelectric material, the thickness of the piezoelectric material, the reflection at the backing and the piezoelement capacity.[1,2] Table 2-1 gives a short overview of characteristic properties of some piezoelectric materials.

Table 2-1: *Properties of some piezoelectric materials.*[1,2,13,15,16]

	Ceramics (PZT-4&PZT-5)	*Quartz*	*LiNbO$_3$*	*PVdF*
g_{33} [10^{-3} V/m]	25-26	50-58	230	170-340
ε_r [-]	900-1200	4.5	29	10-12
ν [m/s]	4350-4800	5740	6300-7400	2150-2400
Z [10^6 kg/m^{2}s]	30-37	15	34-47	3.8

For wideband (1-80 MHz) detection of ultrasonic waves, PVdF is a suitable piezoelectric material[1,2]. Due to the small thickness of PVdF films, they are less sensitive to radial forces. Furthermore, as PVdF has an acoustic impedance Z which is, compared to the other piezoelectric materials, close to the acoustic impedance of soft tissue (about $1.6 \cdot 10^6$ kg/m^{2}s), the amount of sound which is back-reflected at the tissue-piezo interface (see paragraph 2.2.3), is smaller than for other piezoelectric materials. Using acoustic matching layers can reduce the back-reflection of sound into the tissue, but construction of broadband (several tens of MHz) matching layers is difficult.

2.2.3 Detection of photoacoustic waves

Thin piezoelectric sensors make use of a piezoelectric element, which thickness t_p is much smaller than the lateral dimensions.[13] In this case the piezoelectric voltage as a function of time, generated by a photoacoustic pressure-wave P(**r**,t) can be expressed as:

$$V_{piezo}(t) = \frac{g_{33}}{A} \int\limits_{z=0}^{t_p} \int\limits_{A} P(\mathbf{r},t) dA dz \qquad (2.3)$$

where A is the area of the sensor, **r** is the location of the sensor surface.

When the acoustic wave travels from a liquid to the piezoelectric sensor, it crosses a boundary between two materials and follows Snell's law for the angles of reflected, transmitted and refracted longitudinal and shear waves:

$$\frac{\sin\theta_{i,L}}{v_{1,L}} = \frac{\sin\theta_{r,L}}{v_{1,L}} = \frac{\sin\theta_{t,L}}{v_{2,L}} = \frac{\sin\theta_{t,S}}{v_{2,S}} \qquad (2.4)$$

where 1=liquid, 2=solid, θ is the angle with respect to normal to interface, i=incident, r=reflected, t=transmitted, L=longitudinal acoustic wave, S=shear acoustic wave and v=acoustic velocity of longitudinal or shear acoustical wave. Shear waves are generated when a longitudinal wave is incident at an oblique angle ($\theta_i \neq 0°$). As in piezoelectric material the 3,1- and 3,2-coupling is smaller than the 3,3-coupling, (e.g. 9µm Bi-Oriented PvdF – Piezotech S.A. France: $d_{31}=d_{32}=-5$ pC/N; $d_{33}=20-25$ pC/N) the main contribution to the piezoelectric voltage is generated by the normal component of the transmitted wave. The 3,1- and 3,2-coefficients have opposite polarity, compared to the 3,3-coefficients. This causes a decrease in voltage, when waves are incident at an increasing angle, thus reducing the opening angle of the sensor. As the sensor we will design, has already a very small opening angle (see paragraph 2.3), the contribution of the 3,1- and 3,2- coefficients can be neglected.

If the generation of shear waves is neglected, the amplitude reflection and transmission coefficients R_A and T_A are given by:[13]

$$T_A = \frac{\dfrac{2Z_2}{\cos\theta_t}}{\dfrac{Z_2}{\cos\theta_t} + \dfrac{Z_1}{\cos\theta_i}} \;; \qquad R_A = \frac{\dfrac{Z_2}{\cos\theta_t} - \dfrac{Z_1}{\cos\theta_i}}{\dfrac{Z_2}{\cos\theta_t} + \dfrac{Z_1}{\cos\theta_i}} \tag{2.5}$$

where Z is the acoustic impedance, given by

$$Z = \frac{B}{v} = \rho v \,, \tag{2.6}$$

ρ is the specific mass [kg/m^3], v is the acoustic velocity [m/s] and B is the bulk modulus [Pa]. The bulk modulus refers to the ratio of pressure to decrease in volume.

If the thickness t_p of the piezo is small compared to the acoustic wavelength λ_a (i.e. $t_p < \frac{1}{4}\,\lambda_a$), the integration over the thickness of the piezoelectric material can be neglected. The piezoelectric voltage can then be calculated by

$$V_{piezo}(t) = \frac{g_{33}t_p}{A} \int_A P(r,t) T_A(r) \cos(\theta_t(r)) dA \,. \tag{2.7}$$

When the backing of the sensor is not acoustically matched with the piezoelectric material, this introduces a reflection of the acoustic wave at the piezo-backing interface. This gives an increase in the detected voltage by a factor $(1+R_A)$, which in case of normal incidence on a PVdF – copper interface[13] is equal to 1.83.

2.3 *Design of the photoacoustic sensor*

To monitor local blood content in tissue, at depths up to about 3 cm, a sensor is required, which is sensitive only to variations in blood content, which occur on a line in depth. This implies that this sensor should have a very small opening angle. The opening angle is defined as the angle of incidence of ultrasound with respect to the normal of the sensor surface at which the amplitude of the generated voltage is decreased to half of the maximum value.

The shape and size of the piezoelectric element determines the characteristics of the sensor, such as the opening angle. Sensors with a small element size ("point sensors") have a very large opening angle and thus are able to detect acoustic signals originating from a large volume in the tissue.[1] As ring-shaped or annular sensors[1,15,17] have a very small opening angle, this type of sensors is preferred for the above-mentioned application.

To characterize the sensor, the directional sensitivity and depth response to a spherical photoacoustic source can be calculated. The depth response is defined as the signal maximum as a function of depth of the source, while the source is

located on-axis. The directional sensitivity is defined as the signal maximum as a function of the lateral displacement of the source for a certain depth (Figure 2.3).
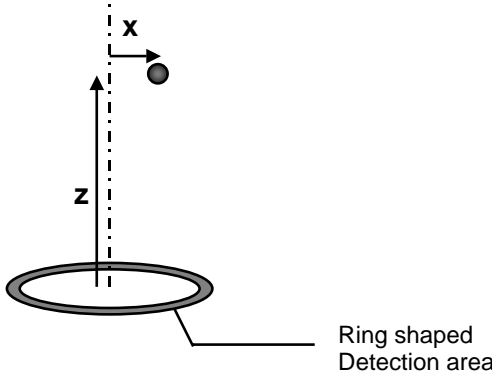
Figure 2.3 *Definition of directional sensitivity and depth response: Depth response is defined as response of the sensor to an acoustic point source located on-axis (x=0) as a function of depth z; Directional sensitivity is defined as response of the sensor to an acoustic source located at a fixed depth z, as a function of the off-axis position x of the source.*

The directional sensitivity and depth response are calculated by numerically evaluating equation 2.7, using the pressure distribution P($\mathbf{r}$,t), generated by a spherical photoacoustic source.

A spherical photoacoustic source with a gaussian absorption distribution (1/e radius r_0), homogeneously illuminated, will generate a spherical pressure wave, which at a distance r (r>>r_0) from the source at time t can be described[18,19] by:

$$P(\mathbf{r},t) = -P_{max}(\mathbf{r})\sqrt{e}\frac{t-\tau}{\tau_e}\exp\left\{-\frac{1}{2}\left(\frac{t-\tau}{\tau_e}\right)^2\right\};$$

$$P_{max}(\mathbf{r}) = \frac{\beta E_a}{2\sqrt{e}(2\pi)^{3/2}c_p\tau_e^2 \mathbf{r}}; \quad \tau = \frac{\mathbf{r}}{v}; \qquad\qquad (2.8)$$

$$\tau_e = \sqrt{\tau_a^2 + \tau_l^2}; \quad \tau_a = \frac{\frac{1}{2}\sqrt{2}r_0}{v}.$$

where β is the thermal expansion coefficient [K^{-1}], c_p is the specific heat capacity [J/kg.K], τ_l is half the pulse duration between the 1/e-points of the temporal amplitude distribution of the laser pulse [s], and E_a is the amount of laser pulse energy which is absorbed by the photoacoustic source [J]. Figure 2.4 shows a typical temporal pressure profile, generated by a spherical photoacoustic source.
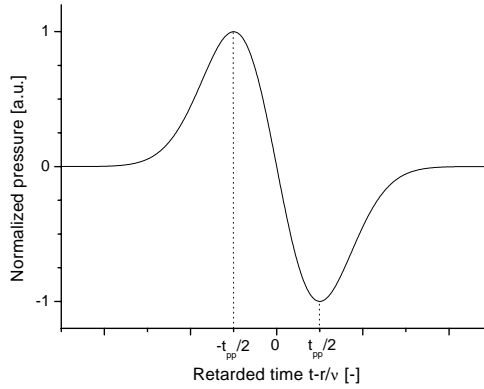
Figure 2.4 *Temporal pressure profile, generated by a spherical photoacoustic source*

The temporal pressure profile of the photoacoustic signal can be characterized by the peak-to-peak time $\tau_{pp}=2\tau_e$. This peak-to-peak time is dependent on the dimensions of the photoacoustic source, as well as the duration of the laser-pulse.

To monitor the blood content in blood vessels with diameters ranging from several tens of micrometers to millimeters, peak-to-peak times of the photoacoustic waves are expected in the range from about 25 ns to 1 μs. This corresponds with frequencies in the 500 kHz – 20 MHz range and wavelengths in soft tissue of about 75 μm to 3 mm.

2.3.1 Width of ring shaped sensor

For optimal charge generation, the maximum pathlength difference for the acoustic signals, arriving at the ring shaped sensor, should be smaller than a quarter of the acoustic wavelength, determining the maximum width w of the ring shaped sensor:

$$\sqrt{z^2+(R+w)^2} - \sqrt{z^2+R^2} \leq \lambda/4 \tag{2.9}$$

z   = depth of photoacoustic source
R   = inner radius of ring shaped sensor surface
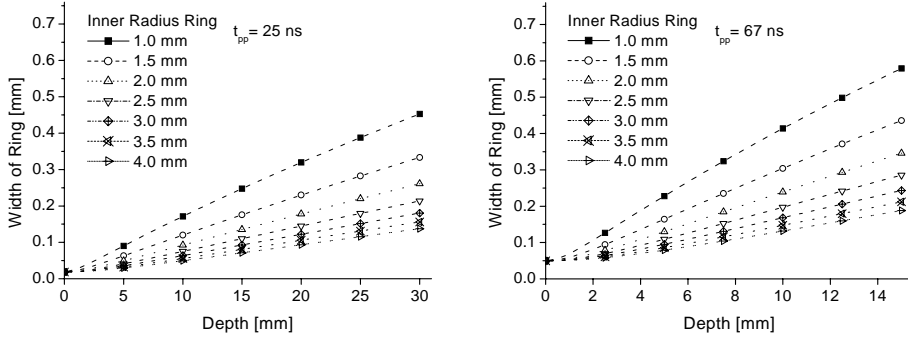w   = width of ring shaped sensor surface.

Figure 2.5 *Maximum width of piezoelectric ring-shaped sensor as a function of depth of the photoacoustic source, which generates acoustical waves with a peak-to-peak time of 25 ns (left panel) and 67 ns (right panel).*

Figure 2.5 gives the maximum width of the ring for various inner ring radii as a function of depth for photoacoustic sources with peak-to-peak times of 25 ns and 67 ns. It is obvious that with increasing peak-to-peak time the maximum width increases. The maximum width of the ring is determined by the minimum depth at which the photoacoustic signal has to be detected with maximum charge generation. Taking an inner radius of 2.0 mm, and a width of the ring of 0.17 mm, then photoacoustic signals with a peak-to-peak time of 67 ns can be detected with maximum charge generation for depths larger than 7.5 mm.

Besides influencing the maximum charge generation, also the width of the ring determines the broadening of the peak-to-peak time of the detected signals, as there will be interference of the acoustic waves, arriving at the ring shaped sensor surface.

Figure 2.6 gives the calculated broadening of the peak-to-peak time and piezo-voltage as a function of the peak-to-peak time of the photoacoustic signal for a depth of 10 mm (left) and 20 mm (right), detected with a ring-shaped sensor area with an inner radius of 2 mm and a width of 0.17 mm. In this calculation it is assumed that all signals, with equal amplitude, are generated by a point source, which is located on the axis of the sensor.
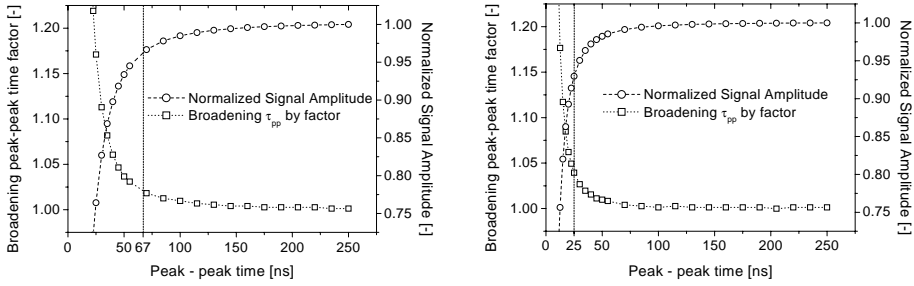
Figure 2.6 *Calculated broadening of peak-to-peak time and normalized signal amplitude, detected by the piezoelectric sensor as a function of peak-to-peak time for a depth of the photoacoustic point source of 10 mm (left) and 20 mm (right), with a ring shaped sensor area with an inner radius of 2 mm and a width of 0.17 mm.*

In Figure 2.6 it is shown that the broadening of the peak-to-peak time and the deviation from maximum signal-amplitude (piezoelectric voltage) is less than 5% for a peak-to-peak time of 67 ns at a depth of 10 mm and for a peak-to-peak time of 25 ns at a depth of 20 mm. This implies that signals generated by small acoustic sources, at small depths will not give an optimal charge generation and that the detected signals are broadened. So the choice of the width of the rings is dependent on the expected source sizes and the depth of these sources.

2.3.2 Directional sensitivity

The directional sensitivity of the ring-shaped sensor has been calculated for various values of the width of the ring. Figure 2.7 shows that the half width at 50% of maximum piezo-voltage (Half Width at Half Maximum – HWHM) of the directional-sensitivity curve does not decrease when the width of the ring is less than the calculated maximum width of the ring (0.17 mm for an inner radius of 2 mm, source located at a depth of 10 mm), as shown in Figure 2.5. By increasing the width of the ring, the directional sensitivity-curve broadens and a side-lobe appears, which implies that the contribution of sources, located off-axis, increases.

Figure 2.5 to Figure 2.7 show that the width of the ring is an important parameter in the design of a ring sensor. The width of the ring has to be chosen such that the expected signals (peak-to-peak time) are detected with minimal broadening and maximum charge generation, while the effect of the side lobes is suppressed as much as possible.
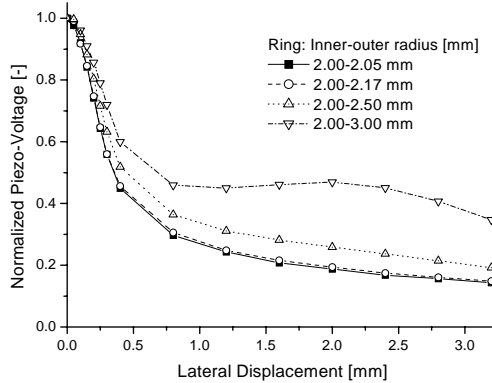
Figure 2.7 *Calculated directional sensitivity of a ring-shaped piezoelectric sensor, for various values of the width of the ring. The calculation uses a photoacoustic point source with a peak-to-peak time of 67 ns at a depth of 10 mm, which lateral position is varied during the calculation.*

The effect of the inner radius on the HWHM is calculated for a photoacoustic point source, which generates a signal with a peak-to-peak time of 67 ns, located at various depths. The width of the ring is chosen such that it is not larger than the maximum width as shown in Figure 2.5, and furthermore the area of the rings is equal for all values of the inner radii. The resulting values of the HWHM are plotted in Figure 2.8.
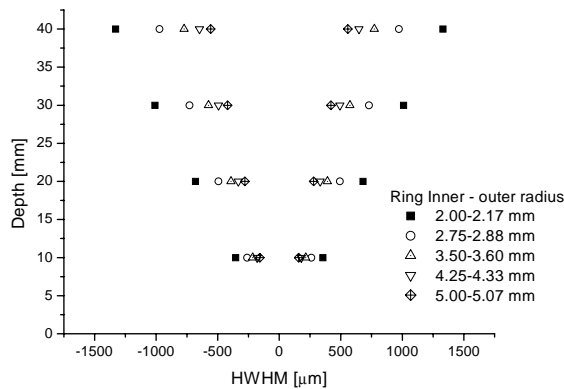
Figure 2.8 *Calculated half-width-at-half-maximum (HWHM) of the directional-sensitivity plot as a function of depth, for various dimensions of the ring-shaped senor. In the calculations, a photoacoustic point source is assumed, which produces an acoustic wave with a peak-to-peak time of 67ns.*

As the directional sensitivity curve is symmetrical around the axis of the ring-shaped sensor surface, the HWHM as plotted in Figure 2.8 may be positive

as well as negative. In this way the opening angle of the sensor is visualized. This graph shows that the HWHM decreases with increasing ring size. This means that the opening angle of the detector reduces as the inner radius of the ring-shaped sensor increases.

Figure 2.9 (left) shows the dependency of the directional sensitivity on the peak-to-peak time of the photoacoustic signal. When the peak-to-peak time increases, the directional sensitivity curve broadens. A larger peak-to-peak time corresponds with a larger acoustic wavelength. The effect of a displacement of the source has a larger effect on the interference of the acoustic waves on the ring shaped sensor surface for smaller acoustic wavelengths compared to larger wavelengths. The relative change in distance to the sensor surface (in units of the wavelength) will be larger for smaller wavelengths. So the opening angle (defined as the arctan of the HWHM over depth) of the sensor is dependent on the properties of the photoacoustic source (Figure 2.9, right panel).

When this sensor is used for imaging purposes, this feature has to be taken into account. For monitoring purposes, this implies that the sensor will be more sensitive to larger photoacoustic sources (larger peak-to-peak time) located off-axis than to small photoacoustic sources located off-axis (smaller peak-to-peak time).
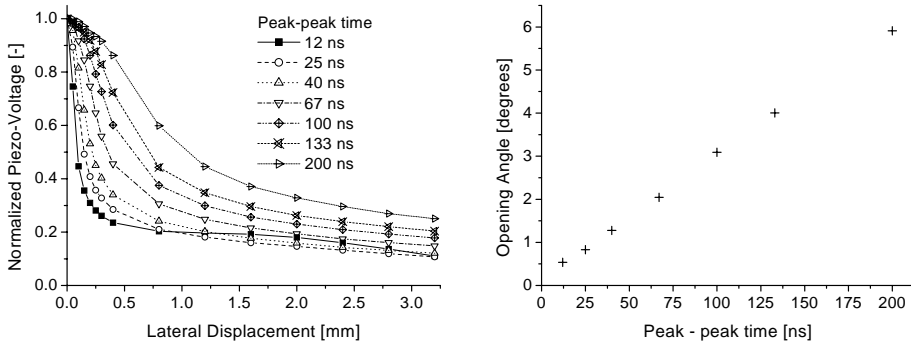
Figure 2.9 *Calculated directional sensitivity (left panel) for a ring-shaped piezoelectric sensor (inner-radius 2.0 mm, width 0.17 mm), for various values of the peak-to-peak time of the photoacoustic point source, which is located at a depth of 10 mm. The right panel shows the opening angle as a function of peak-to-peak time.*

Figure 2.8 to Figure 2.9 show that the directional sensitivity is dependent on the inner radius of the ring shaped sensor surface, as well as the dimensions of the photoacoustic source (peak-to-peak) time. Furthermore it can be seen that the directional sensitivity-curve does not go very fast to zero for relatively large (larger than two times HWHM) displacements of the photoacoustic source. This means that the sensor is still sensitive to sources located off-axis.

To improve the directional sensitivity of the ring-shaped sensor, two rings can be used. The effect that the directional sensitivity does not decrease very rapidly to zero can be reduced using cross-correlation techniques (paragraph 2.4). Furthermore, if a side-lobe occurs in the directional sensitivity this is related to the radius of the ring. As the second ring has a different radius, the side-lobe will appear at a different lateral displacement of the source. By simply adding the signals of both rings, the effect of side-lobes will already decrease with a factor 2.

2.3.3 Double ring sensor

Based on the described calculations of the sensor characteristics we constructed a double ring photoacoustic sensor. It consists of two concentric ring shaped sensor areas. The inner ring has an inner radius of 2 mm and a width of 0.17 mm. The outer ring has an inner radius of 3.5 mm and a width of 0.1 mm, so that the area of both rings is equal. This sensor will be capable of detecting photoacoustic signals with a peak-to-peak time of 67 ns, located at depths larger than 7.5 mm, without any significant distortion of the signals. With increasing depth, also signals with a smaller peak-to-peak time can be detected undistortedly. Furthermore, for photoacoustic signals with a peak-to-peak time larger than 67 ns, the minimum depth at which they are detected as being undistorted, decreases further below 7.5 mm with increasing peak-to-peak time. In many applications of the sensor, there will be a distance between the tissue and the sensor of a few millimeter, which will be filled with ultrasound contact gel. So the effective depth (depth in the tissue) at which the signals can be located as being undisturbed is even smaller. For application of this sensor for monitoring the blood content in the brain, the minimum depth of interest is determined by the thickness of the skin, skull, and the cerebrospinal fluid layer. This total thickness is at least several millimetres. So the limitation on the minimum depth at which the sensor can measure photoacoustic signals undisturbed will not be a problem.

The depth response of the two separate rings has been calculated (Figure 2.10, left panel) for a spherical photoacoustic source, which generates an acoustic signal with a peak-to-peak time of 67 ns. The total (summed) depth response of the double ring sensor is visualized in Figure 2.10, right panel.
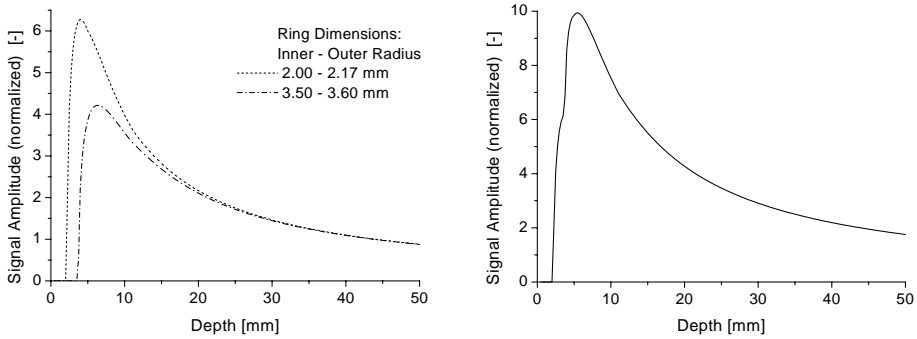
Figure 2.10 *Calculated response of the sensor as a function of depth to a spherical photoacoustic source, which generates an acoustic wave with a peak-to-peak time of 67 ns. Left panel: depth-response of the separate rings; right panel: depth response of the double ring sensor.*

In Figure 2.10 the calculated depth response of the separate rings and the response of the total sensor (sum of the response of the separate rings) are shown. It is obvious that there is a minimum depth at which the sources can be detected. This depth is determined by the critical angle of the transmission of sound from tissue to the piezoelectric material, and thus dependent on the radius of the ring-shaped sensor surface. Furthermore, due to angle dependent transmission of ultrasound from tissue to piezoelectric material, the signal amplitude of the outer ring decreases more rapidly with decreasing source depth than the signal amplitude of the inner ring, as the angle of the sound incident on the ring increases more rapidly (transmission of sound decreases with increasing angle) for a larger ring than for a smaller ring as the depth location of the source decreases.

The right panel of Figure 2.10 (sum of the individual depth responses of both rings) shows a non-linearity at a depth of 3.8 mm, which is caused by the difference in minimum depth, which can be detected by the inner and outer ring as shown in Figure 2.10-left panel.

2.4 Signal processing

2.4.1 Time delay

Before the signals detected by the two ring-shaped sensor areas can be processed (e.g. adding the signals), first they have to be corrected for the time delay which they have with respect to each other. It takes more time for an acoustic wave, generated by a source on-axis of the sensor, to travel from the source to the outer ring, compared to the inner ring.

Figure 2.11 shows the time delays Δt_{in} and Δt_{out}, which appears when a signal travels from a source located on-axis to the inner and outer ring. By applying this time delay, the time t' at which the signals are detected by the rings is corrected such that the corrected time t corresponds to the depth z of the PA source ($t = z/v$):

$$t = \frac{\sqrt{(vt')^2 - R^2}}{v}$$ (2.10)

where R is the radius to the center (see Figure 2.11) of the ring-shaped detection area. As now the time-axes of both rings are corresponding to the depth of the PA source, the signals of both rings can be processed (e.g. adding the signals).
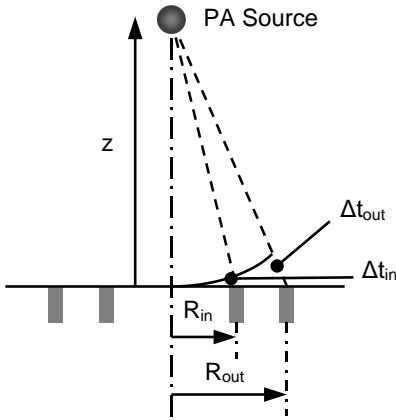

Figure 2.11 *Schematic overview of time delay, for a PA signal, traveling from a source located on-axis to the inner and outer ring.*

2.4.2 Cross-correlation

The directional sensitivity of the double ring sensor can be further improved by calculation of the zero-time cross-correlation $C(\tau=0)$ between the signals detected by the inner ring $S_{in}(t)$ and outer ring $S_{out}(t)$, according to:

$$C(\tau) = \int S_{in}(t)S_{out}(t+\tau)dt$$ (2.11)

If the PA source is located on-axis, the cross-correlation C(0) will be maximum, as both rings will detect the photoacoustic signal (after correction for the above mentioned time delay) at the same time, with an identical shape. If the source is located off-axis, then the signals detected by the inner and outer ring will be different (different shape and temporal behaviour), due to different interference at the inner and outer ring, and the cross-correlation will decrease.
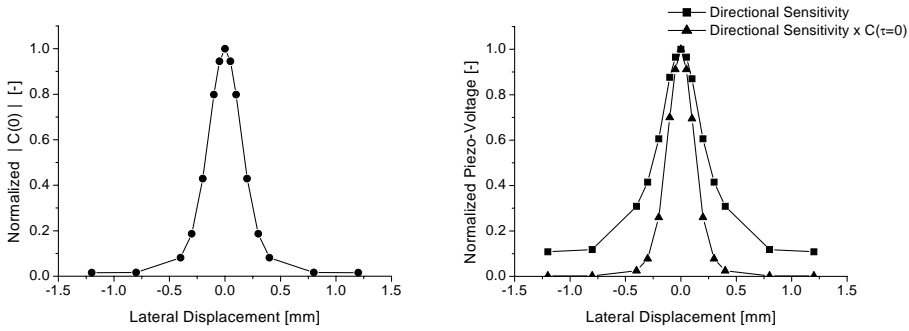
Figure 2.12 *Left-panel: Zero time cross-correlation of the signals detected by the inner and outer ring, as a function of the lateral displacement of a photoacoustic point source, located at a depth of 10 mm, which generates a signal with a peak-to-peak time of 67 ns. Right panel: Corresponding directional sensitivity curve for the double-ring sensor with and without multiplication by the zero-time cross-correlation function as shown in the left-panel.*

Figure 2.12, left panel, shows the zero-time cross correlation C(0), as a function of lateral displacement of the photoacoustic source, of the signals detected by the inner and outer ring, after correction for the time delay. This photoacoustic source was located at a depth of 10 mm, generating an acoustic signal with a peak-to-peak time of 67 ns. The cross-correlation function has a full-width-at-half-maximum (FWHM) of 0.37 mm, which will reduce the opening angle of the sensor. Furthermore, it suppresses the amplitude of signals generated off axis, as the correlation goes faster to zero than the directional sensitivity. This is shown in Figure 2.12 right panel, where the directional sensitivity is shown, with and without multiplying by the zero-time cross-correlation function. The FWHM is reduced by a factor 1.8, from FWHM = 0.51 mm to 0.29 mm.

2.5 *Experimental verification of detector characteristics*

The detector characteristics, like depth response, directional sensitivity and the above mentioned cross-correlation technique have been verified experimentally (experimental set-up: chapter 3). A 200 μm diameter, black horse-tail hair, illuminated by a 100 μm diameter fiber, acted as a PA-point source, generating a bipolar PA signal with a peak-to-peak time of 40 ns. The hair was illuminated from the bottom side, along a length of about 200 μm. As the absorption of the hair is fairly high, only a shell of the hair, at the bottom side, will act as a PA source.

The directional sensitivity is measured by laterally displacing the sensor with respect to the source, while the source was located at a depth of 10 mm. The

maximum amplitude of the photoacoustic signal is taken as a measure for the directional sensitivity, which together with the calculated curve is shown in Figure 2.13 left panel.

The zero-time cross-correlation has been calculated from the measured signals. The measured directional sensitivity has been multiplied by this cross-correlation. Figure 2.13 right panel, shows the result, together with the calculated (from theory) directional sensitivity, multiplied by the calculated cross-correlation. By using the zero-time cross-correlation as a weight factor, the sensor gets a much more pronounced forward sensitivity, i.e. reduced opening angle. Furthermore, the directional sensitivity decreases much faster to zero for off-axis translation, when the correlation is used as weight factor.

As mentioned earlier, only a part of the bottom side of the hair acts as a photoacoustic source. The hair has different acoustic properties compared to the surrounding water, so it will shield a part of the sound. This can explain the decrease in amplitude of the photoacoustic signals, as observed for some points in the center (exactly above the hair) of the directional sensitivity curve.
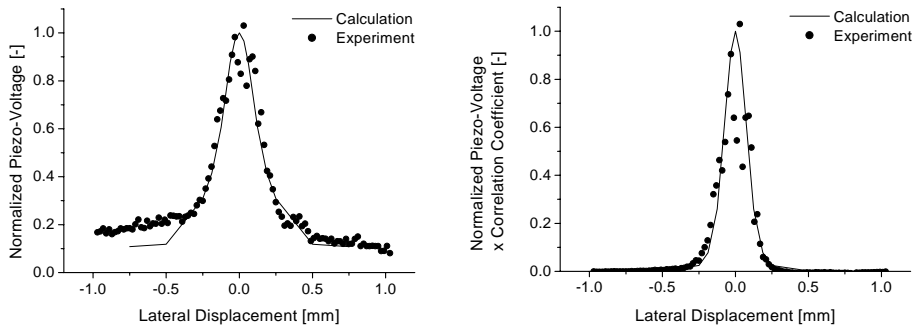
Figure 2.13 *Left panel: measured directional sensitivity, defined as the maximum amplitude of the sum of both ring-signals, compared with the calculated (from theory) directional sensitivity, for a point source with a peak-to-peak time of 40 ns, located at 10 mm depth. Right panel: Directional sensitivity curve, multiplied by the zero-time cross-correlation function, resulting from an experiment and resulting from the theoretical calculation.*

The measured depth response, together with the calculated depth response are shown in Figure 2.14. The maximum amplitude of the photoacoustic signal is taken as a measure for the depth response of the constructed photoacoustic sensor.

Figure 2.14 *Depth response of the constructed double ring sensor, calculation (line) compared with measurement (dots), both for a point source with a peak-to-peak time of 40 ns.*

2.6 Signal amplification

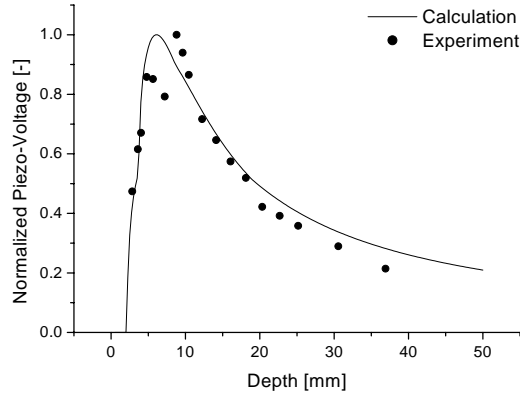To amplify the piezoelectric signal there are two possible amplification schemes: voltage amplification (VA) and charge amplification (CA). Hoelen[1] has shown that there is no large difference in signal to noise ratio (SNR) between VA and CA, but in some cases the CA method has a slightly larger SNR.

To amplify the signals of the double-ring sensor, the CA has been chosen. The used circuit, consisting of two amplification stages is shown in Figure 2.15.
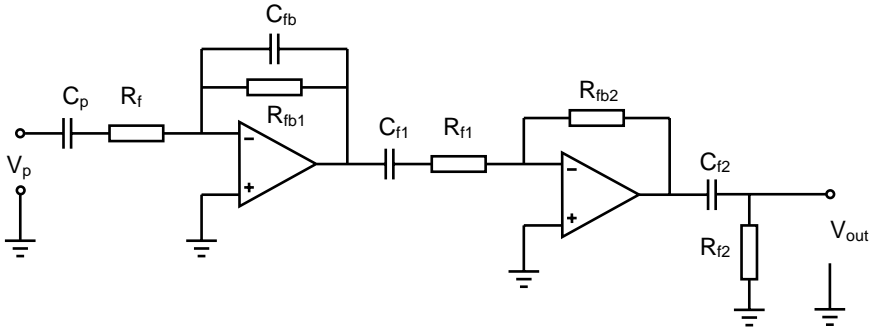
Figure 2.15 *Amplifier configuration, consisting out of pre-amplifier, post-amplifier and high-pass filter (R_{f2}, C_{f2}). Symbols: V_p = piezo voltage, V_{out} = output voltage, C_p = piezo capacitance, C_{fb} = feedback capacitance, R_{fb1}, R_{fb2} = feedback resistances, R_f, R_{f1}, R_{f2} = filter resistances.*

The transfer function $H(\omega)$ consists of three parts: $H_{pre}(\omega)$, $H_{post}(\omega)$, and $H_{filter}(\omega)$, which are given by:

$$H_{pre}(\omega) = \frac{-j\omega R_{fb1}C_p}{(j\omega R_f C_p + 1)(j\omega R_{fb1}C_{fb} + 1)}$$

$$H_{post}(\omega) = \frac{-j\omega R_{fb2}C_{f1}}{j\omega R_{f1}C_{f1} + 1}$$

$$H_{filter}(\omega) = \frac{j\omega R_{f2}C_{f2}}{j\omega R_{f2}C_{f2} + 1}$$

$$H(\omega) = \frac{V_{out}}{V_p} = H_{pre}(\omega) \cdot H_{post}(\omega) \cdot H_{filter}(\omega).$$

(2.12)

For the given dimensions of the inner and outer ring and the properties of the 9 µm thick PVdF (Piezotech SA, France), the capacity of the piezo C_p will be 26 pF. The amplitude transfer-function as a function of frequency is given in Figure 2.16, which shows a –3dB bandwidth of about 75 MHz, starting at 1 MHz.
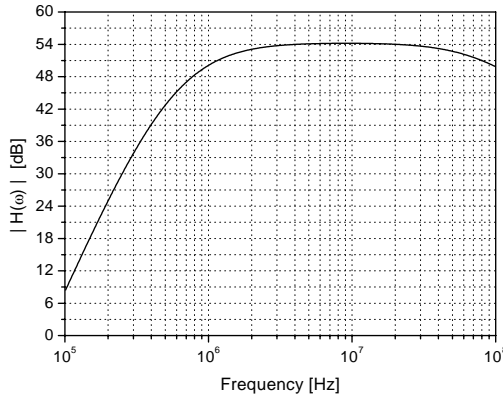
Figure 2.16 *The Amplitude transfer-function $|H(\omega)|$ of the amplifier used with the double ring sensor. C_p=26pF, R_{fb1}=82kΩ, Rf=82Ω, C_{fb}=2.2pF, C_{f1}=6.8nF, R_{f1}=50Ω, R_{fb2} =2.2kΩ, C_{f2}= 6.8nF, R_{f2}=50Ω.*

2.7 Illumination system

To generate photoacoustic waves in tissue, the tissue has to be illuminated by pulsed light. The amount of light, which can by applied to the tissue, is restricted by safety regulations as ascertained by the standard NEN-EN 60825:1994. This standard gives values for the Maximum Permissible Exposure (MPE) as a function of pulse-duration and exposure time (=duration of pulse train

[sec]). Based on this standard, the maximum pulse energy has been calculated as a function of exposure time, for light pulses with duration of 5-15 ns and a repetition rate of 10 Hz.
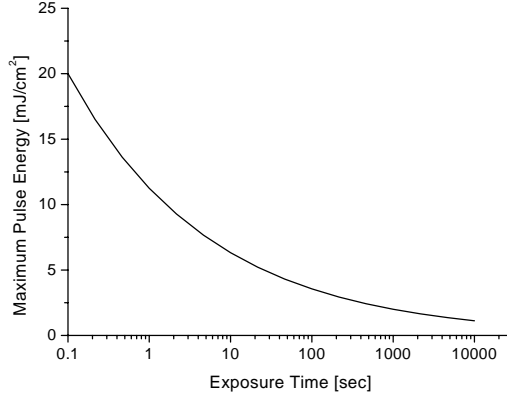
Figure 2.17 *Maximum pulse energy, to be used with photoacoustics, as a function of exposure (measurement) time for pulse lengths in the range from 5 – 15 ns and a repetition rate of 10 Hz (NEN-EN 60825).*

Figure 2.17 shows that when multiple pulses are used, the maximum pulse energy decreases rapidly. The maximum pulse energy [mJ/cm^2], for an exposure time T [sec], a pulse duration of 5-15 ns and a repetition rate f [Hz], is then given by

$$E_{pulse} \leq 20 \cdot \left(f \cdot T \right)^{-\frac{1}{4}} \quad [mJ/cm^2] \tag{2.13}$$

To optimise the amount of energy per pulse to be used with photoacoustics, the exposure area of the tissue should be as large as possible. As the designed sensor consists of two concentric ring-shaped electrodes, there are two possible ways to integrate the illumination in the sensor: inside the electrodes – disc shaped (fiber) illumination, or around the electrodes – ring shaped illumination.

Monte-Carlo simulations of the light scattering in tissue[20] have been used to compare these two illumination systems. Simulations have been performed for the light distribution in a homogeneous, semi-infinite, tissue-like medium with a reduced scattering coefficient of 0.75 mm^{-1} and an absorption coefficient of 0.05 mm^{-1}. These values are about the values for scattering and absorption of tissue at a wavelength of 800 nm.

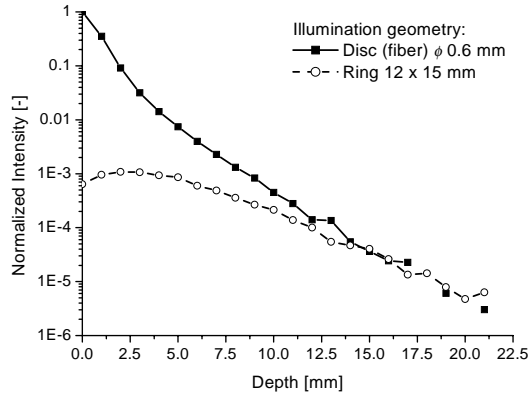**Figure 2.18** *Simulated on-axis intensity as a function of depth for two different illumination geometries. Optical properties of medium:* μ_s*' = 0.75 mm*$^{-1}$*;* μ_a *= 0.05 mm*$^{-1}$*. The vertical axis gives the on-axis intensity [mJ] for a light pulse of 1 mJ, incident on the tissue surface.*

Figure 2.18 shows the on-axis intensity as a function of depth for a ring-shaped (12 x 15 mm diameter) and disc-shaped (0.6 mm diameter) illumination geometry. The intensity is normalized on the intensity (amount of photons), which is applied to the tissue. The vertical axis gives the on-axis intensity [mJ] for a light pulse of 1 mJ, incident on the tissue surface.

In case of a ring-shaped illumination geometry, the photons are injected at a distance of 6 to 7.5 mm from the axis of the illumination system. This results in lower on-axis intensity for small depths than the disc shaped illumination system. However, due to the scattering of light by the tissue, at depths larger than about 12.5 mm, both systems give an equal intensity. As the area of the ring-shaped illumination system is about 56 times larger than the disc-shaped (fiber) system, the amount of energy that can be applied to the tissue is also 56 times larger. This means that for larger depths (larger than about 12.5 mm), the ring-shaped illumination system is more advantageous than the disc-shaped (fiber) illumination system, due to the larger area. With the current design of the photoacoustic sensor, the fiber diameter can be further increased to about 6 mm, while the outer radius of the ring-shaped illumination is determined by practical considerations (compactness of probe) only.

The ring shaped illumination system is constructed from a hollow quartz-glass cylinder (12 x 15 mm, length 24 mm), which is mirrored (aluminium) on the inner and outer side. To inject the light into this hollow cylinder, 4 fibers (ø 600 µm, NA=0.22) are placed on top of this glass cylinder, as shown in Figure 2.19. The length of the glass-cylinder, the numerical aperture (NA) of the fibers used, and the amount of fibers determine the homogeneity of the light distribution at the bottom of the ring shaped illumination system. Increase of these parameters

(increased length, larger NA, larger number of fibers) will give a more homogeneous light distribution.
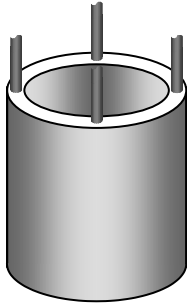
Figure 2.19 *Schematic overview of construction of ring-shaped illuminator: hollow quartz-glass cylinder, mirrored (aluminium) on inner and outer surface. End sides of cylinder are polished. 4 fibers are placed on top of glass cylinder to inject light into the ring-shaped illuminator.*

2.8 Construction of photoacoustic double ring sensor

The double-ring photoacoustic sensor consists of two concentric rings (diameter 4.00 x 4.34 mm and 7.00 x 7.20 mm) together with a fiber or ring-shaped illumination system. The electrodes are constructed by using a printed circuit board (PCB) with two concentric copper circles (electrodes) on it. A metallized hole through the PCB connects the electrodes to the amplifiers. The piezoelectric material (9 μm thick PVdF, biaxially stretched, poled, with one side metallized Au/Pt, Piezotech SA, France) is glued to the PCB, using significant pressure to minimize the thickness of the glue layer. Everything is embedded in a brass housing to shield the electronics for electromagnetic noise.

Figure 2.20 shows a schematic drawing of the photoacoustic double ring sensor, with a fiber for illumination integrated in the sensor. The sensor with a ring-shaped illumination system is constructed in a similar way: instead of a fiber in the center, a mirrored, hollow glass cylinder in which the sensor and amplifiers are mounted is used.
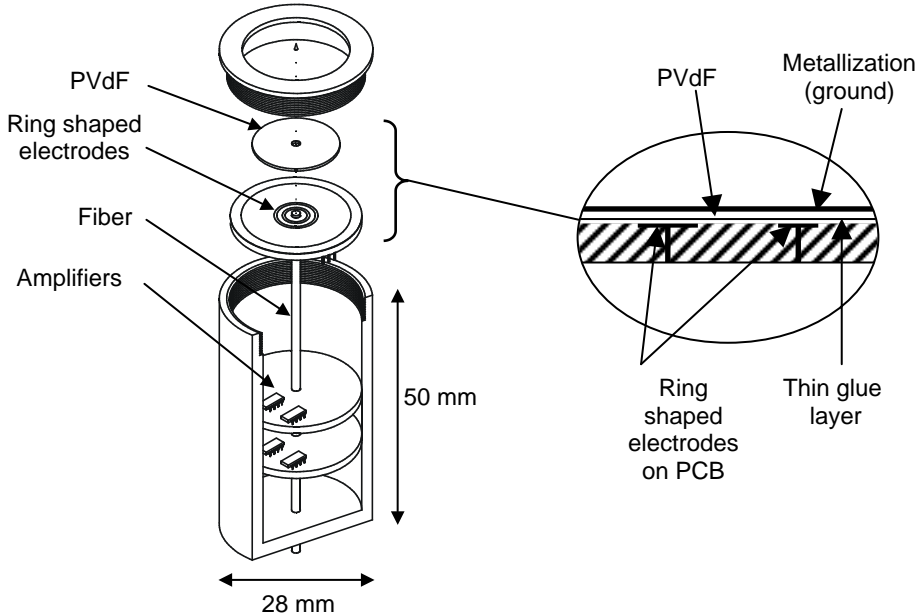
Figure 2.20 *Schematic drawing of photoacoustic double ring sensor, with a fiber for illumination integrated in the sensor. The piezo-film (PVdF) is glued to the PCB with two ring-shaped, copper electrodes on it. The top surface of the PVdF is metallized and connected to ground. The pre- and post-amplifiers are mounted inside the brass housing.*

2.9 Optical detection of photoacoustic waves

If one uses photoacoustics to image absorbing structures in tissue, it is preferable to have an array of photoacoustic sensors, to minimize measurement time. The minimum sensor element size and inter-element spacing determine the image resolution, and are mainly limited by technological aspects (size of electronics on chip). With an all-optical detection method of acoustic waves, the sensor array can be replaced by very fast CMOS or CCD cameras. By using imaging optics, the minimum element size is then only determined by the way the optical sensor is addressed (eg. spot size of light source at interface). Furthermore it is possible to construct transparent sensor systems through which the excitation light pulses can be transmitted for reflection-mode (or backward mode) photoacoustic imaging. In addition, an optical detection system can be constructed such that no contact is required, which is preferable in certain applications where sterility and patient friendliness are essential, like determination of burn-wound depth.

Paltauf et al.[8,9] have developed an optical detection system, based on pressure-induced changes of optical reflectance at a glass liquid interface. The changes in optical reflectance are recorded by a time-gated video camera, which makes it possible to image the pressure distribution at the liquid interface at once, without the need of scanning with the sensor over the interface. However, only one time-of-flight (or depth) position can be monitored at the same time (time windowing).

Beard et al.[5-7] have developed a Fabry-Perot polymer film sensor, based on pressure induced variations in thickness of the polymer film. The thickness variations in the polymer film are detected using a Fabry-Perot interferometer. Based on this technique they have developed a photoacoustic fiber probe and a system that can be used for imaging purposes. The detection of the interference pattern can be carried out using a time-gated camera, like the one Paltauf et al.[8,9,10] have used. To obtain a maximum sensitivity, the wavelength of the laserdiode used in the interferometer, or the angle of incidence to the polymer film have to be tunable.

Both above described optical detection systems have to be in contact with the tissue, like in piezoelectric detection of acoustic waves. A different method, described by Jacques et al.[11,12] is based on non-contact detection of acoustic waves. This system makes use of a dual beam common path interferometer. Two beams are directed to the tissue surface at a small distance from each other. When the pressure wave arrives at the surface, a displacement is induced, which will be detected by the interferometer. An advantage of the common path interferometer is that it is insensitive to variations in distance from the interferometer to the surface, as these changes are the same for both paths of the interferometer. However, this set-up has to be used in a scanning mode and cannot be easily adapted to a set-up in which the whole pressure or displacement distribution is measured at once by using e.g. a time-gated camera.

2.9.1 Construction of a dual-polarization interferometer

In a first attempt towards a non-contact photoacoustic optical detection system, suitable for imaging, we applied a dual-polarization interferometric set-up, as described by Kubota et al.[21] for displacement or distance measurements in general. We tested the application of this dual-polarization interferometer by detection of displacements (caused by PA-generated ultrasonic waves) of unpolished reflective tape (sellotape), positioned as to seal a hole in the wall of a water reservoir. The tape is used to mimic the tissue surface, while the water reservoir mimics the tissue. The results are compared to those of measurements with a 200 μm diameter, 9 μm thick PVdF disk detector.[1]
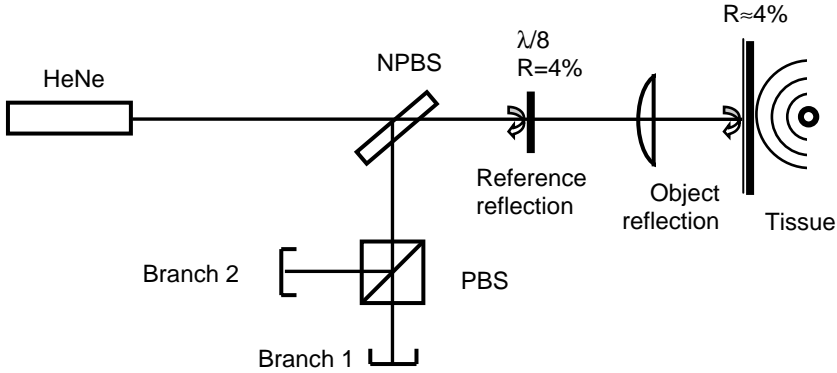
Figure 2.21 *Schematic set-up of the dual polarization interferometer. PBS = polarizing beam splitter, NPBS = non-polarizing beam splitter. The reference arm of the interferometer is formed by the reflection of the He-Ne laser beam at the non-coated side of the λ/8 retardation plate. A 80 mm focal length lens has been used to reduce the spot size of the laser beam at the tissue. In the experiments the tissue has been simulated by using unpolished reflective tape, which covers a hole in the wall of a water reservoir. The photoacoustic source was located inside the reservoir.*

Figure 2.21 shows the set-up of the used dual polarization interferometer. The system measures two polarizations separately, where each polarization branch can be regarded as an independent interferometer. The interferometer is insensitive to variations in object – interferometer distance, as these distance variations are present in both polarizations. The reference arm in this interferometer is formed by reflection of the beam at the uncoated surface of the λ/8 retardation plate. The interference pattern of one polarization is shifted over λ/4 with respect to the other polarization (Figure 2.22), due to the λ/8 retardation plate. This results in sensitivities (defined as modulation of laser power incident on the detector surface per unit displacement of the (tissue-) interface [W/m]) of the two branches, proportional to $\sin\theta$ and $\cos\theta$, respectively (where the phase angle θ is the optical pathlength difference between the reference and object arm). With the displacement u of the sample the change in phase angle $\Delta\theta$ can be written as $\Delta\theta = 4\pi u/\lambda$, assuming that the interferometer is placed in air (with refractive index n=1). After determining the sign of the sensitivities of each branch (derivative of curve in Figure 2.22) and multiplying the signals with this sign, the signals of the two branches can be summed. The sensitivity of the total interferometer will then, after correction for the sign of the sensitivity of the two branches, be equal to the sum of the absolute values of both sensitivities:

$$S = \left\{ |\sin\theta| + |\cos\theta| \right\} \frac{4\pi}{\lambda} P_{AC} \quad [\text{W/m}] \qquad (2.14)$$

where P_{AC} is the amplitude [W] of the interference pattern. This amplitude is equal to the visibility V times the DC-power P_{DC}. The values of the factor ($|\sin\theta| + |\cos\theta|$) will fluctuate between 1 and $\sqrt{2}$, with an average value of 1.2 and a standard deviation of 13 %. We calculated the sensitivity to be:

$$S = 1.2\frac{4\pi}{\lambda}P_{DC}V \qquad [\text{W/m}] \tag{2.15}$$

Theoretically, a constant value for the sensitivity can be obtained by squaring the measured displacement signals, as $(\sin^2 + \cos^2)$ gives a constant value for the sensitivity. However, low frequency fluctuations in the set-up (e.g. environmental noise - vibrations) will cause the measured displacement signal to fluctuate with these frequencies as well. When squaring the signals of both branches, the final amplitude of the signal and thus the sensitivity will be dependent on the low frequency fluctuations. So the overall sensitivity will not be constant anymore. It has been tried to filter out all frequencies below 1 MHz, but even in this case, the above-described method (adding the signals of both branches after determination of the sign) was less sensitive to these fluctuations and gave a more stable value for the sensitivity.

If we assume that the system is shot noise limited, then the signal-to-noise-ratio (SNR) of the interferometer can be calculated to be:

$$SNR = \frac{\eta Su}{2\sqrt{2e\eta P_{DC}B}} \tag{2.16}$$

with η the sensitivity of the photodetector [A/W], B the bandwidth of the detection system [Hz], and u the displacement of the sample [m]. The factor 2 in the denominator before the square root appears because we are using two photodetectors. The signals of these two detectors are added, resulting in addition of the noise.

If we define the minimum detectable displacement u_{min} as the displacement that causes a voltage equal to the noise floor (SNR=1), then u_{min} is given by:

$$u_{min} = 2\sqrt{\frac{2eB}{\eta P_{DC}}}\frac{\lambda}{4\pi}\frac{1}{1.2V} \tag{2.17}$$

This theoretical minimum detectable displacement u_{min} is in our case 0.05 nm, if we assume a maximum visibility: V=1 (P_{DC}=0.04mW, B=20MHz, λ=632.8nm, η=0.4A/W, e=1.6 10^{-19}C).

Figure 2.22 shows that there are four regions of interest, where each region corresponds with a unique pair of signs for the sensitivities of branch 1 and 2. The information about the DC-power incident on the photodetector can be used to determine the region in which the measurement is performed. An example of a measurement in which the branches have opposite sign for the sensitivity is given in Figure 2.23.
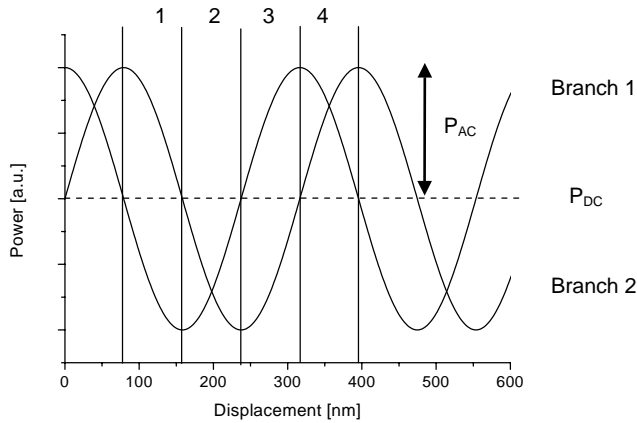
Figure 2.22 *Interference pattern of branch 1 and 2 are shifted over π/2. Four regions can be distinguished with a unique pair of signs for the sensitivities (derivative of power incident on photodetector with respect to displacement) of the branches.*
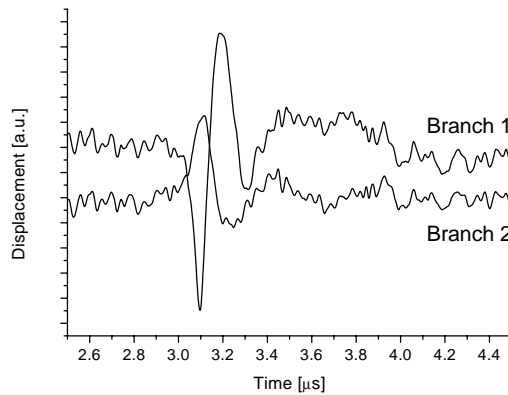
Figure 2.23 *Single measurement, where the sensitivities of the branches have opposite signs.*

A photoacoustic signal was generated by illuminating a Solvent Red solution in paraffin oil with a 532 nm Nd:YAG laser with 12 ns pulses operating at 50 Hz repetition rate, with an energy of 1 mJ per pulse. The absorption coefficient of the solution was μ_a=160 mm^{-1}, about 5 times that of blood. Paraffin oil was used for its large thermal expansion coefficient (~400 times larger than water) in comparison to water or blood. The absorbing medium was attached to the end of a 600 μm diameter illumination fiber (Figure 2.24), and placed inside the water reservoir. At a distance of 4 mm from the absorbing source, a 1cm^2 window in the water tank was sealed by unpolished reflective tape (sellotape). In the interferometer, a 80 mm focal distance lens was used to focus the HeNe-laser (Uniphase, 632.8 nm, 10 mW) beam into a 180 μm diameter spot, in order to

prevent acoustic destructive interference at the surface of measurement. This destructive interference might originate from signals from different spots on the detector, in case the beam is too wide. The interference signals in the branches are detected by photodiodes, with a 1-20 MHz bandwidth.

Displacement of this surface due to the generated pressure waves inside the water tank is detected by the non-contact dual polarization interferometer. For comparison of the results obtained with the interferometer, also measurements are carried out with a 200 μm diameter, 9 μm thick PVdF piezoelectric detector.[1]
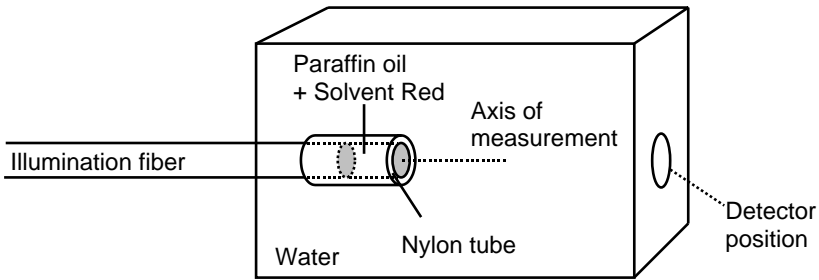
Figure 2.24 *Solvent Red solution in paraffin oil, directly attached to the illumination fiber is used as a photoacoustic source.*
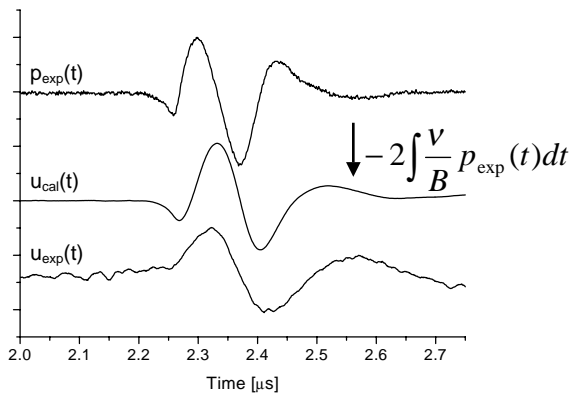
Figure 2.25 *Comparison of PA measurements with the interferometer and with a PVdF probe. Upper trace: single measurement of pressure signal with piezoelectric detector. Middle trace: displacement calculated from the measurement of the pressure signal with the piezoelectric detector by integration (see text) over time. Lower trace: average of 7 measurements of the displacement of the interface with the dual polarization interferometer.*

Figure 2.25 shows a comparison between the measured displacement and the corresponding pressure wave. The upper line is the measured pressure wave

with a piezoelectric detector; the middle line is the calculated displacement wave from the experimental data of the upper line. The bottom line is the displacement measured with the dual polarization interferometer. For the calculation of the displacement from the measured pressure, the following equation is used:

$$u(t) = -\frac{2v}{B} \int_{t=0}^{t} p(t)dt \tag{2.18}$$

where u(t) is the displacement signal, p(t) the pressure signal, B the bulk modulus of water, v the sound velocity in water. A reflection R = –1 at the object-air interface has been taken into account, assuming a total reflection of the acoustic wave at the interface (air has a much lower acoustic impedance than liquids, resulting in a reflection close to -1).

The middle and bottom time trace in Figure 2.25 are equally shaped, which indicates a validation of the calculation of the displacement signal from the measured pressure signal. The experimental displacement signal is slightly broadened, compared with the calculated displacement signal. This might be caused by acoustic interference at the rough interface (unpolished tape).

The RMS noise level of the interferometer was 3 times the fundamental shot noise limitation. Furhermore, the use of the tape resulted in an interference signal with 20% visibility (or, a five times lower interference amplitude than the theoretical maximum). These two factors increase the minimum detectable displacement by a factor 15 to 0.8 nm.

Mechanical vibrations and environmental noise incident to a flexible surface of measurement, given by the 1 cm^2 of tape, are expected to influence the stability of the system. Therefore the stability was investigated by determining the deviation in the sensitivity of the system in a noisy environment. The signals of branch 1 and 2 were added after determining their signs, and the deviation in the peak-to-peak values of 50 measurements was calculated. Figure 2.26 shows a 30% standard deviation in the sensitivity of the system (instead of the theoretical expected deviation of 13%). It can be concluded that environmental noise increases the deviation from the average sensitivity. This can be further reduced by reducing the size of the entire interferometer.
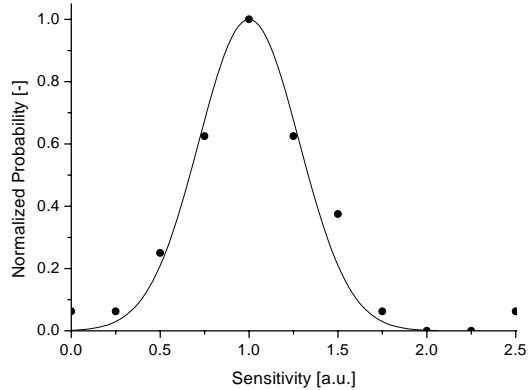
Figure 2.26 *Deviation in sensitivity for 50 measurements. The solid line is a gaussian fit through the data.*

The constructed dual-polarization interferometer shows that it can be used to detect displacements at an interface, caused by photoacoustic waves. Furthermore, it is insensitive to variations in object-interferometer distance and it reveals a nearly constant sensitivity, without the need of tuning the interferometer.

By replacing the photo-diodes in the two arms of the interferometer with fast CMOS-cameras, where each pixel can be addressed separately, a 2D image of the displacement of the interface can be recorded, without the need of scanning over the interface. This enables detection of the entire time-trace per pixel or flight-time (or depth) windowing of the signal, as is the case with other existing 2D camera detectors for PA. This makes this method suitable in cases where a non-contact method of detection of the photoacoustic waves is required.

The sensitivity of broadband piezoelectric transducers is expected to be slightly better than the sensitivity of interferometric sensors, covering a comparable bandwidth.[22,23] However, promising applications, like large area non-contact detection with the use of fast cameras are in favour of interferometric detection.

2.10 *References*

1. C.G.A. Hoelen, A. Dekker, and F.F.M. de Mul, "Detection of photoacoustic transients originating from microstructures in optically diffuse media such as biological tissue", *IEEE Trans. Ultrason., Ferroelect., Freq. Contr.*, vol 48 (1), pp. 37-47, 2001.

2. A.A. Oraevsky, and A.A. Karabutov, "Ultimate sensitivity of time resolved opto-acoustic detection", in *Biomedical Optoacoustics*, A.A. Oraevsky Ed., Proc. SPIE vol. 3916, pp. 228-239, 2000.

3. K.P. Köstli, M. Frenz, H.P. Weber, G. Paltauf, and H. Schmidt-Kloiber, "Pulsed optoacoustic tomography of soft tissue with a piezoelectric ring sensor", in *Biomedical Optoacoustics*, A.A. Oraevsky Ed., Proc. SPIE vol. 3916, pp. 67-74, 2000.

4. J.A. Viator, G. Au, G. Paltauf, S.L. Jacques, S.A. Prahl, H. Ren, Z. Chen, and J.S. Nelson, "Clinical testing of a photoacoustic probe for port wine stain depth determination", *Lasers Surg. Med.*, vol. 30, pp. 141-148, 2002.

5. P.C. Beard, F. Perennes, and T.N. Mills, "Transduction mechanisms of the Fabry-Perot polymer film sensing concept, for wideband ultrasound detection", *IEEE Trans. Ultrason., Ferroelect., Freq. Contr.*, vol 46 (6), pp. 1575-1582, 1999.

6. P.C. Beard, A.M. Hurrel, and T.N. Mills, "Characterization of a polymer film optical fiber hydrophone for use in the range 1 to 20 MHz: a comparison with PVDF needle and membrane hydrophones", *IEEE Trans. Ultrason., Ferroelect., Freq. Contr.*, vol 47 (1), pp. 256-264, 2000.

7. P.C. Beard, and T.N. Mills, "An optical detection system for biomedical photoacoustic imaging", in *Biomedical Optoacoustics*, A.A. Oraevsky Ed., Proc. SPIE vol. 3916, pp. 100-109, 2000.

8. G. Paltauf, H. Schmidt-Kloiber, K.P. Köstli, and M. Frenz, "Optical method for two-dimensional ultrasonic detection", *Appl. Phys. Lett.*, vol. 75 (8), pp. 1048-1050, 1999.

9. G. Paltauf, H. Schmidt-Kloiber, K.P. Köstli, M. Frenz, and H.P. Weber, "Optoacoustic imaging using two-dimensional ultrasonic detection", in *Biomedical Optoacoustics*, A.A. Oraevsky Ed., Proc. SPIE vol. 3916, pp. 240-248, 2000.

10. K.P. Köstli, M. Frenz, P. Weber, G. Paltauf, and H. Schmidt-Kloiber, "Optoacoustic tomography: time-gated measurement of pressure distributions and image reconstruction", *Applied Optics*, vol 40 (22), pp. 3800-3809, 2001.

11. S.L. Jacques, P.E. Andersen, S.G. Hanson, and L.R. Lindvold, "Non-contact detection of laser-induced acoustic waves from buried absorbing objects using a dual-beam common path interferometer", in *Laser-Tissue Ineraction IX*, S.L. Jacques Ed., Proc. SPIE vol. 3254, pp. 307-318, 1998.

12. P.E. Andersen, S.G. Hanson, and S.L. Jacques, "Photoacoustic imaging of buried objects using an all-optical detection scheme", in *Laser-Tissue Ineraction X*, S.L. Jacques Ed., Proc. SPIE vol. 3601, pp. 303-309, 1999.

13. V.M Ristic, "Principles of acoustic devices", J. Wiley & Sons, New York, 1983.

14. W.P. Mason, "Piezoelectric crystals and their application to ultrasonics", D. van Nostrand company Inc., New York, 1950.
15. P.N.T. Wells, "Biomedical ultrasonics", Academic press, London, 1977.
16. M.G. Silk, "Ultrasonic transducers for non-destructive testing", Adam Hilger Ltd, Bristol, 1984.
17. R.G.M. Kolkman, M.C. Pilatou, E. Hondebrink, and F.F.M. de Mul, "Photo-acoustic A-scanning and monitoring of blood content in tissue", in *Biomedical Optoacoustics*, A.A. Oraevsky Ed., Proc. SPIE vol. 3916, pp. 76-83, 2000.
18. C.G.A. Hoelen, and F.F.M. de Mul, "A new theoretical approach to photoacoustic signal generation", *J. Acoust. Soc. Am.*, vol. 106 (2), pp. 695-706, 1999.
19. M.W. Sigrist and F.K. Kneubühl, "Laser generated stress waves in liquids", *J. Acoust. Soc. Am.*, vol. 64, pp. 1652-1663, 1978.
20. F.F.M. de Mul, M.H. Koelink, M.L. Kok, P.J. Harmsma, J. Greve, R. Graaff, and J.G. Aarnoudse, "Laser Doppler velocimetry and Monte Carlo simulations on models for blood perfusion in tissue", *Applied Optics*, vol. 34, pp. 6591-6611, 1995.
21. T. Kubota, M. Nara, and T. Yoshino, "Interferometer for measuring displacement and distance", *Optics Letters*, vol. 12 (5), pp. 310-312, 1987.
22. C.B. Scruby, and L.E. Drain, "Laser Ultrasonics; Techniques and Applications", A. Hilger Ed., Bristol, 1990.
23. R.J. Dewhurst, C.E. Edwards, A.D.W. McKie, and S.B. Palmer, "Comparative study of wide-band ultrasonic transducers", *Ultrasonics*, vol. 25, pp. 315-321, 1987.

3 Experimental Photoacoustic Imaging and Monitoring

In this chapter we describe the set-up and equipment used to perform photoacoustic measurements. Results of photoacoustic experiments with phantoms, and in vivo experiments in animals and humans are discussed.

3.1 Photoacoustic set-up

To perform photoacoustic experiments a set-up is needed which consists of a light source, sensor, scanning mechanism and data-acquisition system. The set-up used to perform photoacoustic measurements in phantom and in *in vivo* experiments is shown in Figure 3.1.
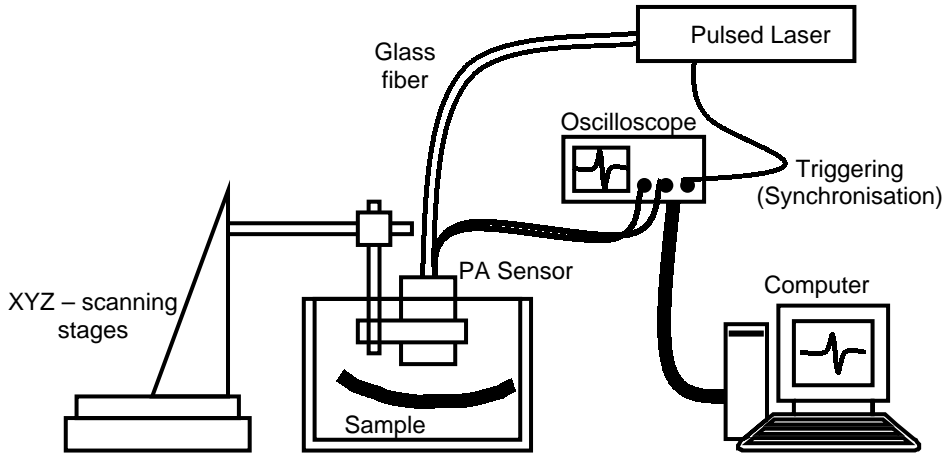
Figure 3.1 *Set-up, used to detect photoacoustic signals from absorbing structures (e.g. artificial blood vessels) in a container, filled with water or tissue mimicking fluid. The container can also be replaced with real tissue (e.g. a human arm) to perform in vivo experiments. The photoacoustic sensor can be scanned in XYZ-direction with respect to the object.*

To generate photoacoustic signals, a pulsed light source is required. If this light source generates pulses with a pulse-duration shorter than the acoustic transit time ($=\delta/\nu$) of the acoustic source (ν is the acoustic velocity, δ is the optical penetration depth, assuming that the beam diameter is much larger than δ) the condition of stress confinement is fulfilled. In this case the initial pressure distribution is proportional to the deposited energy density.[1] The wavelength of the source has to correspond with maximum photoacoustic signal generation and maximum penetration of the light into tissue (see also paragraph 3.2). The light sources used are Q-switched Nd:YAG lasers, which generate light pulses with a duration between 6 and 15 ns, and a repetition rate of 10-50 Hz, depending on the used Nd:YAG laser system (Brilliant B, Quantel + OPO, Opotek Inc.; LS2139, Lotis TII; Quanta Ray DCR-2, Spectra Physics). The pulse duration fulfils the requirements of stress confinement, when using photoacoustics to localize blood in the visible and near-infrared wavelength range. The available wavelengths were 1064 nm (first harmonic), 532 nm (second harmonic) and 690-950 nm (by using an optical parametric oscillator – OPO, Opotek). The available energy per pulse is dependent on the laser-system and wavelength (at least 80 mJ/pulse). The

light is coupled into a glass fiber, which is integrated in the photoacoustic sensor. To be able to scan the sensor over the sample, the sensor is mounted in an XYZ scanning system. The sample (e.g. artificial blood vessel) can be placed in a container, which can be filled with water or a tissue-mimicking fluid. Instead of using a container with a sample inside, the sensor can also be scanned over a tissue surface (e.g. human arm) to obtain an *in vivo* experiment. Acoustic coupling between the tissue surface and photoacoustic sensor is in this case obtained by using an optical transparent ultrasound contact gel (Sonogel[®], Germany). The photoacoustic signals are collected by a dual channel, digital oscilloscope (TDS220 – Tektronix, 1Gsample/sec, 100 MHz bandwidth). The results of the experiments described in this chapter are acquired at a sample rate of 250 Msamples/sec, unless otherwise stated. The acquisition is synchronised (triggered) on the Q-switch trigger, generated by the laser. The delay between the Q-switch trigger and the actual light pulse, exiting the fiber inside the photoacoustic sensor, is corrected by applying a delay to the Q-switch trigger pulse, before it synchronises (triggers) the oscilloscope. Besides using an oscilloscope, also a dual channel 100 Msample/sec oscilloscope-card (NI5112 – National instruments) has been used. The acquired data is transferred to a computer, where it is further processed using Labview (National Instruments).

The advantage of using an oscilloscope-card instead of an oscilloscope is the reduced data transfer time. When using the oscilloscope, the data transfer time to the computer, for 2 channels (IEEE.488 protocol) is about 1 sec, while the oscilloscope card reduces this time to about 5 msec.

3.2 Phantom materials

To perform photoacoustic measurements in a laboratory set-up, phantom materials are needed to simulate *in-vivo* measurements. These phantom materials need to have optical and acoustical properties, which correspond with real tissue.

3.2.1 Acoustic properties of biological tissue

The acoustic properties of biological tissue are characterized by acoustic impedance, speed of sound and attenuation.[2]

The *attenuation* of ultrasound consists of scattering and absorption losses. The attenuation coefficient α is usually expressed in decibels per centimetre [dB cm^{-1}]. For soft biological tissues[2,15] the relation between the attenuation and the frequency f is given by $\alpha \approx af^{b}$, where b has a value little greater than unity for frequencies in the range of about 0.1-50 MHz. In this region the value for a is for most soft tissues in the range from 0.2-1.5 [dB cm^{-1} MHz^{-b}], with f being expressed in MHz. For still higher frequencies (larger than about 100 MHz) the

water absorption starts to dominate, giving an attenuation proportional to f^2 (*b*=2). The value of *a* for water is about 0.002 [dB cm^{-1} MHz^{-2}], with *f* given in MHz.[2,15]

For most soft tissues, the *speed of sound* [2,15,13] ranges from about 1450 m/s to 1600 m/s, whereas the sound speed in water[15,13] is about 1480 m/s.

The *acoustic impedance* Z of soft tissue[15] ranges from about 1.3-1.7 [10^6 kg m^{-2} s^{-1}]. The acoustic impedance of water[15,13] is 1.5. The change in acoustic impedance across the interface of two materials determines the sound amplitudes that are transmitted and reflected at this interface (see also paragraph 2.2.3).

As water has acoustic properties close to the acoustic properties of tissue, a water-like phantom will be suitable for acoustic measurements. The largest difference in acoustic properties will be caused by the attenuation of ultrasound, which is larger in tissue. For 10 MHz, the penetration depth in infant brain (1/e decrease of amplitude) is about 3 cm, whereas water[2] at this frequency has a penetration depth of about 40 cm. As the geometrical attenuation of ultrasound is large (as shown in Figure 2.14), at least larger than the attenuation by the tissue, the attenuation by the tissue can be neglected at these distances. So water-like media can be used as acoustic phantoms, despite the lower value of the attenuation coefficient.

3.2.2 Tissue optical properties

A photoacoustic phantom should also match the optical properties of the tissue. These optical properties can be characterized by the absorption coefficient μ_a, the reduced scattering coefficient μ_s' and anisotropy factor g (average cosine of the scattering angle).

The penetration of light into the tissue is determined by these parameters and can be calculated by using e.g. the diffusion approximation[6,7,8,9,25] or can be simulated with Monte-Carlo simulations.[10] For a point source in a scattering and weakly absorbing, homogeneous medium, the energy fluence rate ψ [W/m^2] as a function of distance r to the source can, according to the diffusion approximation, be described by[6,7,8,9,25]

$$\psi(r) = \frac{\psi_0}{r}\exp(-\mu_{eff}r) \quad ; \quad \psi_0 = \frac{3\mu_{tr}}{4\pi}Q_0 \tag{3.1}$$

with Q_0 the power of the point source, μ_{eff} the effective attenuation coefficient, and μ_{tr} the transport coefficient, given by

$$\mu_{eff} = \sqrt{3\mu_a\mu_{tr}} \quad ; \quad \mu_{tr} = \mu_a + \mu_s'. \tag{3.2}$$

$1/\mu_{eff}$ is often referred to as the effective mean free path or the optical penetration depth.

Table 3.1 *Optical properties derived from literature for various tissue types.*

Tissue Type	Sample	λ [nm]	μ_a [mm^{-1}]	μ_s' [mm^{-1}]
neonatal white matter[11]	in vitro	650-900	0.04-0.07	0.5-1.2
neonatal gray matter[11]	in vitro	650-900	0.04-0.08	0.4-0.9
adult skull[12]	in vivo	849	0.022	0.91
adult white matter[12]	in vivo	849	0.013	0.98
adult white matter[11]	in vitro	650-900	0.02-0.03	8-10
adult white matter[13]	in vitro	1064	0.32	6.0
adult gray matter[12]	in vivo	811	0.018-0.019	0.48-0.74
adult gray matter[12]	in vivo	849	0.018-0.019	0.45-0.74
adult gray matter[11]	in vitro	650-900	0.04-0.06	1.9-2.2
adult gray matter[13]	in vitro	1064	0.50	1.2
Caucasian skin (epidermis+dermis)[14]	ex vivo	800	0.013	1.9
Negroid skin (epidermis+dermis)[14]	ex vivo	800	0.079	2.13
Human dermis[20]	in vivo	940	0.020-0.035	0.8-1.1
Breast tissue[15]	in vivo	800	0.002-0.003	0.72-1.22
Breast tissue (glandular)[17]	in vitro	700	0.047	1.42
Breast tissue (glandular)[17]	in vitro	900	0.062	0.99
Breast tissue (adipose)[17]	in vitro	700	0.070	0.86
Breast tissue (adipose)[17]	in vitro	900	0.075	0.79
Human abdomen[18]	in vivo	811	0.006-0.008	0.88-0.93
Human abdomen[18]	in vivo	849	0.007-0.008	0.88-0.91
Rabbit skin (epidermis+dermis)[16]	in vitro	790	0.070	1.84
Piglet skin (epidermis + dermis)[16]	in vitro	790	0.24	1.93
Piglet skin (epidermis + dermis)[16]	in vitro	850	0.16	1.43

In literature there is a lot of discussion about the optical properties of various types of tissue, as there is a lot of spread in the determined values for the reduced scattering coefficient and absorption coefficient. In Table 3.1 an overview is given of optical properties of various tissue types.

Variation between optical properties determined *in vitro* and *in vivo* are most likely to be caused by differences in sample preparation, when measuring *in vitro*. An important parameter, which is dependent on sample preparation, will be the water content of the tissue. Furthermore, blood drainage and structural alterations will influence the results of the *in vitro* measurements. Roggan et al.[19] found significant deviations in optical properties of porcine liver for different tissue preparation techniques. They concluded that it is very important to control

the preparation condition in order to determine reliable optical parameters for biological soft tissue. Graaff et al.[20] have shown that substantial inconsistencies exist between optical properties of human dermis determined *in vitro* and *in vivo*. The measured values for the absorption and reduced scattering coefficient are significantly lower when measured *in vivo*. They concluded that *in vitro* measurements will probably be more successful when measuring procedures are optimised and when the problems related to the sample treatment are solved.

The penetration of light into tissue can be described by the effective mean free path, which increases with decreasing absorption and scattering coefficients. As the scattering coefficient of tissue decreases with wavelength, the penetration of light increases. So shifting to larger wavelengths is in favour of the penetration depth of the light.

To generate photoacoustic signals from blood, the light has to be absorbed by it. The amplitude of the photoacoustic signal is proportional to the *absorption contrast* between blood and tissue ($\mu_{a,blood}$-$\mu_{a,tissue}$). This means that the wavelength to be used has to be chosen such that this absorption contrast is maximized.

In Figure 3.2 we show the absorption spectra of oxygenized and de-oxygenized hemoglobin[21], water[21], and bloodless dermis[22], together with the absorption coefficients of breast tissue[15,17], and adult gray- and white-matter.[11,12,13]
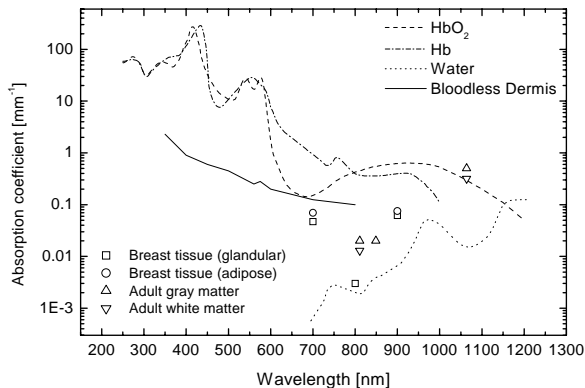
Figure 3.2 *Absorption spectra of oxygenized and de-oxygenized hemoglobin[21], water[21], and bloodless dermis[22], together with the absorption coefficients of breast tissue[15,17], and adult gray- and white-matter.[11,12,13]*

The optical penetration depth $1/\mu_{eff}$ has been calculated (Figure 3.3) using the data of Figure 3.2 and Table 3.1. In this calculation we assumed a blood volume in tissue of 5% and an oxygenation of blood of 80%. Furthermore, the water content of tissue is taken to be 80 %. The wavelength dependence of the reduced scattering coefficient is modeled[23] by $\lambda^{-0.37}$, with a value of 0.75 mm^{-1} at a wavelength of 800 nm.

Figure 3.3 *Calculated optical penetration depth ($1/\mu_{eff}$) of light into tissue. Blood volume: 5%, oxygenation 80%, water content 80%, reduced scattering coefficient (μ_s') at 800 nm: 0.75 mm^{-1}, wavelength dependence μ_s': $\lambda^{-0.37}$.*

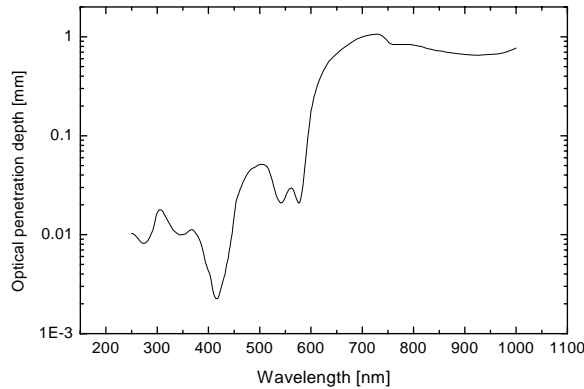In the blue (400-450 nm) and green (520-580 nm) range the absorption contrast is relatively large. However, the scattering of light by tissue and also the absorption by blood in this region is relatively high, which limits the penetration depth. When shifting to the near-infrared (700-900 nm), the absorption contrast decreases, whereas the penetration of the light into the tissue increases significantly (Figure 3.3). Shifting further to the infrared, the water absorption increases, which limits the absorption contrast. At 1064 nm, the water absorption has a local minimum, so this wavelength can also be used. For deep photoacoustic measurements, with a reasonable absorption contrast, a wavelength in the 700-900nm range seems to be optimal. The most favorable wavelength is about 800 nm, because at this wavelength, called isobestic point, the oxygenized and de-oxygenized hemoglobin have the same absorption coefficient. This implies that at this wavelength the generated photoacoustic signals are not dependent on the oxygenation of the blood. On the other hand, the difference in absorption spectrum of oxygenized and de-oxygenized blood can also be used in photoacoustics to determine the oxygenation of the blood (photoacoustic spectroscopy).

3.2.3 Intralipid as a photoacoustic tissue phantom

A suitable phantom to be used with photoacoustic measurements can be an Intralipid-solution. Intralipid is an intravenous nutrient consisting of an emulsion of fat in water. It is widely used as an optical phantom, as it is a highly scattering suspension with low absorption.[24,25,26] The liquid nature of the phantom facilitates independent variation of the optical properties.

Intralipid consists of approximately spherical particles of soyabean oil, surrounded by a lipid monolayer. In water these particles become vesicles surrounded by a monolayer of lecithin with a thickness of 2.5-5 nm. The mean diameter of these vesicles is about 100 nm.[25] Intralipid is available in various stock solution concentrations, mostly 10 or 20%. When mentioning a dilution of Intralipid, it is useful to mention the concentration of the stock solution, otherwise it is not clear whether the concentration of the stock solution influences the final optical properties. The optical properties of Intralipid-10% in the wavelength range from 400-1100 nm can be calculated using a model described by van Staveren et al.[25]:

$$\mu_s(\lambda) = \frac{0.016}{\lambda^{2.4}}\left[\frac{mm^{-1}}{ml/l}\right] \quad ; \quad g(\lambda) = 1.1 - 0.58\lambda \qquad (3.3)$$

This model can be used in a concentration range of ~17% to ~4% Intralipid-10% in the wavelength range of 400-1100 nm, with an uncertainty in optical properties of about 6%. The absorption of Intralipid in the wavelength range above 700 nm can be described by water absorption.[26] The optical properties for a 7.5% Intralipid-10% dilution as a function of the wavelength, according to the relations given by van Staveren et al.[25], are given in Figure 3.4.
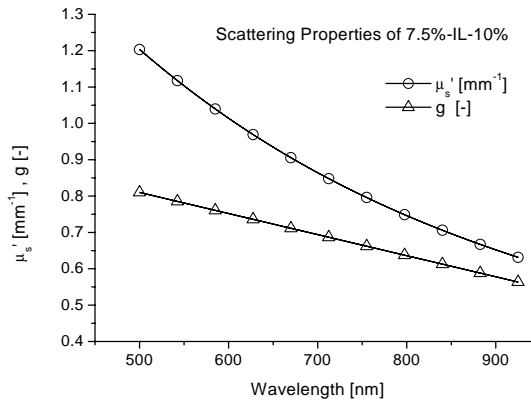
Figure 3.4 *Reduced scattering coefficient and absorption coefficient of 7.5% Intralipid-10% as a function of wavelength, according to the model given by van Staveren et al.[25]*

At a wavelength of 800 nm, the reduced scattering coefficient of 7.5% Intralipid-10% corresponds quite well with the values for real tissue (about 0.75 mm^{-1}) as presented in Table 3.1. The absorption of the Intralipid solution can be adjusted to the desired value by adding a dye, e.g. Indocyanine green (ICG). ICG is a dye of which the absorption spectrum depends on the nature of the solvent

medium and on the dye concentration. In general the absorption spectrum ranges from about 650-850 nm.[28]

Intralipid consists mainly of water, so the acoustical properties will be similar to the acoustic properties of water. As the acoustic properties of water are close to the acoustic properties of tissue (see section 3.2.1), Intralipid is a suitable tissue phantom for photoacoustic measurements.

3.2.4 Artificial blood vessels

Silicone rubber tubes filled with flowing human blood were used to mimic blood vessels in the tissue phantom. Depending on the exact type of silicone rubber, the acoustic impedance Z ranges from about 1.1 to 1.5 [10^6 kg m^{-2} s^{-1}]. As blood has an acoustic impedance[27] of 1.61, the amplitude reflection for normal incidence at the blood - silicone rubber interface will be 3 - 19%, whereas the amplitude reflection at a muscle (vessel wall) - blood interface is about 3%. When interpreting the detected photoacoustic signals, care has to be taken of these reflections.

Human blood can also be replaced by a dye, which has the same absorption as blood. However, the dye should not stain the inner wall of the silicone rubber tubing, as in that case the walls of the tube are acting as a photoacoustic source rather than the blood-mimicking dye inside the tube. As this was difficult to realize, human blood was preferred over a dye. The blood was anti-coagulated with EDTA or Lithium heparin. The blood was kept flowing during the measurement to avoid sedimentation of the red blood cells in the artificial blood vessel.

3.2.5 Conclusions

We have shown that Intralipid is a suitable photoacoustic tissue phantom as it can match both optical and acoustic properties of tissue. The optical properties can be adjusted by changing the concentration of the Intralipid dilution and by adding dyes. The acoustic properties of Intralipid resemble those of water that has acoustic properties close to those of tissue, except that it has a lower attenuation coefficient than tissue. At detection distances up to a few centimeters, the geometrical attenuation of ultrasound is much larger than the attenuation by the tissue, so the attenuation by the tissue can be neglected.

Blood vessels can be mimicked using silicone rubber tubes filled with anti-coagulated, flowing blood. Instead of blood also a dye can be used, but care has to be taken not to stain the inner wall of the tubing. The difference in acoustic properties between blood and silicone rubber gives rise to reflections, which are in the same order of magnitude as in real blood vessels. One has to take these reflections into account when interpreting the measured photoacoustic signals.

3.3 *Photoacoustic measurements on artificial blood vessels*

Phantom experiments have been performed to investigate the ability of the constructed sensor to localize and image (artificial) blood vessels and to investigate the sensitivity to vessel diameter (amount of blood).

3.3.1 Imaging

A silicone rubber tube filled with flowing human blood (anti coagulated with Lithium heparin) was immersed in a 7.5% Intralipid-10% dilution. The internal diameter of the tube was 1 mm, with a wall thickness of 0.5 mm. The tubing was positioned at a depth of 7 mm and was illuminated by a fiber in the center of the photoacoustic sensor (see chapter 2). The sensor used a 25 μm thick PVdF film to detect the photoacoustic waves. A pulse energy of 1 mJ was applied, with a pulse duration of 8 ns, at a wavelength of 800 nm and a repetition rate of 10 Hz. The signals detected by the sensor were averaged 128 times, before being transferred to the computer. A linear-scan perpendicular to the tubing has been made, consisting of 51 measurement positions, with 100 μm spacing.

The sensor has a directional sensitivity, which is very narrow (chapter 2, Figure 2.12, Figure 2.13). So each photoacoustic time trace can be considered as a 1D image of the photoacoustic sources inside the measurement volume. By multiplying the time with the speed of sound in the medium, the time can be converted to depth information.

As the measurement consists of a liner scan, a 2D image (scan direction vs. depth) can be obtained by plotting all 1D – depth images (i.e. time traces) next to each other. The bipolar photoacoustic signal contains information about the front (positive peak) and the back (negative peak) of the vessel. In the 2D-image the absolute value of the measured signal is plotted, showing both negative and positive peak as positive peaks in the image.

The resulting photoacoustic image is shown in Figure 3.5-A. When using the zero-time cross-correlation values (Figure 3.5-C) as weight factors (paragraph 2.4.2), the opening angle of the sensor reduces and smearing out of the image in lateral direction will be suppressed, as is shown in Figure 3.5-B.
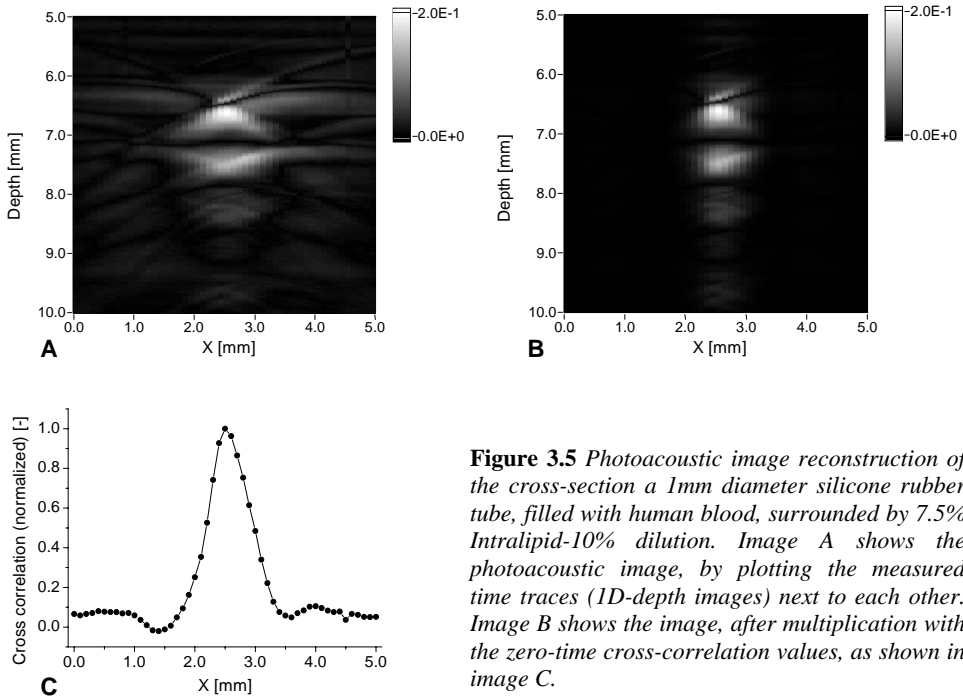
A

B

C

Figure 3.5 *Photoacoustic image reconstruction of the cross-section a 1mm diameter silicone rubber tube, filled with human blood, surrounded by 7.5% Intralipid-10% dilution. Image A shows the photoacoustic image, by plotting the measured time traces (1D-depth images) next to each other. Image B shows the image, after multiplication with the zero-time cross-correlation values, as shown in image C.*

The photoacoustic signal, generated by a cylindrically symmetrical source can be calculated numerically, using the models described by Hoelen et al.[5] or Lai and Young.[29] However, there is no simple analytic expression available to describe the signal generated by a cylindrically symmetrical source. Therefore we will use the model of a spherical photoacoustic source, as described by Sigrist et al.[30] and Hoelen et al.[5], as an approximation of a cylindrical source. This model gives the far field approximation (detection distance >> 1/e-radius of the Gaussian absorption distribution, see also paragraph 2.3) of a spherical source with a 3-dimensional Gaussian absorption distribution.

The mayor assumption in this model is that after heating (laser pulse) the source has an initial Gaussian heat distribution, equal to the Gaussian absorption distribution.[5] It is assumed that the light intensity is not attenuated, when a part is being absorbed by the absorption distribution (1st Born approximation). This requires that the radius of the blood vessel has to be of the same order of magnitude, or smaller than the absorption-mean-free-path ($=1/\mu_{a,blood}$). For larger radii of the blood vessels the light-intensity decays too much inside the vessel and only a shell of the blood will contribute to the photoacoustic signal. In these cases this model can no longer be used to approximate our photoacoustic signals. In case (near) infrared light is used (>700 nm), the absorption of blood will be less

than about 0.7 mm^{-1}. This results in a maximum vessel diameter, for which this approximation will hold, of about 3 mm.

A spherical photoacoustic source with a Gaussian absorption distribution will generate a signal[5] that can be characterized by three parameters: the peak-to-peak time τ_{pp}, the zero-crossing time t_0 and amplitude C:

$$P(t) = -2C(t - t_0)e^{\left(-\frac{1}{2}\left(\frac{t-t_0}{\frac{1}{2}\tau_{pp}}\right)^2\right)}$$

(3.4)

Figure 3.6 shows a measured photoacoustic time-trace of a 1 mm diameter silicone rubber tube filled with human blood, situated in a 7.5% IL-10% dilution, together with the bipolar fit. In Figure 3.7 the residual time trace is plotted, which is the difference after subtraction of the bipolar fit from the measured time trace. In this graph also a time trace is shown at position X=0 mm (see Figure 3.5), where there is no artificial blood vessel present in front of the transducer.

The measured photoacoustic time trace shows a large positive amplitude, which is not taken into account in the fit. Furthermore, the first slope of the photoacoustic signal is steeper than the slope of the fit. Nevertheless, the bipolar fit seems to be a reasonable approximation of the measurement. Besides the part that is approximated by the bipolar fit, also a sort of oscillations is present at a time larger than 5.3 µs. As can be seen from Figure 3.7 the amplitude of the oscillations is much higher than the fluctuations in the photoacoustic time trace when there is no artificial vessel present in front of the transducer. These oscillations are most likely to be reflections of the photoacoustic signal at the walls of the silicone rubber tube, as the peak-to-peak time of these oscillations is about equal to the peak-to-peak time of the main photoacoustic signal. The small negative peak that precedes the photoacoustic signal is present in all our measurements. A possible explanation could be radiation pressure, where there is a change of momentum upon reflection of light. This will result in a pressure wave consisting of first a rarefaction, followed by compression. However, the silicon rubber tubes do not have a very high reflection. As a result the amplitude of radiation pressure, compared to the photoacoustic pressure, is likely to be negligible. So the origin of this negative peak is not yet understood.
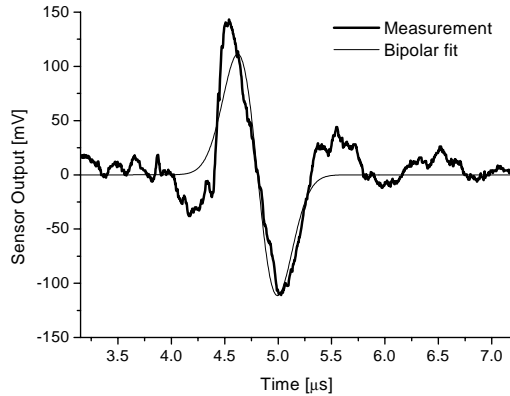
Figure 3.6 *Measured photoacoustic time trace for a 1 mm diameter silicone rubber tube filled with human blood situated in a 7.5% IL-10% dilution, together with the bipolar fit.*
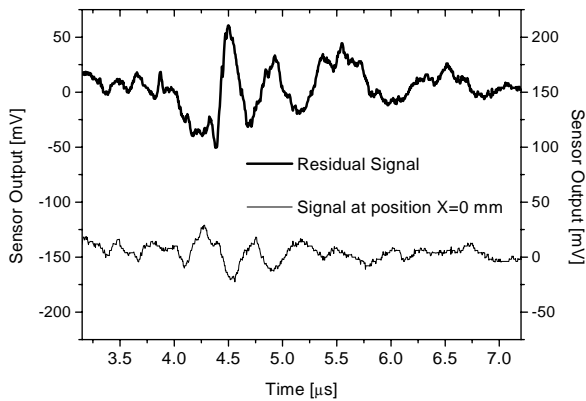
Figure 3.7 *Residual time trace when subtracting the bipolar fit from the measured time trace as shown in Figure 3.6, together with the photoacoustic time trace at position x = 0 mm (see Figure 3.5), where there is no artificial vessel present in front of the sensor.*

The pressure wave is the result of a thermal expansion process where light is absorbed in a restricted volume followed by thermal relaxation. Thus, the shape of the photoacoustic wave contains information about the absorption distribution in this volume. In case of a spherical photoacoustic source with a Gaussian absorption distribution, the integral over time of the ideal photoacoustic time trace gives the absorption distribution of the source. So when we integrate the bipolar fit, a first approximation of the absorption distribution $A(t)$ can be obtained:

$$A(t) = \int_0^t P(\tau)d\tau = \tfrac{1}{2} C\tau_{pp}^2 e^{\left(-\tfrac{1}{2}\left(\frac{t-t_0}{\tfrac{1}{2}\tau_{pp}}\right)^2\right)} \tag{3.5}$$

The absorption distribution A(t) is a Gaussian function, which can be characterized by its standard deviation or flex point σ (square root of the variance of the distribution), which is equal to ½ τ_{pp}. As we have used the signal of a spherical photoacoustic source as a model of the signals generated by a cylindrical source, the absorption distribution will contain information about the diameter of the vessel.

The result of the fit is shown in Figure 3.8-A, where the absolute value of the bipolar fit is plotted. In this way both positive and negative peaks are shown as positive peaks in the image, visualizing the front and back of the vessel. After fitting the bipolar signal to the measurement, the fit has been multiplied by the zero-time correlation factor to reduce broadening of the image.
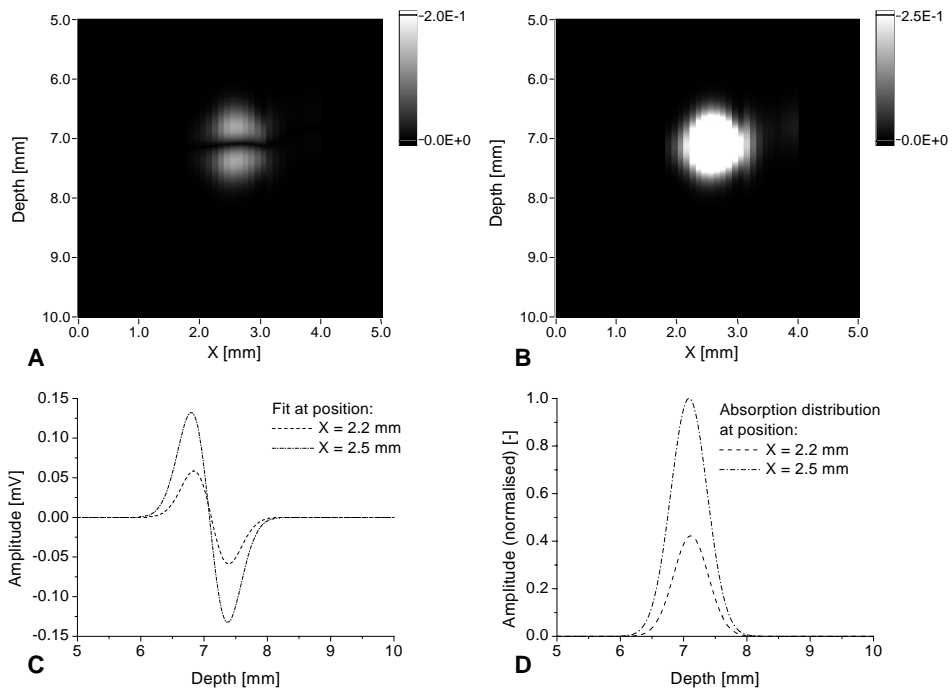
Figure 3.8 *Image A: photoacoustic image consisting of the bipolar fit to the measurement (Figure 3.6), including multiplication with the weight factors based on the zero-time cross-correlation. In the image the absolute value of the fit is plotted, showing both positive and negative peaks as positive peaks in the image. Image B: image of the absorption distribution, after integration of the bipolar fit as shown in the left panel. Cross-sections (in depth) of images A and B, at positions X = 2.2 mm and X = 2.5 mm, are shown in graphs C and D respectively.*

The corresponding absorption distribution is obtained by integrating the bipolar fit and is shown in Figure 3.8-B. In this image, also the zero-time cross correlation has been used as a weight factor.

In Figure 3.8-B the threshold is set to 25% of the maximum value, making everything above this threshold appearing as white in the image. This image shows that the circular shape of the artificial vessel is nicely reconstructed, without using prior knowledge about the shape of the vessel. The only assumption, which has been made, is that the photoacoustic time trace generated by a blood vessel can be approximated by a bipolar signal (derivative of a Gaussian function). Furthermore, each vertical line plotted in the image (Figure 3.8-C,D), is based on a measurement recorded in a single scanning position, which is independent of the next position.

3.3.2 Different vessel sizes

The experiments described in paragraph 3.3.1 have also been performed for different sizes of the silicone rubber tubes (artificial blood vessels), filled with flowing human blood.

Six different vessels have been used in this experiment, with dimensions of (inner x outer diameter, as specified by the manufacturer): 0.3x0.7; 0.5x1.0; 0.8x1.4; 1.0x2.0; 1.2x2.5; 1.5x2.1 mm. The vessels were situated in a 7.5% Intralipid-10% dilution, at a depth of 7 mm. A pulse energy of 1 mJ/pulse was used, with a pulse-duration of 8 ns, at a wavelength of 800 nm. All photoacoustic signals were averaged 128 times by the oscilloscope, before being transferred to the computer. A linear scan perpendicular to the artificial vessel has been performed, consisting of 51 measurement positions, with a spacing of 0.1 mm.

Figure 3.9 A to F show that the cross sections of the different vessels is nicely reconstructed.

A - ø = 0.3 mm

B - ø = 0.5 mm

C - ø = 0.8 mm

D - ø = 1.0 mm

E - ø = 1.2 mm

F - ø = 1.5 mm

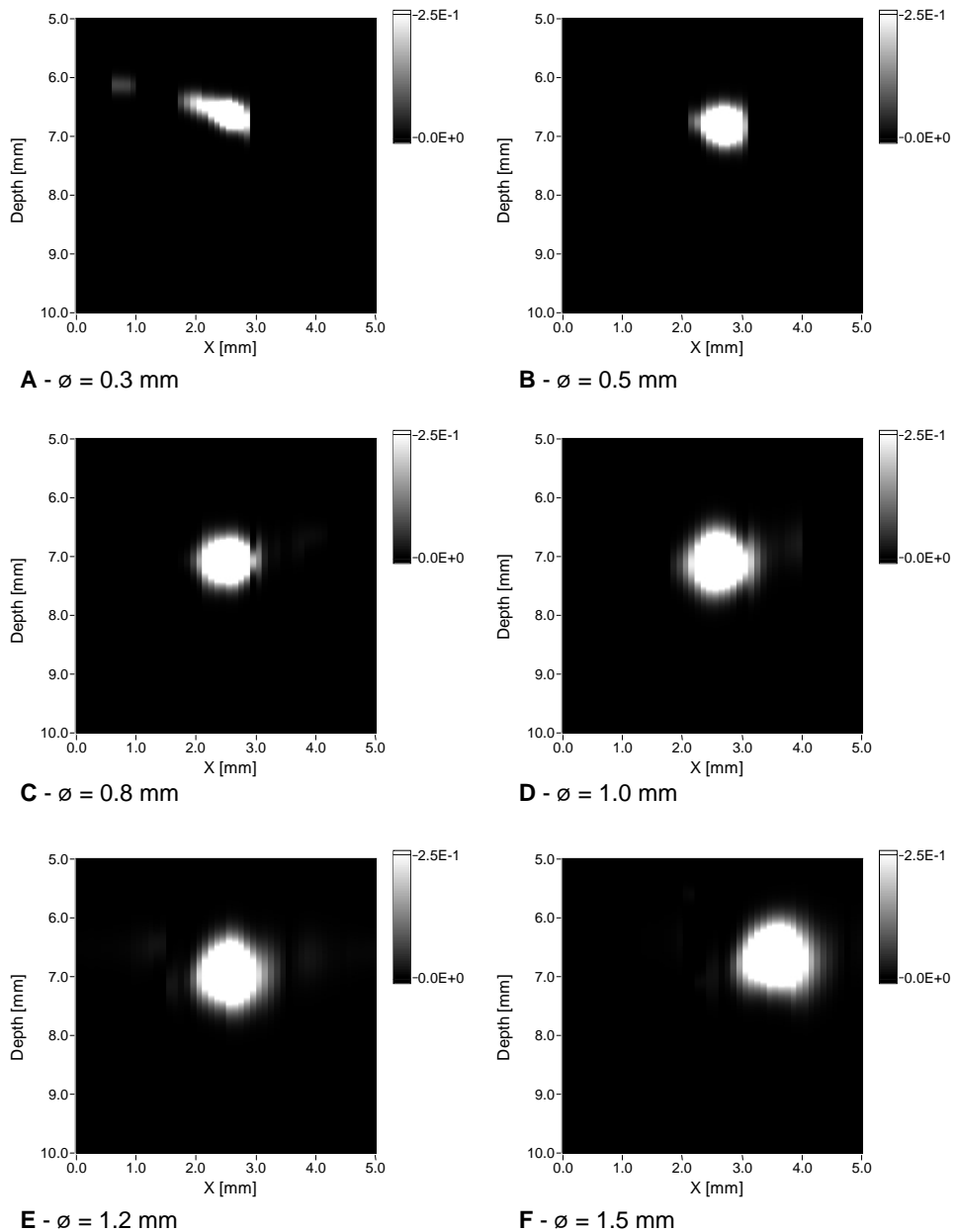**Figure 3.9** *photoacoustic reconstruction of the cross-section of artificial blood vessels, with six different inner diameters, filled with flowing human blood, and situated in 7.5% Intralipid-10%. Each scan (image) consists of 51 measurement positions along a line, with a spacing of 0.1 mm. A wavelength of 800 nm has been used, with a pulse energy of 1 mJ/pulse. All photoacoustic signals were averaged 128 times.*

From the images in Figure 3.9, the vessel diameter can be determined, by estimating the maximum peak-to-peak time τ_{pp}, which corresponds to the maximum size (diameter) of the cross-section through the vessel. In the images the absorption distribution is plotted, of which the *standard deviation* σ ($e^{-0.5}$ value of maximum amplitude) is equal to ½ τ_{pp}. Figure 3.10 shows this Gaussian absorption distribution, characterized by its standard deviation σ.
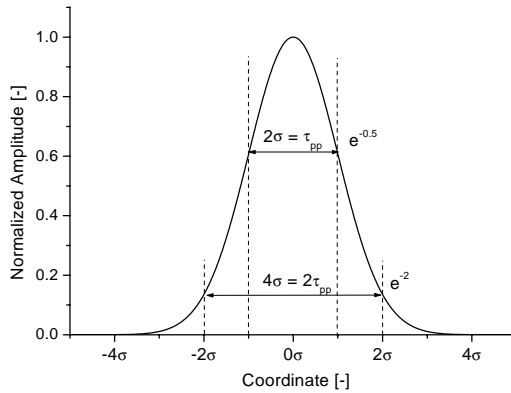
Figure 3.10 *Gaussian absorption distribution, characterized by its standard deviation σ, which is equal to ½ τ$_{pp}$.*

In a Gaussian function 95.4% of the area under the curve is covered between $\pm 2\sigma$ = $\pm\tau_{pp}$. This value is taken as a measure for the diameter of the artificial blood vessels, resulting in a diameter of $2\tau_{pp}\nu$, where ν is the acoustic velocity in the medium (Intralipid: $\nu = 1480$ m/s).

Figure 3.11 *Diameter of artificial blood vessels, estimated from the peak-to-peak time (2D images) versus the diameter, measured with a calibrated microscope. The solid line gives the expected one-to-one relation.*

The estimated diameter from the images is plotted versus the real diameter, measured with a calibrated microscope. The result is shown in Figure 3.11. The solid line shows the expected one-to-one relation between the estimated and real diameter.

The data-points in Figure 3.11 suggest that there is linear relation between the real diameter and the estimated diameter, other than the plotted one-to-one relation. This linear relation will have a smaller slope together with an offset.

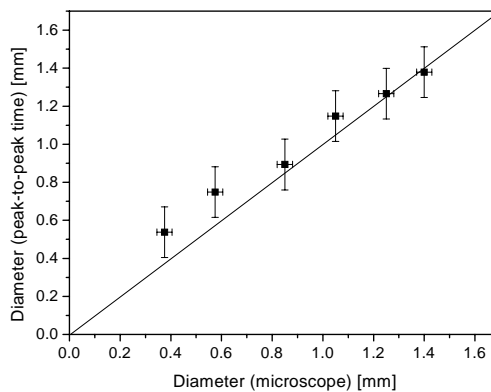The diameter estimated from peak-to-peak time is, within the error bars, in agreement with the values measured with a microscope. The two smallest vessels seem to give a value, which is slightly overestimated compared to the four largest vessels. However, these measurements show that the used model gives a reasonable estimation of the vessel diameter.

3.3.3 Orientation parallel to scan direction

Besides scanning (imaging) perpendicular to the orientation of the vessel, also a scan parallel to the vessel has been made. In this measurement, a 1 mm diameter silicone rubber tube, filled with flowing human blood was immersed in a 7.5% Intralipid-10% dilution at a depth of 6 mm. The linear scan consisted of 121 measurement positions, with a spacing of 50 μm. The vessel had a length that was much larger than the part of the vessel that has been imaged. The photoacoustic waves were generated by illuminating the sample with light pulses with an energy of 1 mJ/pulse, pulse-duration 8 ns, at a wavelength of 800 nm. The photoacoustic time traces were averaged 16 times by the oscilloscope, before being transferred to the computer.

Figure 3.12 *Photoacoustic image of a 1 mm diameter artificial blood vessel (silicone rubber tube), filled with flowing human blood, positioned parallel to the scanning direction. The scan consisted of 121 measurement positions, with a spacing of 50 μm. In this measurement a pulse energy of 1 mJ/pulse is used, pulse-duration 8 ns, at a wavelength of 800 nm. All photoacoustic signals were averaged 16 times.*

Figure 3.12 shows the photoacoustic image of this vessel. The diameter of the vessel in the image seems to decrease slightly, when scanning from left to right. This indicates that the vessel was not positioned exactly parallel to the scan direction. From the image can be calculated that the vessel is positioned at a tilting angle of 1° with respect to the scanning direction.

This experiment was repeated for a vessel with a gradually decreasing depth position. The measurement conditions were the same as the above-described experiment, except that the photoacoustic time traces were averaged 128 times in stead of 16 times. The scan consisted of 51 measurement positions, at a spacing of 0.25 mm.
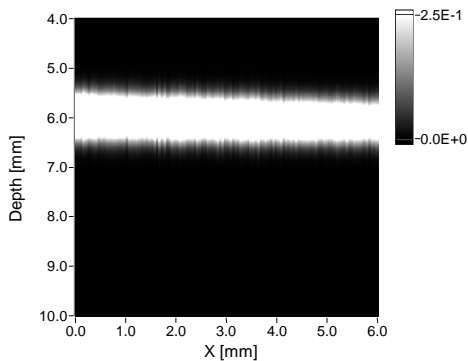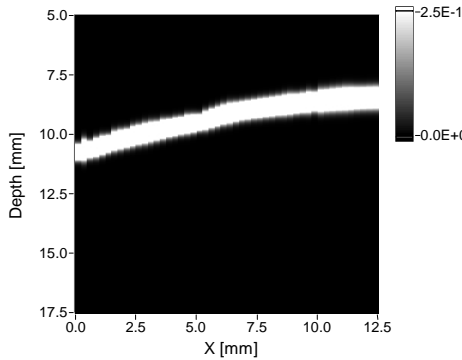

Figure 3.13 *Photoacoustic image of a 1 mm diameter artificial blood vessel (silicone rubber tube), filled with flowing human blood. The scan consisted of 51 measurement positions, with a spacing of 0.25 mm. In this measurement a pulse energy of 1 mJ/pulse is used, pulse-duration 8 ns, at a wavelength of 800 nm. All signals were averaged 128 times. Per measurement position (vertical line in 2D image), the signals were normalized to the maximum value, to correct for the decrease in amplitude, due to a decrease in light intensity with increasing depth, and geometrical attenuation of the ultrasound, together with the depth response of the photoacoustic sensor.*

Figure 3.13 shows the photoacoustic image of the artificial vessel. In this image all signals have been normalized to the maximum value per measurement position to correct for the decrease in amplitude with increasing depth of the vessel. This decrease in amplitude is caused by a decrease in light intensity with increasing depth. Furthermore the amplitude also decreases due to geometrical attenuation of the ultrasound, together with the depth response of the photoacoustic sensor (see also paragraph 2.3.3 & 2.5). The vessel is still clearly visible at a depth of about 11 mm in a 7.5% Intralipid-10% dilution. The diameter of the vessels seems to decrease with increasing depth, which is most likely caused by the fact that the positioning of the vessel was not exactly parallel to the scan direction. It is probably positioned at a tilting angle of a few degrees with respect to the scanning direction, as was also the case for the experiment shown in Figure 3.12.

3.3.4 Discussion and conclusions

We showed that the broadening of the photoacoustic image could be successfully reduced, using the zero-time cross-correlation as a weighting factor. In the way we applied this cross-correlation, knowledge about the velocity of sound in the medium is needed. The algorithm can be further improved determining the time delay corresponding to the maximum of the cross-correlation-function at the position exactly above the vessel. This time delay can then be used to determine the actual velocity of sound. In this way no knowledge

about the speed of sound is needed. Furthermore, the speed of sound will then automatically be corrected for inhomogeneities in tissue.

The model we used to reconstruct the absorption distribution is based on a spherical source, while we applied it to a cylindrical source. A model taking into account the cylindrical shape of the source can give a better reconstruction of the absorption distribution. The currently available models for cylindrical sources can only be calculated numerically, making it difficult to use these models to fit to the measured photoacoustic time traces. Although the model we used is an approximation, it showed that the cross-section of the artificial blood vessel is outstandingly well reconstructed.

Using the reconstructed absorption distribution, the diameter of the artificial blood vessels could be estimated. The diameter of the two smallest vessels was slightly overestimated. However, still the estimated diameter of the artificial blood vessels agreed with the actual diameter within the error bars. This shows the potential of photoacoustics to be used to determine the size of blood vessels. Furthermore it demonstrates that photoacoustics is sensitive to changes in vessel diameter, that is to say changes in blood content.

Imaging parallel to blood vessels shows that also in these cases the cross section of the vessel is nicely reconstructed.

3.4 Photoacoustics in rabbit ear[*]

In the previous section we presented images of artificial blood vessels in a tissue phantom. Experiments have been performed on blood vessels in the ear of a rabbit to explore the feasibility of photoacoustics to be used in *in vivo* imaging. These vessels were easily accessible, whereas the vessels also can be located by eye. In these experiments we will show that we are able to image blood vessels *in vivo*. Furthermore it will be shown that photoacoustics is able to monitor changes in vessel size, and we will prove that the main contribution to the photoacoustic signal is caused by blood inside the vessel and not by the vessel wall.

3.4.1 Materials and method

The Ethical Committee on Animal Research of the University of Nijmegen approved the experiments described in this work.

The rabbit (~2 kg) was anaesthetized and, after orotracheal intubation, mechanically ventilated. The ear of the rabbit was shaved and placed on foam rubber, while the gap between the ear and foam rubber was filled with ultrasound

---

[*] These experiments were carried out at the central animal laboratory of the University Medical Center in Nijmegen, in cooperation with J.H.G.M. Klaessens, J.C.W. Hopman, and J.M. Thijssen, Department of Paediatrics, Clinical Physics laboratory, University Medical Center Nijmegen.

contact gel (Sonogel®, Germany). To ensure a good acoustic coupling between the ear and the sensor, also this gap was filled with ultrasound contact gel.

Photoacoustic signals were generated by illuminating the ear by a fiber, which was positioned in the center of the photoacoustic sensor. The light pulses at a wavelength of 1064 nm had pulse duration of 15 ns, an energy of 1 mJ/pulse, with a repetition rate of 50 Hz. A photograph of the rabbit ear is shown in Figure 3.14.
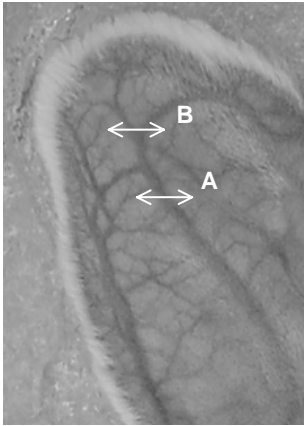
Figure 3.14 *Photograph of the rabbit-ear, placed on foam rubber. Hair has been removed. The blood vessel structure is clearly visible. The arrows indicate the regions where a scan has been made of the blood vessels.*

3.4.2 Imaging

An image of a vessel in the ear of the rabbit has been made by scanning the sensor along line A (Figure 3.14), with a step size of 0.1 mm, taking 61 measurements, while averaging the photoacoustic time traces 16 times per measurement. The distance between the ear and the sensor was about 6.5 mm, which was completely filled with ultrasound contact gel.

Figure 3.15 *Photoacoustic image of vessel in rabbit ear. The image consists of a scan of 61 measurements along a line, with a spacing of 0.1 mm between the detection-points. At each detection-point, 16 photoacoustic signals have been averaged.*

The photoacoustic image Figure 3.15 shows an elliptic cross-section of the vessel. Scanning not perpendicular to the vessel (see Figure 3.14) is most likely the reason of this ellipticity. The diameter (in depth) of the vessel is about 1 mm.

Another scan has been made, along line B (Figure 3.14), which shows two vessels close to each other. The scan consisted of 31 measurement positions along a line, with a step size of 0.1 mm. The resulting image is shown in Figure 3.16. The two vessels are indicated with 1 and 2.
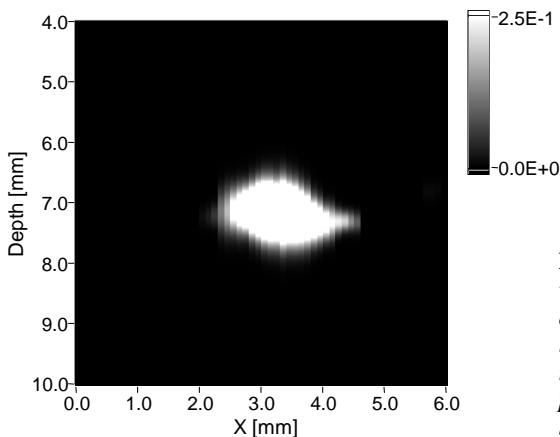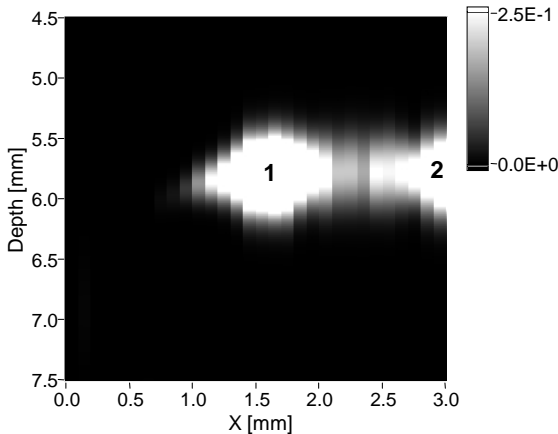

Figure 3.16 *Photoacoustic image of two vessels close to each other in rabbit ear. The image consists of a linear scan of 31 measurement positions, with a spacing of 0.1 mm between the detection-points. At each detection-point, 16 photoacoustic signals have been averaged.*

3.4.3 Monitoring blood content

After imaging these two vessels, the sensor was placed in one steady position above the center of vessel 1 in Figure 3.16, at position X=1.5 mm. To change the amount of blood in the vessel (vessel size), the vessel was alternately closed upstream (occlusion) and opened. During this experiment the photoacoustic signals have been measured continuously. Each photoacoustic signal, being transferred from oscilloscope to computer, consisted of an average of 16 independent photoacoustic signals, which were generated 50 times per second (repetition rate laser: 50 Hz). Including the data-transfer from the oscilloscope to the computer, the total time, for one photoacoustic signal of 16 averages, was about 1.3 sec.

When the vessel is closed upstream, a part of the blood will flow out of the vessel, decreasing the size of the vessel. As the photoacoustic signal contains information about the vessel size, characterized by the peak-to-peak time, a decrease in this peak-to-peak time is expected during occlusion.

Figure 3.17-right panel, shows the photoacoustic time traces during and after occlusion. A bipolar photoacoustic signal (as described in paragraph 3.3) has been fitted to these signals. The peak-to-peak time has been determined from the fitted signals and is shown in Figure 3.17-right panel. This graph shows that

during occlusion, the peak-to-peak time decreases, indicating a decrease of vessel size.
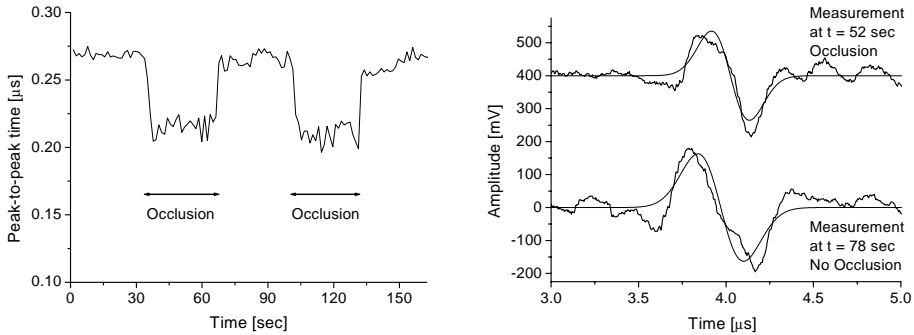

Figure 3.17 *Left panel: peak-to-peak time of the photoacoustic time traces during monitoring at one steady position above the vessel, while the vessel is alternately closed (occlusion) and opened. Right panel: photoacoustic time traces during (at t = 52 sec) and after (at t = 78 sec) occlusion, together with the bipolar fit (time trace during occlusion is shifted over 400 mV).*

3.4.4 Flushing with saline

To prove that the photoacoustic signal is primarily generated by blood and not by the vessel wall, a blood vessel has been flushed with saline, replacing the blood during a few seconds. Flushing with saline has been carried out by injection of saline inside the vessel, at a position upstream of the vessel, well outside the measurement site. The photoacoustic time traces have been recorded, and the results are shown in Figure 3.18.

Figure 3.18-right panel, shows the photoacoustic time traces of a vessel filled with blood, as well as the time trace of a vessel filled with saline. The main bipolar photoacoustic signal disappears almost completely when the blood is replaced by saline, proving that the photoacoustic signal is predominantly generated by blood. A small signal is still present, which is probably generated by small amounts of blood present in the vessel wall or the surrounding tissue.

Like in the experiment shown in Figure 3.6 and Figure 3.17, there are oscillations visible after the photoacoustic signal. A part of these oscillations will be caused by reflections at the vessel-wall – blood interface. However, in this case we placed foam rubber underneath the ear. This foam rubber consist of small cavities filled with air, that will act as reflectors for ultrasound. The oscillations are also visible, though with lower amplitude, when the blood is replaced by saline. So we expect that these are mainly caused by reflections at the foam rubber.

A bipolar signal has been fitted to the measured photoacoustic signals. The normalised amplitude of the fit as a function of time is plotted in the left panel of Figure 3.18. During the time that the vessel is flushed with saline the amplitude shows a distinct decrease, whereas it returns to the original value immediately when the flushing with saline is stopped.
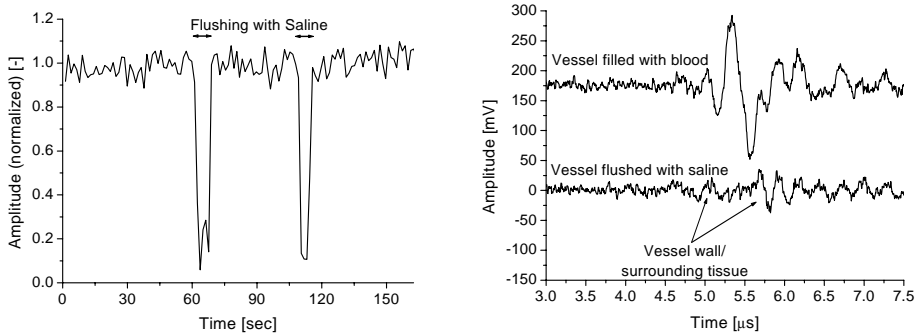
Figure 3.18 *Left panel: Normalised amplitude of photoacoustic signal during experiment in which blood vessel is flushed with saline. Right-panel (time trace of vessel filled with blood is shifted over 175 mV): photoacoustic time trace before flushing with saline (vessel filled with blood) and during flushing with saline.*

3.4.5 **Branching of vessels**

To visualize branching of vessels in the rabbit ear, a region with several vessels has been imaged. The scan consisted of 9 linear scans with a separation of 1 mm, each linear scan consisting of 61 measurement positions with a spacing of 0.3 mm. At each measurement position 16 photoacoustic time traces have been detected and averaged. Each linear scan gives a photoacoustic image, so the total scan consists of 9 images. The total scan time was about 30 minutes.

The region which has been imaged, is depicted in the photograph of the ear with a white rectangle (Figure 3.19-right panel). The left panel of Figure 3.19 shows the photoacoustic images, where it is obvious that the branching is visualized.
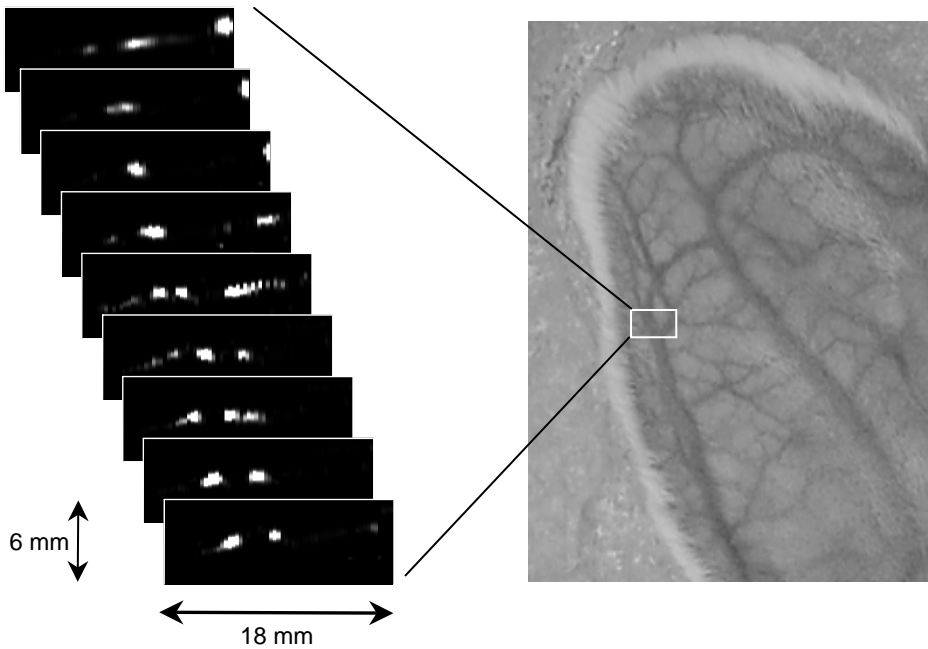
Figure 3.19 *Right-panel: photograph of rabbit ear. White rectangle shows the region, which has been imaged. Left panel: resulting photoacoustic images. Horizontal axis: scan direction [mm]; vertical axis: depth [mm]. Each image consists of 61 measurement positions along a line, with a separation of 0.3 mm. The distance between the images is 1 mm.*

3.4.6 Conclusions

We have shown to be able to visualize blood vessels *in vivo* in the ear of a rabbit. The cross-section of the blood vessels was nicely reconstructed. Furthermore we showed that changes in vessel size (amount of blood) could be detected while the vessel was repeatedly opened and closed (occlusion). By flushing the vessel with saline, replacing the blood for a short time, we proved that the photoacoustic signal is caused by blood inside the vessel and not the vessel-wall. Imaging of branching of vessels in the ear showed that the cross section could be reconstructed, visualizing also the branching of these vessels.

3.5 In vivo imaging in human wrist

In the previous section we have shown to be able to visualize the branching of blood vessels in the ear of a rabbit. These vessels were clearly visible by eye, whereas the rabbit was anaesthetized during the experiment. A next step is to visualize blood vessels *in vivo* in a man. We have chosen the branching of 2 veins in the lower side of the wrist. These vessels were visible vaguely through the skin.

3.5.1 Materials and method

An arm-support has been used to keep the arm in a stable position during the measurement, as shown in Figure 3.20. To keep the wrist in fixed position, a mould made of a thermoplastic sheet material (Efficast®, Orfit Industries) has been used.
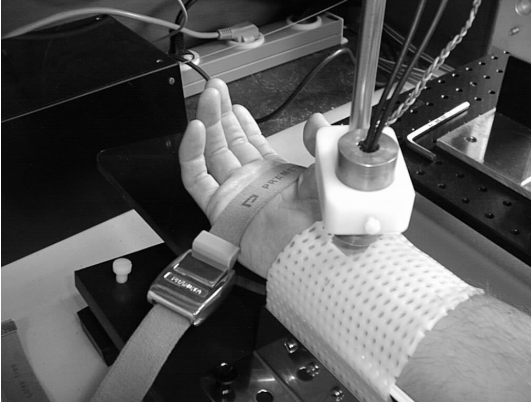
Figure 3.20 *Position of arm during scanning of the branching of two veins in the lower side of the wrist. To keep the wrist in a stable position, a mould of a thermoplastic sheet material (Efficast®, Orfit Industries) has been used.*

The measurement consisted of 9 linear scans (=9 2D-images), with a spacing of 1 mm. Each line (2D image) consists out of 31 measurement positions, with a spacing of 0.3 mm. At each measurement position the photoacoustic time traces were averaged 16 times. Total scan time: 20 minutes. Photoacoustic signals were generated by illuminating the tissue with 12 ns light pulses, with an energy of 1 mJ/pulse, and a wavelength of 1064 nm. The tissue was illuminated by a fiber, which was positioned in the center of the photoacoustic sensor. The gap between the sensor and the skin surface was filled with ultrasound contact gel (Sonogel®, Germany) to ensure a good acoustic coupling.

Taking into account the safety limits as mentioned in paragraph 2.7, the minimum required distance between fiber and sensor can be calculated. As during the measurement the sensor is being scanned, each time a different area is illuminated. So the measurement time T per measurement position is 1.6 sec (10 Hz repetition rate of the laser, 16 averages per measurement position). According to the safety limits, in this case, a maximum energy density is allowed of 10 mJ/cm^2. Using the NA of the fiber (0.22) and the refractive index of the ultrasound contact gel (n=1.3), the minimum required distance can be calculated to be 10 mm.

3.5.2 Results

In Figure 3.21 the photoacoustic image of the branching of two blood vessels in a human arm, a few cm upwards from the wrist is shown. A photograph of the scanned area is shown in the left panel. The photoacoustic reconstruction is

presented in the right panel. Besides the blood vessels, also the skin gives a photoacoustic signal, as there is a difference in optical absorption between the ultrasound contact gel (used as acoustic coupling medium between the skin and the sensor) and the skin. This figure shows that the cross section of blood vessels in the skin can be imaged, showing even the branching of the vessels. Visual inspection (photograph – left panel) shows a 2D image, determined by the outer diameter in top view of the vessels only.
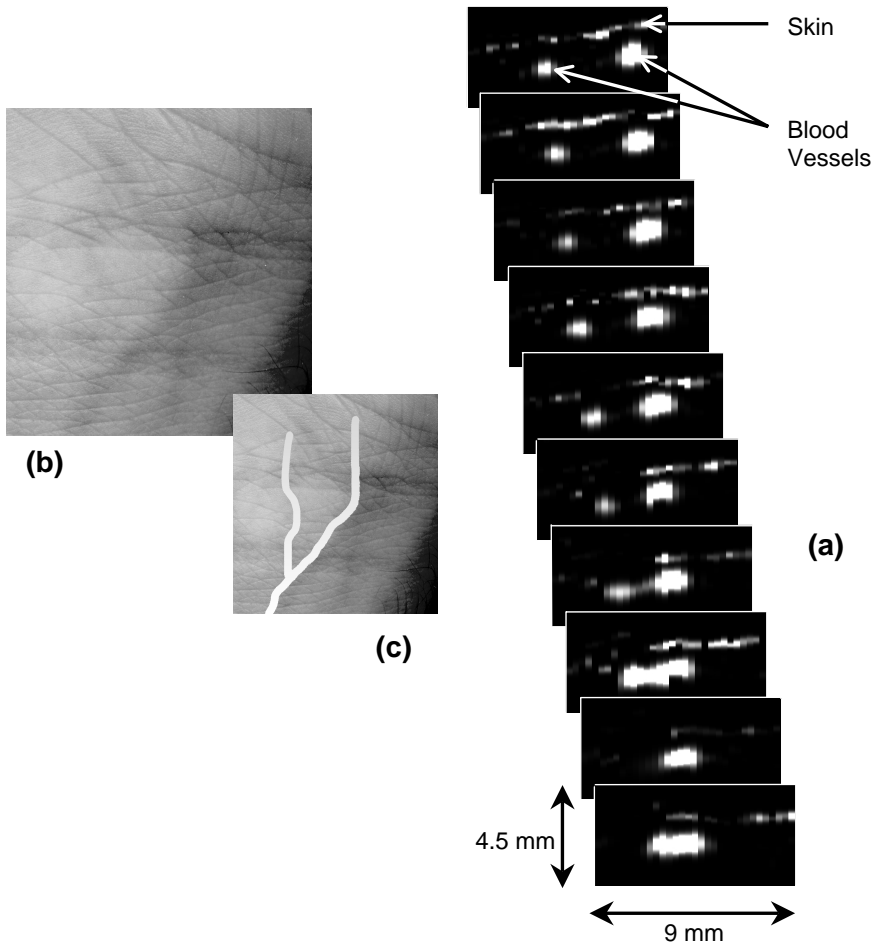
Figure 3.21 *Imaging of branching of vessels in the wrist of a human volunteer: (a) photoacoustic image, consisting of 10 slices, 1 mm apart. Horizontal axis: scan direction [mm]; vertical axis: depth [mm]. Each image consists of 61 measurement positions along a line, with a separation of 0.3 mm. At each measurement position, the photoacoustic signals are averaged 16 times. (b,c): photograph of measurement site; in (c) the course of the vessels is indicated with the white line.*

The cross section of the blood vessels shows on oval shape of the blood vessels. The smallest vessel (vessel on the left side in the photoacoustic image) has a size in depth of about 0.6 mm, and the larger vessel on the right side has a size in depth of 1 mm. The depth-position of the vessels with respect to the skin surface is about 1 mm.

3.5.3 Conclusions

We demonstrated *in vivo* 2D-photoacoustic imaging of blood vessels in man. The branching of blood vessels in reconstructed, showing the size of the vessels as well as the depth-position of the vessels with respect to the skin surface.

3.6 *Estimation of maximum measurement depth of photoacoustics*

To estimate the maximum depth in tissue, from which photoacoustic signals can be detected, the signal to noise ratio (SNR) as a function of depth has been analyzed. The signal to noise ratio is defined as the ratio of the maximum signal amplitude [mV] and the root-mean-square (rms) noise voltage [mV] of the photoacoustic signals.

The amplitude of the photoacoustic waves is proportional to the amount of absorbed energy, which depends on the absorption coefficient of the blood and the fluence rate. The fluence rate at a certain depth is dependent on the optical properties of the tissue. In case of a pencil beam, the fluence rate can be approximated by the diffusion approximation (see paragraph 3.2.2). Furthermore, the amplitude of detected signal depends on the depth response of the sensor (see paragraph 2.3.3 & 2.5). Using the diffusion approximation and the depth response of the sensor, the behavior of the amplitude of the photoacoustic signal as a function of depth can be calculated.

The signal to noise ratio has been determined for a 1 mm diameter silicone rubber tube filled with human blood, surrounded by a 7.5% Intralipid-10% dilution, as presented in Figure 3.13. There was no additional absorber added to the Intralipid solution, resulting in a reduced scattering coefficient of 0.75 mm^{-1} and an absorption of 0.002 mm^{-1} (equal to the absorption of water) at a wavelength of 800 nm. The photoacoustic signals were generated, illuminating the Intralipid solution with a 600 μm diameter fiber with pulses with an energy of 1 mJ/pulse. The time traces were averaged 16 times. In this case the rms noise voltage was about 10 mV. The measured signal to noise ratios (based on the results of Figure 3.13) were used to normalize the calculated amplitude of the photoacoustic waves, as a function of depth location of the source.

As the absorption coefficient of the Intralipid solution is too low, compared to real tissue, the values of signal to noise ratio have also been calculated for real tissue. This is done by re-calculating the values of the SNR for the Intralipid solution to a medium with different optical properties, using the diffusion approximation. The SNR-values based on the experiment in the Intralipid solution, have to be multiplied with a depth dependent factor, that describes the change in fluence-rate due to different optical properties. This factor also takes into account the change in absorption contrast ($\Delta\mu_{a,medium}=\mu_{a,medium}-\mu_{a,blood}$) between blood and the surrounding medium (tissue or Intralipid):

$$\frac{\psi_{tissue}}{\psi_{Intralipid}}(z) \cdot \frac{\Delta\mu_{a,tissue}}{\Delta\mu_{a,Intralipid}} = \frac{\Delta\mu_{a,tissue}}{\Delta\mu_{a,Intralipid}} \cdot \frac{\mu_{tr,tissue}}{\mu_{tr,Intralipid}} \cdot \frac{\exp(-\mu_{eff,tissue}z)}{\exp(-\mu_{eff,Intralipid}z)}$$

The optical properties used to calculate the fluence rate as a function of depth are listed in Table 3.2.

Table 3.2 *Optical properties of a 7.5% dilution of Intralipid-10% and real tissue, at a wavelength of 800nm, used to calculate the signal to noise-ratios in Figure 3.22. The optical properties of real tissue are based on the optical properties as listed in Table 3.1.*

Optical properties [mm^{-1}]	7.5% IL-10% $\lambda = 800$ nm	Real Tissue $\lambda = 800$ nm
μ_s'	0.75	0.75
μ_a	0.002	0.02
μ_{eff}	0.067	0.21
μ_{tr}	0.75	0.77
$\Delta\mu_{a, medium}$	0.40	0.38

Figure 3.22 shows the SNR as a function of depth for a 7.5% Intralipid-10% dilution and real tissue, for two different illumination geometries. The curves are shown for a pulse energy of 1 mJ/pulse in case a fiber is used to illuminate the medium. When a ring-shaped illumination system, as presented in paragraph 2.7, is used, more energy can be applied to the tissue, without exceeding the safety limits. In this calculation a pulse energy of 20 mJ/pulse is taken for the ring-shaped illumination system. The fluence rate of this illumination system, as a function of depth, is determined using Monte-Carlo simulations.[10]
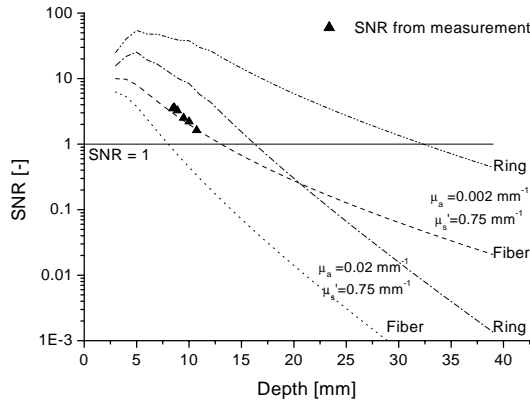
Figure 3.22 *Signal to noise ratio as a function of depth for a 1 mm diameter artificial blood vessel, filled with human blood. The photoacoustic signals were averaged 16 times. The SNR is shown for a 7.5% Intralipid-10% dilution, with no added absorber, and real tissue. Two different illumination geometries are presented: a fiber in the center of the photoacoustic sensor (1 mJ/pulse) and a ring-shaped illumination system (see chapter 2) around the sensor (20 mJ/pulse).*

It is obvious that the maximum detection distance is largest for the Intralipid dilution, without added absorber, as the absorption is very low. With increasing absorption (real tissue), the maximum detection distance decreases. Furthermore, the more energy per pulse is applied to the tissue, the larger the maximum detection distance will be, as is visualized in Figure 3.23.
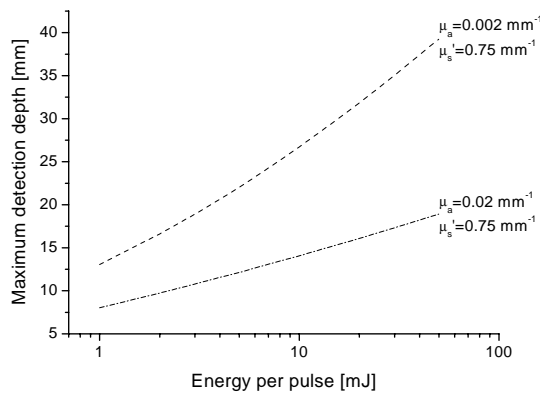
Figure 3.23 *Maximum depth at which a 1 mm diameter blood vessel can be detected as a function of energy per pulse. Data based on Figure 3.22, for two media surrounding the blood vessel, with different optical properties.*

However, safety limits inhibit an unlimited increasing of pulse energy. Enhancing the sensitivity of the photoacoustic sensor, or decreasing the noise level can further increase the maximum detection distance. By increasing the number of averages, the noise level can be reduced further. However, this also causes an increase in measurement time.

3.6.1 Conclusions

We conclude that when using the ring-shaped illumination geometry, with 20 mJ/pulse, in real tissue, a 1 mm diameter blood vessel can be detected up to a depth of about 16 mm. In this calculation, absorption of the tissue is assumed to be 0.02 mm^{-1}. If the actual absorption of the tissue is lower than this value, the maximum detection depth will increase.

3.7 References

1. K.P. Köstli, M. Frenz, H.P. Weber, G. Paltauf, and H. Schmidt-Kloiber, "Optoacoustic infrared spectroscopy of soft tissue", *J. Appl. Phys.*, vol. 88, pp. 1632-1637, 2000.
2. M.J. Crocker Ed., "Encyclopedia of Acoustics", J. Wiley & Sons, New York, 1997.
3. P.N.T. Wells, "Biomedical ultrasonics", Academic press, London, 1977.
4. V.M Ristic, "Principles of acoustic devices", J. Wiley & Sons, New York, 1983.
5. C.G.A. Hoelen, and F.F.M. de Mul, "A new theoretical approach to photoacoustic signal generation", *J. Acoust. Soc. Am.*, vol. 106 (2), pp. 695-706, 1999.
6. A. Ishimaru, "Diffusion of light in turbid material", *Applied Optics*, vol. 28, pp. 2210-2215, 1989.
7. T.J. Farell, and M.S. Patterson, "A diffusion theory model of spatially resolved, steady-state diffuse reflectance for the noninvasive determination of tissue optical properties in vivo", *Med. Phys.*, vol. 19, pp. 879-888, 1992.
8. M.S. Patterson, B.C. Wilson, and D.R. Wyman, "The propagation of optical radiation in tissue I. Models of radiation transport and their application", *Lasers in Medical Science*, vol. 6, pp. 155-168, 1991.
9. A.E. Profio, "Light transport in tissue", *Applied Optics*, vol. 28, pp. 2216-2222, 1989.
10. F.F.M. de Mul, M.H. Koelink, M.L. Kok, P.J. Harmsma, J. Greve, R. Graaff, and J.G. Aarnoudse, "Laser Doppler velocimetry and Monte Carlo simulations on models for blood perfusion in tissue", *Applied Optics*, vol. 34, pp. 6591-6611, 1995.

11. P. van der Zee, "Measurement and modeling of the optical properties of human tissue in the near infrared", *Ph.D. thesis*, University of London, London, 1993.

12. F. Bevilacqua, D. Piguet, P. Marquet, J.D. Gross, B.J. Tromberg, and C. Depeursinge, "In vivo local determination of tissue optical properties: applications to human brain", *Applied Optics*, vol. 38, pp. 4939-4950, 1999.

13. W.F. Cheong, S.A. Prahl, and A.J. Welch, "A Review of optical properties of biological tissues", *IEEE J. Quantum Electronics*, vol. 26, pp. 2166-2185, 1990.

14. C.R. Simpson, M. Kohl, M. Essenpreis, and M. Cope, "Near-infrared optical properties of ex vivo human skin and subcutaneous tissues measured using the Monte Carlo inversion technique", *Phys. Med. Biol.*, vol. 43, pp. 2465-2478, 1998.

15. G. Mitic, J. Kölzer, J. Otto, E. Plies, G. Sölkner, and W. Zinth, "Time-gated transillumination of biological tissues and tissuelike phantoms", *Applied Optics*, vol. 33, pp. 6699-6710, 1994.

16. J.F. Beek, P. Blokland, P. Posthumus, M. Aalders, J.W. Pickering, H.J.C.M. Sterenborg, and M.J.C. van Gemert, "In vitro double-integrating-sphere optical properties of tissues between 630 and 1064 nm", *Phys. Med. Biol.*, vol. 42, pp. 2255-2261, 1997.

17. V.G. Peters, D.R. Wyman, M.S. Patterson, and G.L. Frank, "Optical properties of normal and diseased human breast tissues in the visible and near infrared", *Phys. Med. Biol.*, vol. 35, pp. 1317-1334, 1990.

18. J.B. Fishkin, O. Coquoz, E.R. Anderson, M. Brenner, and B.J. Tromberg, "Frequency-domain photon migration measurements of normal and malignant tissue optical properties in a human subject", *Applied Optics*, vol. 36, pp. 10-20, 1997.

19. A. Roggan, D. Schädel, U. Netz, J.-P. Ritz, C.-T. Germer, and G. Müller, "The effect of preparation technique on the optical parameters of biological tissue", *Appl. Phys. B.*, vol. 69, pp. 445-453, 1999.

20. R. Graaff, A.C.M. Dassel, M.H. Koelink, F.F.M. de Mul, J.G. Aarnoudse, and W.G. Zijlstra, "Optical properties of human dermis in vitro and in vivo", *Applied Optics*, vol. 32, pp. 435-447, 1993.

21. S. Prahl, "Optical properties spectra", http://omlc.ogi.edu/spectra/index.html, Oregon Medical Laser Centre (OMLC).

22. S.L. Jacques, and M. Keijzer, "Dosimetry for lasers and light in dermatology: Monte Carlo simulations of 577-nm pulsed laser penetration into cutaneous vessels", in *Proc. Soc. Photo-Opt. Instrum.Eng.*, O.T. Tan Ed., vol. 1422, pp. 3-13, 1991.

23. R. Graaff, J.G. Aarnoudse, J.R. Zijp, P.M.A. Sloot, F.F.M. de Mul, J. Greve, and M. Koelink, "Reduced light-scattering properties for mixtures

of spherical particles: a simple approximation derived from Mie calculations", *Applied Optics*, vol. 31, pp. 1370-1376, 1992.

24. S.T. Flock, S.L. Jacques, B.C. Wilson, W.M. Star, and M.J.C. van Gemert, "Optical properties of Intralipid: A phantom medium for light propagation studies", *Las. Surg. Med.*, vol. 12, pp. 510-519, 1992.

25. H.J. van Staveren, C.J.M. Moes, J. van Marle, S.A. Prahl, and M.J.C. van Gemert, "Light scattering in Intralipid-10% in the wavelength range of 400-1100 nm", *Applied Optics*, vol. 30, pp. 4507-4514, 1991.

26. I. Driver, J.W. Feather, P.R. King, and J.B. Dawson, "The optical properties of aqueous suspensions of Intralipid, a fat emulsion", *Phys. Med. Biol.*, vol. 34, pp. 1927-1930, 1989.

27. J.A. Evans, "Physics – the nature of ultrasound", In *Practical Ultrasound*, R. Lerski (Ed.), pp. 15-29, IRL Press, Oxford, 1988.

28. M.L.J. Landsman, G. Kwant, G.A. Mook, and W.G. Zijlstra, "Light-absorbing properties, stability, and spectral stabilization of indocyanine green", *Journal of Applied Physiology*, vol. 40, pp. 575-583, 1976.

29. H.M. Lai, and K. Young, "Theory of the pulsed optoacoustic technique", *J.Acoust. Soc. Am.*, vol. 72, pp. 2000-2007, 1982.

30. M.W. Sigrist, and F.K. Kneubühl, "Laser generated stress waves in liquids", *J.Acoust. Soc. Am.*, vol. 64, pp. 1652-1663, 1978.

4 Pulsed-laser Doppler flowmetry

Using a pulsed-laser diode, a higher peak power can be injected into the tissue compared to a continuous wave laser-diode, without exceeding the safety limits. In this chapter we will prove that a pulsed-laser diode can be used in laser-Doppler flowmetry (LDF). The advantage of pulsed-LDF is that a larger spacing is allowed between the locations of illumination and detection. Thus, the penetration depth and therefore the measurement volume can be enlarged. In the second part of this chapter the effect of increasing fiber separation on the LDF measurements is investigated using Monte-Carlo light scattering simulations. Based on these measurements and simulations we will present a design for a more advanced pulsed-LDF set-up in the last part of this chapter.

4.1 Introduction

Laser Doppler Flowmetry (LDF) is used to probe the perfusion of the microcirculation in tissue with typical measurement depth of a few millimeters (paragraph 1.3). We would like to use LDF to monitor microcirculation in the brain. To reach the brain, light has to pass through the scalp and skull. This requires an enlargement of the typical penetration depth of LDF from a few millimeters to centimeters. Light detected at increasing distances from the source-fiber has traveled at larger depth in the tissue, as will be shown in paragraph 4.3.2. However, the intensity of the detected light will decrease with increasing source-detector distance. So the intensity of the source has to increase to obtain comparable signal levels.

The intensity to be applied to the tissue is restricted by safety regulations as ascertained by the standard NEN-EN 60825:1994. This standard gives values for the maximum permissible exposure (MPE) as a function of exposure time and pulse-duration. For continuous wave (CW) illumination the MPE is limited to 2 mW/mm^2 for exposure-times up to 10^4 sec. This MPE increases when pulsing the light source, as will be shown in paragraph 4.4. So a pulsed-laser diode is required to be able to measure at large source-detector separations.

The LDF signal detected by the photodetector is sampled by an analog-to-digital AD-card. Thus, illuminating the tissue outside the time frame that a photodetector signal is taken, is in principle a "waste of light" as it will not contribute to the signal, but only to the radiant exposure of the tissue. This implies that it is desirable to use a pulsed-laser diode in LDF.

4.2 Pulsed-LDF provides basis for deep perfusion probing[*]

A setup for pulsed-laser Doppler flowmetry (LDF) measurements has been built and tested. Measurements were carried out comparing continuous wave (CW) and pulsed-LDF. With pulsed-LDF a higher peak power can be injected into the tissue without exceeding the safety limits. This enables a much larger spacing between the locations of illumination and detection. Thus, the penetration depth and therefore the measurement volume can be enlarged using the pulsed-LDF method. This method will allow e.g. monitoring of the cerebral perfusion.

4.2.1 Introduction

Laser Doppler flowmetry (LDF) provides a method for non-invasive measurement of the perfusion of tissue. The tissue is illuminated with a CW laser source and the backscattered light from the tissue is then detected and analyzed. Due to scattering of the light at moving red blood cells, this light gets a frequency shift, which causes the detector signal to fluctuate due to interference. These fluctuations contain information about the perfusion. Bonner and Nossal[1] have shown that the first moment of the power spectral density of these signals is proportional to the root-mean-square velocities of the red blood cells:

$$\int_0^\infty \omega S(\omega)d\omega \sim \sqrt{<v^2>} \tag{4.1}$$

They also showed that the first moment is proportional to the concentration of moving red blood cells as well, provided this concentration is small.

Perfusion deep under the tissue surface can in principle be measured with laser Doppler flowmetry by placing the fibers for illumination and detection at a sufficient distance from each other. However, due to the strong attenuation of reflected light, laser powers would be needed which exceed the safety limits. Soelkner and co-workers[2,3], have shown that it is possible to perform laser Doppler measurements up to a depth of 30 mm with 120 mW CW light in a tissue-like head phantom. However, the high power needed prevented application on real tissue.

A way to increase the power without exceeding the safety limit is by pulsing the laser source and pulse-sampling the Doppler signal. By using short pulses, a high peak power can be achieved with a low average power. For long term monitoring of the perfusion the average power determines the maximum allowable power for skin illumination.

The developed pulsed-LDF method explicitly makes use of the high peak power by sampling the peak signals and thus enables non-invasive monitoring of deep perfusion. Other pulsed-[4] or modulated-[5] LDF methods do not make use of the higher peak power, but use the average power to determine the blood flow. Applications of the developed pulsed-LDF method include non-invasive measurement of the brain perfusion as well as monitoring of the perfusion *through* organs (e.g. kidney).

To test the proposed LDF method a test setup has been constructed using a pulsed laser diode.

4.2.2 **Method**

With tissue perfusion the typical frequency range of LDF is 0-20 kHz, corresponding with characteristic time scales up from 50 µs. These times are much larger than typical coherence times of the laser, which implies that each period of the Doppler signal will contain information from many coherence times. Then it does not matter whether those coherence times were directly adjacent to each other (as is the case with CW) or had intermittent time periods (as with pulsed-LDF). Following this line the pulsed-Laser-Doppler method has been designed.

The minimum pulse duration t_{pulse} is limited by the maximum pathlength difference Δl_{max}, which can occur in the measurement volume: photons traveling along the shortest pathlength should have the opportunity to interfere at the detector with photons traveling along the longest pathlength. The minimum pulse duration can be estimated by

$$t_{pulse} > \frac{\Delta l_{max}}{c/n} \tag{4.2}$$

with *n* the refractive index of tissue and *c* the speed of light in vacuum.

Assuming a maximum pathlength difference of 50 cm, which holds for nearly all practical cases, and $n = 1.33$ gives a minimum pulse duration of 2.2 ns. Furthermore, the coherence length of the laser has to be larger than the maximum pathlength difference to allow photons traveling along the shortest and longest pathlength to interfere at the detector: $l_{coh} > \Delta l_{max}$.

As laser-diodes are often used[6,7,8] as a light source in LDF instruments, for this pulsed-LDF method also a laser-diode has been used, which fulfills the mentioned criteria for the pulsed light source.
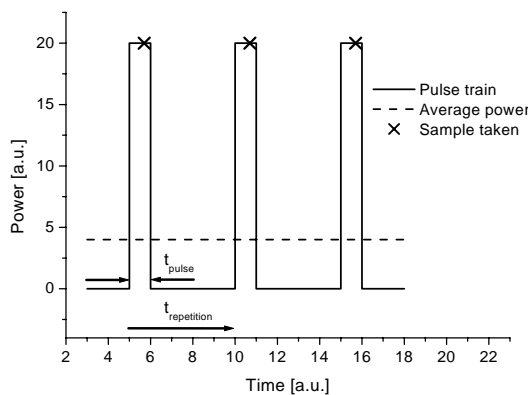

Figure 4.1 *Schematic representation of time scheme pulsed-LDF measurement.*

The LDF time signals are collected by sampling with an analog-to-digital AD-card. A sample is taken during the time the laser is "on". The laser is switched off for the time between two adjacent sample points (Figure 4.1). The average power P_{avg} during the LDF measurement is equal to the time ratio of the pulse width t_{pulse} and the repetition time $t_{repetition}$ times the peak pulse power P_{peak}:

$$P_{avg} = \frac{t_{pulse}}{t_{repetition}} P_{peak} \tag{4.3}$$

The basic setup is shown in Figure 4.2. A pulse generator (Hameg 8035) is used to modulate the laser diode driver (Thorlabs LDC 500) and provides the trigger for the AD-card (National Instruments AT-MIO-16XE-50). The light pulses of the single mode laser diode (Hitachi HL6501MG) are transmitted via a multimode optical fiber (step index, NA=0.23 and core diameter 400 μm) to the sample. The backscattered and Doppler-shifted light is transmitted through the same type of fiber to a photodiode (BPW 34). In this study the pulse generator delivers pulses of 16 μs with a repetition rate of 15 kHz. By using the laser pulse as a trigger for the AD-card, with a delay of 15 μs after the start of the laser pulse, a measurement is recorded only when the laser is 'on'. In this way it is simulated that the LDF signal is generated by a CW light source with a power equal to the peak pulse power.

Or, in other words: between two adjacent samples of the AD-card the light source is switched off. Using a sample-and-hold circuit the AD-card does not notice that the light source is switched off and measures a power equal to the peak pulse power.
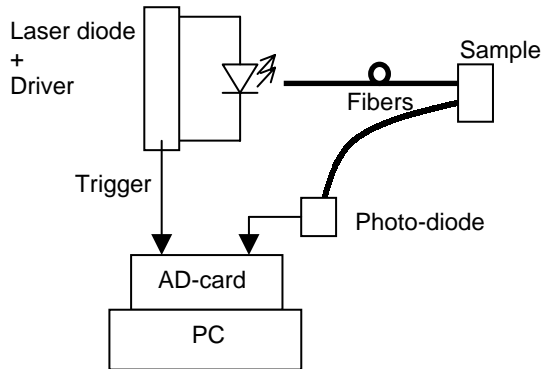
Figure 4.2 *The pulsed-LDF setup.*

A Labview program is used to collect the signals and to calculate the power spectrum of the detected signals. For each spectrum 1000 data-points are collected at a sample rate, determined by the pulse generator (15 kHz). To reduce the noise, several spectra can be averaged. As a sample an Intralipid[TM] (IL)

suspension is used (IL-10%). As the fat particles are in Brownian motion ("flow"), the photons will be Doppler-shifted. A white nylon block is used as a static ("no-flow") scattering object (no Doppler-shifted photons).

4.2.3 Results

Results of phantom measurements are presented in Figure 4.3 and Figure 4.4. Figure 4.3 gives the spectra measured with the pulsed-LDF method of a static scattering object (white Nylon block – "no flow") and a dynamic scattering object (cuvet with IL-10% - "flow", by Brownian motion). The nylon block has comparable scattering and absorption properties as the IL-10%. Also the spectrum of the background is shown. The spectrum of the IL-sample shows the expected Doppler-broadening, which is not present in the spectrum of the static scattering object.
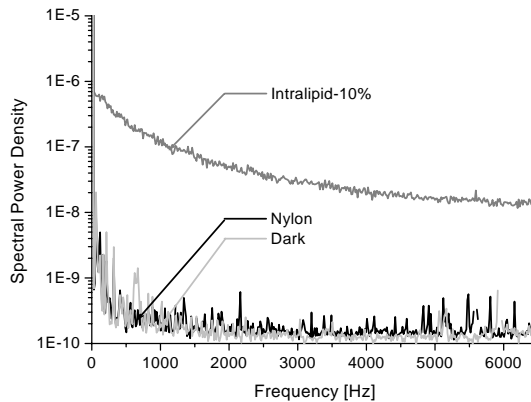
Figure 4.3 *Pulsed-LDF spectra Intralipid-10%, Nylon and dark.*

Comparison of pulsed- and CW-LDF has been carried out by comparing the phantom data results of pulsed-LDF with a peak pulse power of 20 mW to CW-LDF with a power equal to the peak pulse power and a power equal to the average pulsed power: 4.7 mW (Figure 4.4). The time ratio of repetition time and length of the pulses was 4.2.
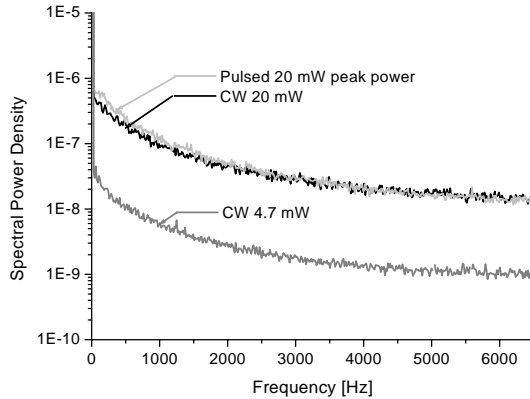
Figure 4.4 *LDF spectra Intralipid-10%, CW compared with pulsed-LDF.*

Figure 4.4 shows that the pulsed-LDF method gives a higher LDF signal than the CW method with the same average power. If the power of the CW LDF method is increased, with a factor equal to the time ratio (4.2), to the peak power of the pulsed-LDF method, both measurements result in the same signal levels.

An *in vivo* experiment on a thumb of a volunteer, using the pulsed-LDF method, with and without an occlusion has been performed. The spectra are recorded before, during and after the occlusion.
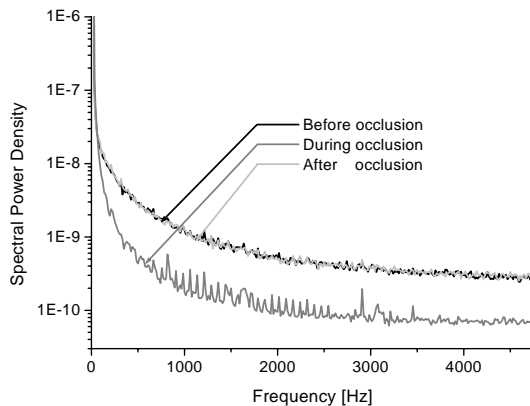
Figure 4.5 *In-vivo, pulsed-LDF spectra of thumb volunteer, before, during and after occlusion.*

Figure 4.5 shows that during the occlusion there are less high frequencies present in the spectrum. About 1 minute after the occlusion, the spectrum is about equal to the spectrum before occlusion.

4.2.4 **Discussion**

Figure 4.3 proves that the pulsed-LDF method indeed measures LDF signals. The LDF spectrum only shows the expected Doppler broadening when a measurement is carried out on a sample with "flow" (cuvet filled with IL-10%). This Doppler broadening is not present in the "no-flow" situation (nylon block).

Furthermore, it is obvious (Figure 4.4) that the proposed pulsed-LDF method makes use of the high peak power instead of the lower average power. Figure 4.4 shows that the pulsed-LDF method gives the same Doppler-signal levels in the spectrum as the CW LDF method with a power equal to the peak pulse power. This proves that the pulsed measurement offers the expected results, using the peak power of the pulses.

Standard CW laser Doppler instruments have a penetration depth up to a few millimeters. This is suitable for monitoring of the microcirculation. To obtain a larger penetration depth, the distance of the fibers must be increased, which is possible when the proposed pulsed-laser Doppler method is used.

Other published pulsed-[4] or modulated-[5] LDF methods do not use the high peak power, but use the average power to measure LDF signals. As the peak power can be much higher than the average power, the separation between the source and detector fiber can be increased, resulting in a larger sampling volume, containing information about deep perfusion.

The expected Doppler shifts in tissue cover a frequency range from 0-20 kHz. This implies that the repetition rate of the pulsed-laser Doppler instrument should be at least 40 kHz to avoid aliasing. If short pulses (~50 ns) together with this repetition rate are used, a peak power of 500 times the average power can be achieved.

Possible applications of the proposed pulsed-LDF method include the monitoring of cerebral perfusion as well as monitoring of perfusion through organs (e.g. kidney).

4.3 Monte-Carlo simulations

In the previous section we proved that a pulsed-laser diode can be used in LDF. This enables the use of larger pulse-peak powers without exceeding the safety regulations. This larger laser power can be used to increase the measurement volume by increasing the separation between the source and detection fiber.

The effect of the increased fiber separation on the detected intensity, measurement volume, and LDF parameters was simulated using Monte-Carlo light scattering simulations.[20]

4.3.1 Model

We simulated a semi-infinite homogenous medium with a reduced scattering coefficient of 0.75 mm^{-1} (g=0.63) and an optical absorption coefficient of 0.002 mm^{-1}, at a wavelength of 800 nm. In the simulations we could vary the percentage of moving particles. These moving particles were moving randomly in all directions, creating a Doppler-shifted photon as soon as a photon is scattered by these particles. The velocity of the particles was normally distributed with a standard deviation of 25% of the mean velocity. The backscattered photons were detected at the surface using a detector with a numerical aperture of 0.22.

4.3.2 Results

The average scattering depth of the photons, together with the average pathlength has been determined from these simulations (Figure 4.6-left panel). It is obvious that both average scattering depth and pathlength increase with increasing fiber separation. So at larger fiber separations more information about deeper tissue layers can be obtained.

Figure 4.6 *Monte-Carlo light scattering simulations; medium 7.5% Intralipid-10%: μ_s'=0.75 mm^{-1}; μ_a=0.002 mm^{-1}. Left panel: average scattering depth and average pathlength of photons arriving at the detector as a function of the separation between source and detection fiber. Right panel: detected intensity as a function of the separation between source and detection fiber; normalized on the source-intensity.*

The intensity as a function of the separation between source and detection fiber was determined from the simulation (Figure 4.6-right panel). This shows that the intensity is decreased by more than 4 orders in magnitude if the fiber separation is increased from 0.5 mm to 2.5 cm. So when increasing fiber separation to enlarge the measurement depth, the power of the light source has to be increased to get equal signal levels. This proves the need for a pulsed-LDF setup, as this enables an increase in peak-pulse power without exceeding safety-regulations.

The effect of increased fiber separation on the average Doppler-shift was simulated while all scatterers were moving. So all photons arriving at the detector will be Doppler-shifted. The average Doppler shift, as a function of fiber separation, is shown in Figure 4.7.
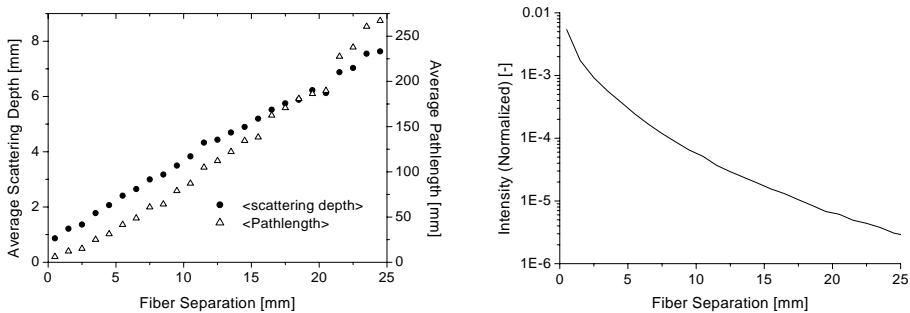

Figure 4.7 *Monte-Carlo light scattering simulation; medium: 7.5 % Intralipid-10%: $\mu_s'=0.75$ mm^{-1}; $\mu_a=0.002$ mm^{-1}, all scatterers were moving in random direction. The average Doppler shift has been determined as a function of fiber separation.*

When increasing the fiber separation, the photons will travel along a larger path, as shown in Figure 4.6-left panel. This implies that the average amount of scattering events per detected photon increases as well. So also the average Doppler shift will increase, which is shown in Figure 4.7.

Increasing fiber separation will also affect the fraction of Doppler-shifted photons reaching the detector. In our simulation we changed the percentage of moving scattering particles and determined the fraction of Doppler-shifted photons as a function of fiber separation. This is plotted in Figure 4.8.

It is obvious that increasing the distance between source and detection fiber gives an increase in fraction of Doppler-shifted photons. In Figure 4.6-left panel we showed that the pathlength increases, which implies an increase in number of scattering events. When the number of scattering events increases, also the probability that a photon is Doppler scattered increases. Furthermore it is clear that increasing the percentage of moving scatterers also increases the fraction of Doppler-shifted photons. The percentage of moving scatterers can be interpreted as the volume fraction of blood present in the microcirculation. In real tissue like brain, this is about 5%.[3]
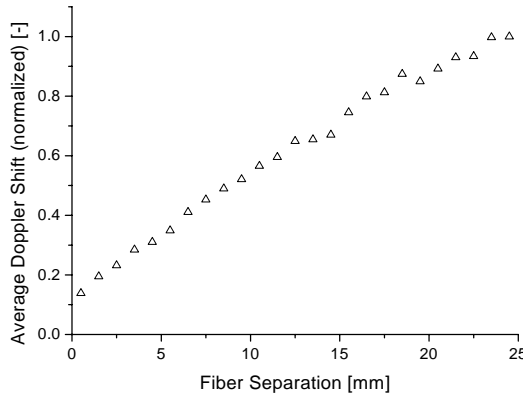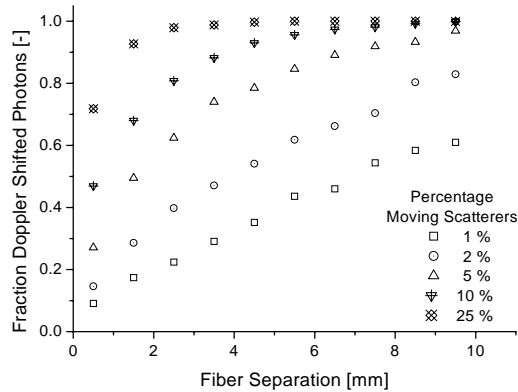
Figure 4.8 *Monte-Carlo light scattering simulation; medium: 7.5 % Intralipid-10%: $\mu_s'=0.75\ mm^{-1}$; $\mu_a=0.002\ mm^{-1}$, the percentage of moving scatterers is varied between 1% and 25%. The fraction of Doppler-shifted photons at the detector is shown as a function of fiber separation.*

As described in paragraph 1.3, the zero order moment is proportional to the red blood cell concentration. This is calculated as the integral over frequency of the power spectrum. Thus it determines the part of the power of the LDF signal that is caused by Doppler-shifted photons. If all photons are Doppler-shifted, the consequence for LDF is that no *additional* Doppler-shifted photons can be created due to increasing red blood cell concentration. As a result, no changes in concentration can be observed anymore.

In literature it is given that if the fraction of Doppler-shifted photons is larger than 0.4, the dependency of the zero order moment on concentration of red-blood cells becomes nonlinear.[7] This implies that for fractions of Doppler shifted photons larger than 0.4 care has to be taken in the interpretation of the zero-order moment.

Information about changes in average velocity will be maintained, despite that all photons are Doppler-shifted, as the average Doppler-shift still can be changed due to changes in red blood cell velocity.

4.3.3 Discussion

We showed that the measurement depth increases with increasing separation between source and detection fiber. Simultaneously the detected intensity decreases rapidly. This justifies the need for the pulsed-LDF method. This method allows a much higher peak-pulse power without exceeding the safety regulations.

Increasing fiber separation will result in an increase of the fraction of Doppler shifted photons. If the fraction of Doppler-shifted photons increases to values larger than about 0.4 the dependency of the zero order moment on the

concentration becomes nonlinear. Furthermore, at a certain fiber separation all photons will be Doppler-shifted and no changes in concentration of moving red blood cells will be detectable anymore. This is a severe limitation of the pulsed-LDF method. When interpreting measurements at large fiber-separation attention has to be paid to the zeroth moment signal.

Information about the concentration of red blood cells can nevertheless be obtained by analyzing the DC-intensity at the photodetector. In near-infrared spectroscopy (NIRS), this is used to determine changes in oxygenation as well as blood content, using multiple wavelengths.[11]

The magnitude of the weighted first order moment increases with increasing fiber-separation. The weighted first order moment will still provide information about the changes in average red-blood cell velocity, even if all detected photons are Doppler-shifted.

Enlarging the fiber separation causes an increase in average Doppler frequency. This is caused by an increased number of Doppler-scattering events. So the bandwidth of the system has to be chosen such that all Doppler frequencies fit within the detection bandwidth to avoid aliasing. In standard LDF instruments, with fiber separations up to a millimeter, the detection bandwidth is about 20-25 kHz. In the pulsed-LDF instrument this has to be increased, depending on the fiber separation.

4.4 Pulsed-LDF set-up – design considerations

In paragraph 4.2 we proved that a pulsed light source can be used in LDF measurements. In those experiments we used light pulses of 16 μs with a repetition rate of 15 kHz, resulting in a time ratio of repetition interval and length of the pulses of 4.2. The gain in instantaneous power was in this case only 4.2. However, this can be further optimized.

According to the standard NEN-EN 60825:1994 the maximum peak pulse power density $P_{peak,max}$ [W/m^2] in a wavelength range from 400-1400 nm is given by

$$P_{peak,\max} = \frac{2000}{f \cdot t_{pulse}} \qquad [\text{W/m}^2] \qquad\qquad (4.4)$$

with f the repetition rate [Hz], and t_{pulse} the pulse-duration [s]. This equation holds for illumination of tissue with 1 – 200 ns pulses, while continuously monitoring up to a period of 3 hours.

The amount of light reaching the photodetector will be proportional to the injected amount of light, which maximum (equation 4.4) is proportional to $1/t_{pulse}$. When one uses the maximum allowed peak pulse power, the detected signal will be inversely proportional to the pulse-duration as well. If we assume that the noise mainly consists of white noise, the total noise will be proportional to the

square root of the frequency bandwidth B of the detection system. This bandwidth is on its turn also dependent on the pulse duration and will be proportional to $1/t_{pulse}$. As a result, the dependency of the signal-to-noise ratio (SNR) on pulse duration can be calculated to be

$$SNR \sim \frac{1/t_{pulse}}{\sqrt{1/t_{pulse}}} = \sqrt{1/t_{pulse}} \ . \qquad (4.5)$$

This shows that shorter pulses will give a higher SNR. However, the pulse-duration is limited to about 2 ns (see paragraph 4.2.2), by the maximum expected path-length difference. So the optimum pulse duration in our case will be 2 ns. If we use a repetition rate of 100 kHz, then a peak pulse power density of 10 W/mm^2 is allowed.

As mentioned in section 4.2.2, LDF requires a coherence length of several tens of centimeters. A shorter coherence length will cause a decrease of modulation depth. For this reason a single-mode laser diode is essential. Single-mode laser diodes are currently available with a maximum pulse-peak power of about 150 mW (e.g. DL-8032-001, 150 mW, 830 nm, Sanyo). These laser diodes typically have emitting surfaces of several square micrometers. Due to this small area, the power-density is very high at this surface. The coating of the surface has to withstand the high power of the laser diode, which is currently the limiting factor in the production of high power single-mode laser diodes.

To generate nanosecond pulses, a pulsed laser-driver is needed. This driver should be able to deliver current-pulses with a high stability, i.e. as small as possible pulse-to-pulse variation in peak-current. The Doppler-shifted photons create a modulation of the photo-detector current. To be able to detect this modulation, the peak-to-peak fluctuation in output of the pulse-driver has to be much less than the modulation caused by the Doppler-shifted photons. Furthermore, the laser-mode of the laser-diode has to be identical in each peak of the successive pulses. If these modes in the peak of the pulses change from pulse to pulse, a change in speckle pattern on the photodetector will be observed, resulting in a modulation of the detector current. This will limit the sensitivity of the instrument, as this determines the minimum detectable Doppler modulation of the detector current.

The light from the laser diode has to be transported to the tissue, which can be done through an optical fiber. The area that is illuminated by the fiber determines the maximum power one can apply to the tissue. The backscattered and Doppler-shifted light will also be transmitted through an optical fiber, so that it can be detected by a photodetector.

The rise time and settling time of the detection electronics is a crucial factor using short (~ns) pulses. To sample the photodetector output, an analog -to-digital AD-card can be used. These cards have typically a settling time of a few microseconds for a full-scale step to ±1 least significant bit (e.g. NI PCI 6052-E, 333 kS/s, 16 bits, National instruments; settling time 3.5 μs). This implies that a sample-and-hold amplifier is needed to hold the voltage of the pulse for at least several microseconds, before it can be sampled by the AD-card.

This sample-and-hold amplifier will take one sample during the laser pulse. It will hold this value during a few microseconds. The AD-card then has time to settle to this value, before making an analog-to-digital conversion.

The sample frequency is determined by the pulse-repetition rate of the laser-driver. As mentioned in the previous paragraph, the bandwidth has to be larger than the 20-25kHz that is used in standard LDF instruments with a fiber separation up to a few millimeters. If we want to have a bandwidth of e.g. 50 kHz, the sampling frequency and thus the pulse-frequency should be at least 100 kHz to avoid aliasing (Nyquist criterion).
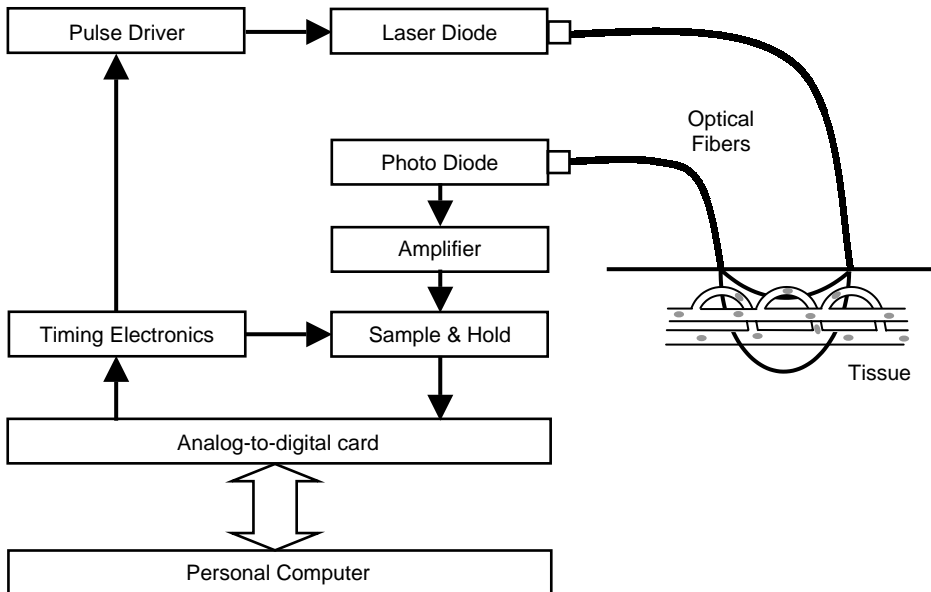

Figure 4.9 *Block diagram of the pulsed-LDF set-up.*

Signal processing can be carried out by a personal computer. The power spectrum *S(ω)* needs to be calculated from the digitally sampled LDF time traces. Information about red blood cell concentration, flow and average velocity can be

obtained from the zero order moment, first moment and weighted first moment of this power spectrum respectively (see also paragraph 1.3).

Figure 4.9 shows the block-diagram of the proposed design for a pulsed-LDF set-up.

4.5 Conclusion

We have shown that it is possible to use a pulsed-laser diode in LDF. The results obtained with pulsed-LDF were equal to the results obtained with a continuous-wave LDF. This proved that illumination outside the time frame that the photodetector signal is sampled, does not contribute to the signal. As the safety-regulations permit a much higher peak-power when using short pulses, it is advantageous to use a pulsed-laser diode instead of a continuous wave laser-diode. When higher powers are allowed, the fiber separation can be increased, resulting in a larger measurement depth.

We showed the consequences of increasing fiber separation for detected intensity, average scattering depth and average Doppler shift, using Monte-Carlo light scattering simulations. Increasing fiber separation reduces the detected intensity, justifying the need for a pulsed-LDF system. Furthermore, increasing fiber separation affects the detected average Doppler shift. This average Doppler frequency increases with increasing fiber separation. This implies that the bandwidth of the detection system should be sufficiently large to be able to detect these frequencies.

We showed that the fraction of Doppler-shifted photons increases rapidly to 100% when enlarging the fiber separation. This means that at large fiber separations no changes in zeroth moment (concentration) can be observed. When one is measuring at large fiber separations attention has to be paid to the interpretation of the zeroth moment.

Based on the results from the measurements and simulations we have proposed a pulsed-LDF instrument, using short (~ ns) laser pulses. This system should be able to handle large (up to a few cm) fiber separations, with the intention that information about deep perfusion can be obtained.

4.6 References

1. R.F. Bonner, and R. Nossal, "Model for laser Doppler measurements of blood flow in tissue", *Applied Optics*, vol. 20, pp. 2097-2107, 1981.
2. G. Soelkner, G. Mitic, and R. Lohwasser, "Monte Carlo simulations and laser Doppler flow measurements with high penetration depth in biological tissuelike head phantoms", *Applied Optics*, vol. 36, pp. 5647-5654, 1997.

3. R. Lohwasser, and G. Soelkner, "Experimental and Theoretical Laser-Doppler Frequency Spectra of a Tissuelike Model of a Human Head with Capillaries", *Applied Optics*, vol. 38, pp. 2128-2137, 1999.

4. V.G. Kolinko, F.F.M. de Mul, J. Greve, and A.V. Priezzhev, "Feasibility of picosecond laser-Doppler flowmetry provides basis for time-resolved Doppler tomography of biological tissues", *J. Biomed. Optics*, vol. 3, pp. 187-190, 1998.

5. H. Olkkonen, "Chopper stabilized laser-Doppler skin blood velocimeter", in *Laser Study of Macroscopic Biosystems*, J.E. Korppi-Tommola Ed., Proc. SPIE vol. 1922, pp. 219-224, 1992.

6. D. Dopheide, H. Pheifer, M. Faber, and G. Taux, "The Use of High-Frequency Pulsed Laser Diodes in Fringe Type Laser Doppler Anemometry", *J. Laser Appl.*, vol. 1, pp. 40-44, 1989.

7. H.W. Jentink, J.A.J. van Beurden, M.A. Helsdingen, F.F.M. de Mul, H.E. Suichies, J.G. Aarnoudse, and J. Greve, "A compact differential laser Doppler velocimeter using a semiconductor laser", *J. Phys. E.*, vol. 20, pp. 1281-1283, 1987.

8. F.F.M. de Mul, J. van Spijker, D. van der Plas, J. Greve, J.G. Aarnoudse, and T.M. Smits, "Mini laser-Doppler (blood) flow monitor with diode laser source and detection integrated in the probe", *Applied Optics*, vol. 23, pp. 2970-2973, 1984.

9. F.F.M. de Mul, M.H. Koelink, M.L. Kok, P.J. Harmsma, J. Greve, R. Graaff, and J.G. Aarnoudse, "Laser Doppler velocimetry and Monte Carlo simulations on models for blood perfusion in tissue", *Applied Optics*, vol. 34, pp. 6591-6611, 1995.

10. A. Serov, W. Steenbergen, F.F.M. de Mul, "Prediction of the photodetector signal generated by Doppler-induced speckle fluctuations: theory and some validations", *J. Opt. Soc. Am.*, vol. 18 (3), pp. 622-630, 2001.

11. M.C. van der Sluijs, W.N.J.M. Colier, R.J.F. Houston, and B. Oeseburg, "A new and hyighly sensitive continuous wave near infrared spectrophotometer with multiple detectors", in *Photon Propagation in Tissues III*, D.A. Benaron, B. Chance, M. Ferrari Eds., Proc. SPIE vol. 3194, pp. 63-72, 1997.

5 Monitoring changes in brain-perfusion using NIRS, LDF, and photoacoustics[*]

Experiments on the circulation in the brain of a piglet have been carried out to explore the combination of results obtained by near-infrared spectroscopy (NIRS), and laser Doppler flowmetry (LDF) or photoacoustics (PA). During these experiments the cerebral circulation has been distorted by inducing hypercapnia (i.e. increased arterial carbon dioxide tension), closing the carotid artery and flushing the brain with saline.

5.1 *Physiological background*

Blood reaches the brain through the vertebral arteries and the internal carotid arteries, supplying oxygen and nutrients to the brain cells. The exchange of gases, water and solutes with interstitial fluid takes place in the capillaries, with walls that consist of a single layer of endothelial cells. Capillaries cannot influence the flow because their walls do not contain smooth muscle cells. Capillaries are supplied by metarterioles or arterioles. At the point of connection of capillaries with metarterioles or arterioles there is a small cuff of smooth muscle called the pre-capillary sphincter. These arterioles, metarterioles and pre-capillary sphincters regulate the flow through capillaries.[1]

The cerebral circulation lies within a rigid structure, the cranium. Because these structures are incompressible, any increase in cerebral inflow must be associated with a comparable increase in venous outflow. The volume of blood and extravascular fluid is relatively constant; a change in either of these fluids must be accompanied by a reciprocal change in the other.[1]

Normally, cerebral blood flow (CBF) matches the cerebral metabolic rate. For example, when the brain is more active, it receives more blood flow. This phenomenon, known as autoregulation, is accomplished by vasodilatation and vasoconstriction. Smooth muscle fibers of metarterioles and pre-capillary sphincters react on reduced oxygen levels by relaxation, causing an increase in flow. Metabolic end products and factors (CO_2, H^+, K^+, adenosine) that tend to increase locally as a result of increased metabolism have similar effect.

The CBF is autoregulated between a mean-arterial-pressure of 60-160 mmHg. Below and above this range CBF is dependent upon the mean-arterial-pressure. Besides mean-arterial-pressure the CBF is dependent on arterial carbon dioxide tension ($PaCO_2$) and arterial oxygen tension (PaO_2). Hypercapnia, elevated $PaCO_2$, and hypoxia, low PaO_2 are cerebral vasodilators. Hypocapnia (low $PaCO_2$) induces vasoconstriction, reducing CBF. There appears to be a ceiling effect below which hypocapnia cannot reduce CBF. The theory is that at this level of hypocapnia, cerebral vasoconstriction approaches the ischemic (deficient blood supply) threshold and an ischemic vasodilatory effect counteracts the vasoconstrictor response. Carbon dioxide causes these changes in cerebral blood flow by altering the perivascular (and probably intracellular vascular smooth muscle) pH. Carbon dioxide can diffuse to the vascular smooth muscle from the lumen of the brain tissue or from the lumen of the vessels, whereas hydrogen ions in the blood are prevented from reaching the arteriolar smooth muscle by the blood-brain barrier. Hence, the cerebral vessels dilate when the hydrogen ion concentration is increased, but they dilate only minimally in response to an increase in the hydrogen ion concentration of the arterial blood.[1,2]

Autoregulation of cerebral blood flow is abolished by hypercapnia or any other potent vasodilator.[1] Increasing the CO_2 concentration in the inhalated air

will induce an increase of the $PaCO_2$ in the blood, which on its turn increases the CBF by increasing the perivascular pH. When the CO_2 concentration in the inhalated air is reduced to normal again the CBF will, after some time, return to the initial situation. Increasing ventilation frequency ("hyperventilation") can accelerate this process. If the increased ventilation frequency is maintained, the $PaCO_2$ will decrease too much, resulting in a hypocapnia.

In our experiments we will change the perfusion in the brain of a piglet by varying the amount of carbon dioxide in the inhalated air. The induced changes will be monitored using three different techniques: near-infrared spectroscopy (NIRS), laser-Doppler flowmetry (LDF) and photoacoustics (PA). These three techniques measure different parameters of the perfusion. NIRS gives information about *changes* in the *oxygenation* and *total hemoglobin concentration*. LDF measures *changes* in average red blood cell *velocity*, red blood cell *concentration* and *blood flow* of the microcirculation. PA measures *local* changes in vessel diameter, i.e. *amount of blood* present in blood vessels. The measurement volume of NIRS and LDF is large (typically $\sim cm^3$, depending on fiber separation), giving global information about changes in parameters. PA is able to measure locally, i.e. in a small volume ($\sim mm^3$). The NIRS system has already been used in the clinic. With these experiments we would like to determine if we could add additional information to the information obtained by the NIRS system using two additional techniques: PA and LDF.

5.2 Materials and Method

The measurements were carried out on the brain of a piglet. The Ethical Committee on Animal Research of the University of Nijmegen approved the experiments described in this work.

The piglet preparation was started with a light anesthesia (intra muscular Midazolam, 1.5 mg/kg; intra muscular Ketamine, 0.75-1 ml; and intra venous Atropine, 0.5 ml). After orotracheal intubation, the animal was mechanically ventilated with a mixture of oxygen, nitrous oxide, and 3% isoflurane (Aestiva/5; Datex-Ohmeda BV). A major vein of the left ear was cannulated for the administration of glucose 5% at a rate of 1.0 ml/kg/hour and of medication (Pavulon 0.15 mg/kg/hour). A polyvinyl catheter (diameter 2.1 mm) was placed in the left femoral artery for measuring the arterial blood pressure (disposable transducers, Baxter) and for arterial bloodgass sampling. Another catheter was placed in the left femoral vein for measuring the venous blood pressure.

In the left carotid artery a canula was placed, directed towards the head to be able to flush the brain with saline during the experiments. An ultrasound blood flow transducer (Transonic Systems Inc., Ithaca) has been placed around the right carotid artery to measure the carotid artery blood flow. The physiological data (ECG, rectal temperature, arterial and venous blood pressure, arterial oxygen

saturation (SaO$_2$), O$_2$-wave, CO$_2$-wave) were continuously recorded with a computer system and stored for further analysis (software package: MIDAC; Instrumentation Department, University Medical Center Nijmegen).

The NIRS measurements were performed using the Oxymon, a system developed by the Instrumentation Department of the University Medical Center Nijmegen, the Netherlands.[11] This system measures the attenuation of light at several near-infrared (NIR) wavelengths. From this attenuation the oxygenation changes in tissue are calculated.

Color Doppler ultrasound (P12-5 phased array transducer, ATL HDI 5000, Philips Medical systems) has been used to visualize the blood vessels, which were detected in the photoacoustic measurements.
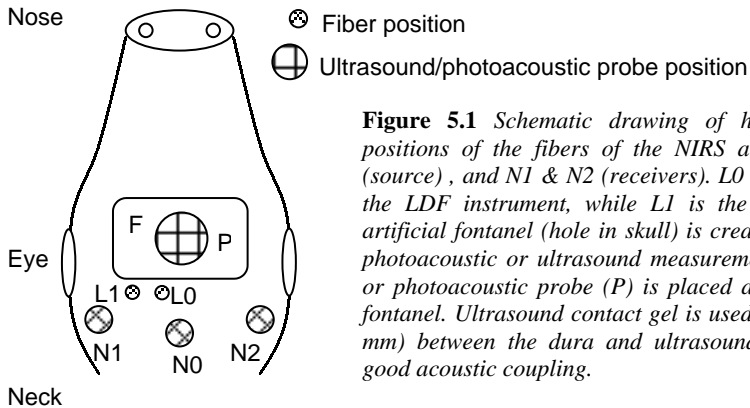

Figure 5.1 *Schematic drawing of head of piglet. The positions of the fibers of the NIRS are denoted with N0 (source) , and N1 & N2 (receivers). L0 is the source fiber of the LDF instrument, while L1 is the detection fiber. An artificial fontanel (hole in skull) is created at position F for photoacoustic or ultrasound measurements. The ultrasound or photoacoustic probe (P) is placed at the position of the fontanel. Ultrasound contact gel is used to fill the gap (~3-4 mm) between the dura and ultrasound sensor ensuring a good acoustic coupling.*

LDF and NIRS use fibers to deliver light to the tissue as well as fibers to detect the backscattered light. A schematic drawing of the positions of the fibers, ultrasound probe and photoacoustic sensor are shown in Figure 5.1.

The NIRS and LDF instruments were allowed to measure alternatingly during 1 second each, while the lasers of the other were switched off. This is done to avoid cross talk between both instruments. The LDF instrument acted as master during the instrument, generating an enable/disable square signal with a frequency of 0.5 Hz.

The LDF instrument used a continuous wave single mode laser-diode. The light of the laser-diode was coupled into an optical fiber (step index, NA=0.23 and core diameter 400 μm). Scattered light was probed using the same type of fiber. Light transmitted through this detection fiber was detected by a photodiode (HFD3022-002, Honeywell). The output of this photodiode was sampled during 0.96 sec with a frequency of 50 kHz. In this time we acquired 48000 samples. This time trace was then divided in 32 time traces of 1500 samples each. From all these 32 time traces the power spectra were calculated, which then were averaged. These power spectra ranged from 0-25 kHz, with a frequency-resolution of 33.3 Hz. This averaged spectrum was used to calculate

the moments of the spectrum providing us with information about the blood flow, red blood cell concentration, and average red blood cell velocity. The moments of the spectrum were calculated using a low cut-off frequency of 66.6 Hz. These moments were normalized on DC^2 of the intensity measured by the photodiode to correct for fluctuations in laser power.

The distance between source and detector fibers of the NIRS instrument was about 3-4 cm, resulting in a penetration depth of the light of about 2-3 cm. The fiber separation of the LDF fibers, the power, and the used laser-diodes are listed in Table 5.1. In experiment 2 we replaced the laser diode by a more powerful one. As the separation between the LDF fibers is much smaller than the NIRS fibers, the penetration depth is also much smaller. For the separation listed in Table 5.1 the penetration depth will be about 2-3 mm.

Table 5.1

	Experiment 1	*Experiment 2*
LDF fiber separation	4 mm	4.5 mm
Power out of source fiber	38 mW	110 mW
Laser diode	783 nm, single mode DL-8032-001, Sanyo	830 nm, single mode DL-7140-201K, Sanyo

We placed the LDF fibers directly on the dura to avoid influence of skin perfusion. Holes have been made in the skull, through which the fibers could be inserted. The fibers were glued to the skull to ensure that they stay at exactly the same position during the measurements. The NIRS fibers were placed on the skin, measuring through the skin as well as through the skull.

Since the bones of the skull absorb and reflect ultrasound, a hole in the skull (indicated with F in Figure 5.1) was needed to perform ultrasound or photoacoustic measurements. The dura was left intact when creating the hole in the skull. Bleedings occurring during removal of skin and skull were stopped by thermal-coagulation of these vessels.

During the photoacoustic measurements we used a Nd:YAG laser (Brilliant B, Quantel) together with an OPO (MagicPrism™, Opotek Inc.), delivering 8 ns pulses with a wavelength of 800 nm, and a repetition rate of 10 Hz to generate PA waves. These generated PA waves were detected by a home-built double-ring PA sensor, with a fiber for illumination integrated in the sensor. The power exiting the fiber inside the sensor was 1 mJ/pulse. A layer of Ultrasound contact gel (Sonogel®, Germany), with a thickness of about 3-4 mm, was placed between the photoacoustic sensor and the tissue to ensure a good acoustic coupling. The PA time traces were sampled (250 MS/s) and averaged by a digital oscilloscope (TDS210, Tektronix) and afterwards transferred to a computer.

5.3 Measurements: LDF + NIRS

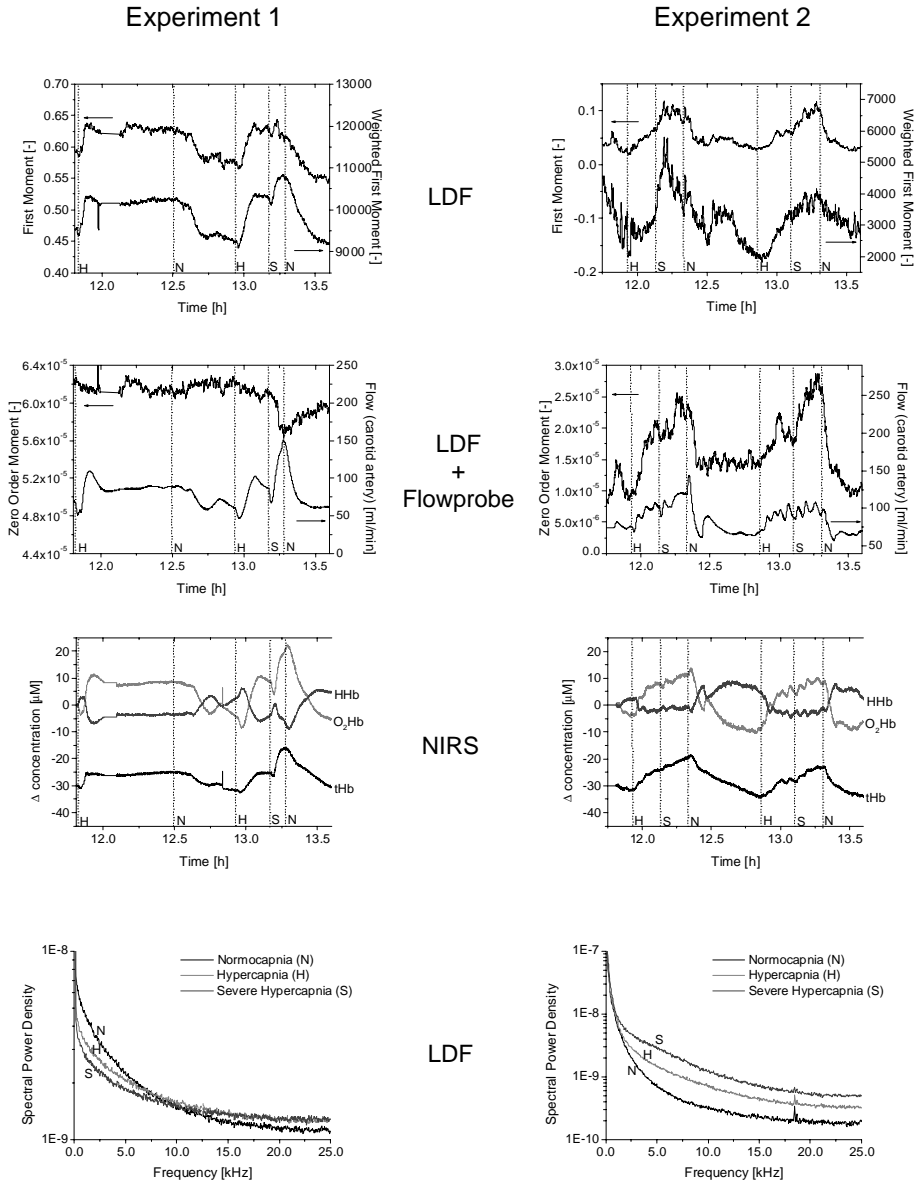## 5.3.1 Monitoring during normocapnia and hypercapnia

Experiment 1   Experiment 2

Figure 5.2 *Caption: see next page.*

Figure 5.2 *Results of NIRS and LDF measurements, while monitoring changes in cerebral perfusion. Respectively H, S, and N indicate the starting of a Hypercapnia, Severe hypercapnia and the return to Normocapnia. Left panel: results of experiment 1; right panel: results of experiment 2 (see also Table 5.1). LDF gives the zero order moment, first moment and weighted first moment, that are assumed to be proportional to red blood cell concentration, flow and average red blood cell velocity respectively. The flow [ml/min] in the carotid artery is measured using an ultrasound flow probe. Changes in oxy-hemoglobin (O_2Hb), de-oxy-hemoglobin (HHb) and total hemoglobin (tHb) concentration [μM] are determined using NIRS; the tHb-curve is shifted over 30 μM for clarity. The LDF spectra shown in the lower graphs are taken during a period of normocapnia (exp.1: t=12.90h, exp.2: t=12.79h) hypercapnia (exp.1: t=13.07h, exp.2: t=13.03h) and severe hypercapnia (exp.1: t=13.24h, exp.2: t=13.20h). These spectra are a result of averaging over 3 minutes.*

During the experiments we changed the carbon dioxide concentration in the blood in two steps, from normocapnia to hypercapnia and severe hypercapnia respectively, by changing the CO_2 supply in the ventilator. These conditions were maintained during at least 10 minutes in order to reach a stable condition. After the severe hypercapnia, the starting condition was restored. By increasing the ventilation frequency we accelerated this return to normocapnic situation.

In Figure 5.2 the results of the measurements with LDF and NIRS are shown. Respectively H, S, and N indicate the *starting* of a Hypercapnia, Severe hypercapnia and the return to Normocapnia.

Experiment 1 shows that the weighted first moment, i.e. average red blood cell velocity, correlates very well with the flow measured in the carotid artery. The flow measured with the LDF increases during hypercapnia, which is in agreement with the measured carotid flow. The concentration shows no changes, except during the severe hypercapnia where a decrease in concentration could be observed. However, the NIRS data displays an increase in blood content during hypercapnia.

Experiment 2 shows that increasing concentration and velocity both contribute to an increase in flow during hypercapnia. This is in agreement with the NIRS data as well as the flow probe data, which showed an increase in respectively total hemoglobin content (tHb) and carotid flow.

Experiment 1 shows a concentration that is about a factor of 3 larger compared to experiment 2. So it is likely that in experiment 1 all photons reaching the detector are already Doppler shifted. So changes in red blood cell concentration do not create *additional* Doppler shifted photons. Thus, no changes in concentration (zero order moment) will be observed. The power spectra (Figure 5.2 – left panel, lower graph) show changes in the shape of the spectra whereas the area under the spectrum does not change significantly when changing the cerebral perfusion. The power spectra measured during experiment 2 display a clear change in area under the spectra. This reflects a change in concentration, which is proportional to the zero order moment of the power spectrum.

5.3.2 Monitoring during occlusion and flushing with saline

In the following experiments we induced changes in the cerebral perfusion by closing the right carotid artery for a short time (occlusion). The left carotid artery was completely blocked by a canula, which was inserted into this artery. This canula is used to perfuse the brain with saline during an occlusion of the right carotid artery, replacing the blood in the brain for some time.

By closing and blocking both carotid arteries, the blood supply to the brain was stopped. This causes a decrease in blood flow in the brain. When flushing the brain with saline, most blood is replaced by saline. As saline does not scatter light, a reduction of flow and concentration is expected. The results obtained during these experiments are shown in Figure 5.3. The set-up was identical to the set-up used in experiment 1, as described in 5.2 and 5.3.1.
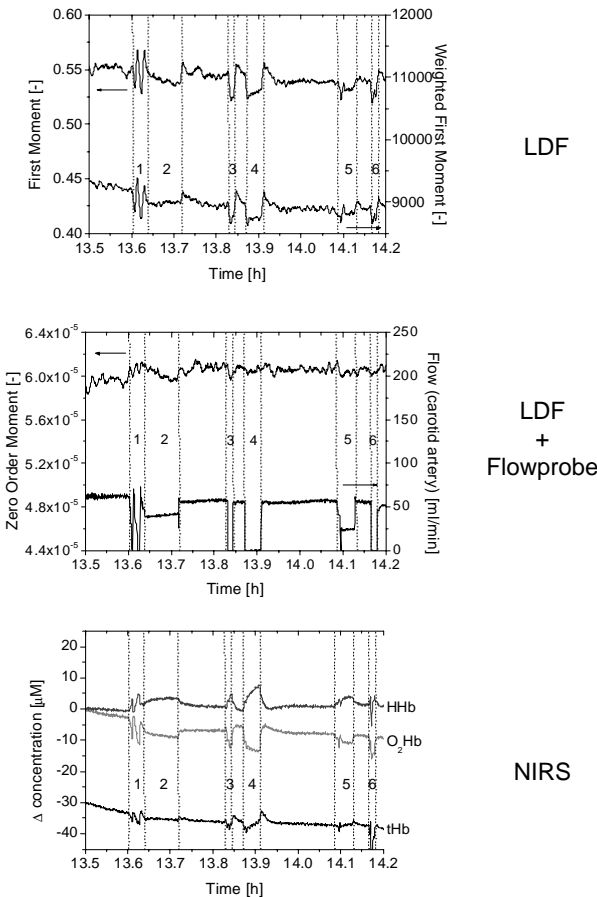
Figure 5.3 *LDF and NIRS data (the tHb-curve is shifted over 30 μM for clarity) during occlusion of the carotid artery together with the flow in the carotid artery, measured with an ultrasound flowprobe. LDF gives the zero order moment, first moment and weighted first moment, indicating red blood cell concentration, flow and average red blood cell velocity respectively. The numbers in the graphs mark the time during which the flow in the carotid artery has been decreased.*

1. *Repeatedly opening and closing of the right carotid artery.*

2. *Right carotid artery 50 % closed.*

3. *Right carotid artery completely closed.*

4. *Right carotid artery completely closed.*

5. *Right carotid artery 50 % closed + injection of saline in left carotid artery*

6. *Right carotid artery completely closed + injection of saline in left carotid artery.*

These graphs show that during occlusion the flow (first moment) and velocity (weighted first moment) decrease. The flow measured with the transonic flowprobe around the carotid artery correlates well with the velocity and flow as measured with LDF. The velocity and flow measured with LDF do not drop to "zero". In our calculation of the moments of the spectra we did not correct for the residual spectrum, which is present in case no Doppler photons are detected. This residual spectrum is mainly caused by system-noise due to noise in electronics, and it creates an offset in the LDF-signals.

NIRS displays changes in total hemoglobin concentration. These changes are not measured by the LDF instruments, as in our measurement probably all photons are already Doppler shifted (see 5.3.1, experiment 1).

When flushing the brain with saline, a decrease in concentration is expected as a non-scattering fluid replaces red blood cells. So no Doppler shifted photons can be created, causing a decrease of the concentration. However, we did not observe a decrease in concentration in our LDF measurements. NIRS observes a short decrease in total hemoglobin concentration during a short time when the right carotid artery is completely closed (Figure 5.3 – event 6). Probably the red blood cells in the microcirculation are not completely replaced by saline, which makes LDF still detecting Doppler shifted photons. NIRS measures also the influence of larger vessels. Replacing blood in these large vessels by saline will have an enormous effect on the measured attenuation of light. LDF mainly measures the perfusion of the microcirculation and large vessels do not contribute to the LDF signals. This can explain the difference in the results between the LDF and NIRS measurements.

5.3.3 Conclusions

We have shown to be able to detect changes in flow using LDF when changing the cerebral perfusion. Our measurements correlate well with the flow measured in the carotid artery, which was the main supply of blood to the brain in our experiment. NIRS measures changes in hemoglobin content in the brain, but does not provide information about the flow. LDF can be used to add this information to the NIRS measurement.

We also showed that changes in cerebral perfusion, induced by partly or completely closing the carotid artery, could be observed with LDF. In these cases NIRS showed a slight decrease in total hemoglobin concentration whereas the changes in oxygenation were large. As the brain does not get a supply of blood, the oxygenation of the blood still present in the brain decreases rapidly.

LDF is able to measure changes in concentration of red blood cells, but only in those cases where not all photons arriving at the detector are Doppler shifted. When increasing the distance between the source- and detector-fiber, the fraction of Doppler shifted photons increases. Thus, at a certain distance all

photons will be Doppler shifted and no changes in concentration can be observed anymore.

These experiments show that LDF can add additional information to the NIRS measurements. Whereas NIRS is able to measure changes in total hemoglobin concentration and oxygenation, LDF can add information about the flow to this information. As soon as the sensitivity of LDF is improved, the fiber separation can be increased so that they can be combined with the NIRS fibers, resulting in an identical measurement volume. In this way information can be obtained about oxygenation, blood content as well as blood flow in the brain in a non-invasive way.

5.4 Measurements: NIRS + PA

5.4.1 Imaging

A vessel in the upper part of the brain has been localized using photoacoustics. We made a linear scan, consisting of 31 measurements with a spacing of 100 μm. The photoacoustic time traces were averaged 128 times per measurement position. The corresponding image is shown in Figure 5.4-right panel. This image shows the cross section of a blood vessel, with a diameter of about 0.9 mm, at a depth of 1.8 mm below the dura. On the left side of the vessel also a small second vessel is visible.
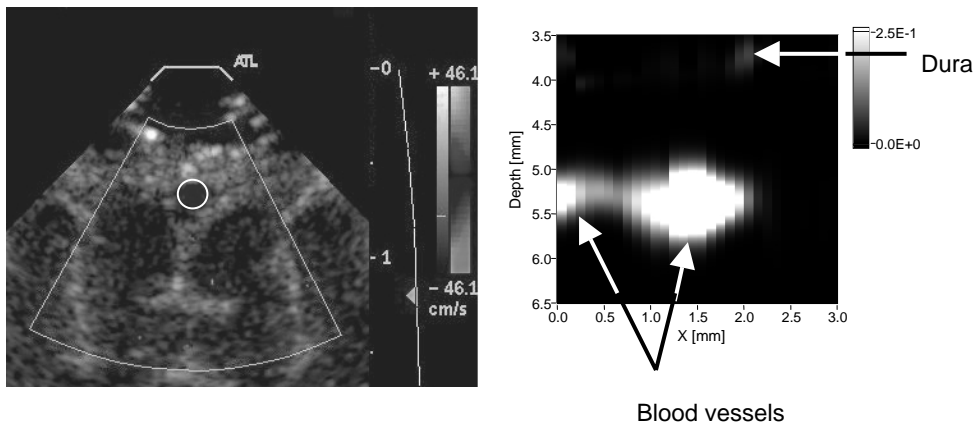
Figure 5.4 *Left panel: color Doppler ultrasound image, showing the blood vessel. The position of the blood vessel is indicated with a circle for clarity. Right panel: photoacoustic reconstruction of a blood vessel in the brain, at a depth of about 1.8 mm below the dura. The gap (about 3.7 mm) between the dura and the photoacoustic sensor was filled with ultrasound contact gel to ensure good acoustic coupling. The position depth=0 mm in the image corresponds with the position of the sensor-surface.*

Figure 5.4-left panel shows a color Doppler ultrasound image, visualizing also the cross section of the blood vessel. To be able to measure at about the same position on the brain, the photoacoustic sensor had to be removed, which makes it difficult for both methods to measure *exactly* at the same position.

The color Doppler ultrasound image gives a diameter of the vessel of about 1.0 mm, with a depth with respect to the dura of 2.5 mm. These values are about the same order of magnitude as determined with photoacoustics. Repositioning of the probes as mentioned above causes the main deviation in these values.

5.4.2 Monitoring during normocapnia and hypercapnia

After imaging the blood vessel with photoacoustics, we placed the sensor exactly above this vessel, at position X=1.5 mm (see Figure 5.4). At this position changes in vessel size (i.e. blood content) were monitored while changing the cerebral perfusion. Changes in cerebral perfusion were induced like in the LDF experiment as described in paragraph 5.3.1.

The results of the experiments with NIRS and PA are shown in Figure 5.5. The zero-crossing time of the PA signal (time between compression and rarefaction peak, where the signal crosses "zero") indicates the position of the blood vessel. This zero-crossing time decreases about 100 ns when a hypercapnia is induced, indicating a movement of the blood vessel towards the sensor of about 150 μm, using a sound velocity of 1500 m/s. This movement is most likely to be caused by a filling of the brain with blood. During hypercapnia the total hemoglobin concentration, as measured with NIRS, increases (Figure 5.5-right panel). As the bone of the skull was partly removed, the brain was able to increase its volume, whereas in normal situation it is embedded in a rigid structure. So this filling of the brain with blood will normally not be measured. The movement of the vessel upward (t_0) correlates with the total hemoglobin concentration as measured with NIRS (Figure 5.5-right panel) until the moment where the mechanical ventilation frequency is increased. This was done to return the animal faster to a normocapnic situation.

Due to inspiration and expiration the volume of air inside the lungs changes, causing small movement artifacts of the animal during the measurements. A sudden increase in mechanical ventilation frequency changes the frequency of the movements as well. Due to this changed movement frequency, it is very likely that the position of the head of the animal changes slightly. This can be seen from Figure 5.5-left panel, where both t_0 and τ_{pp} show an instant step at this moment (indicated with the dotted line: event 4).
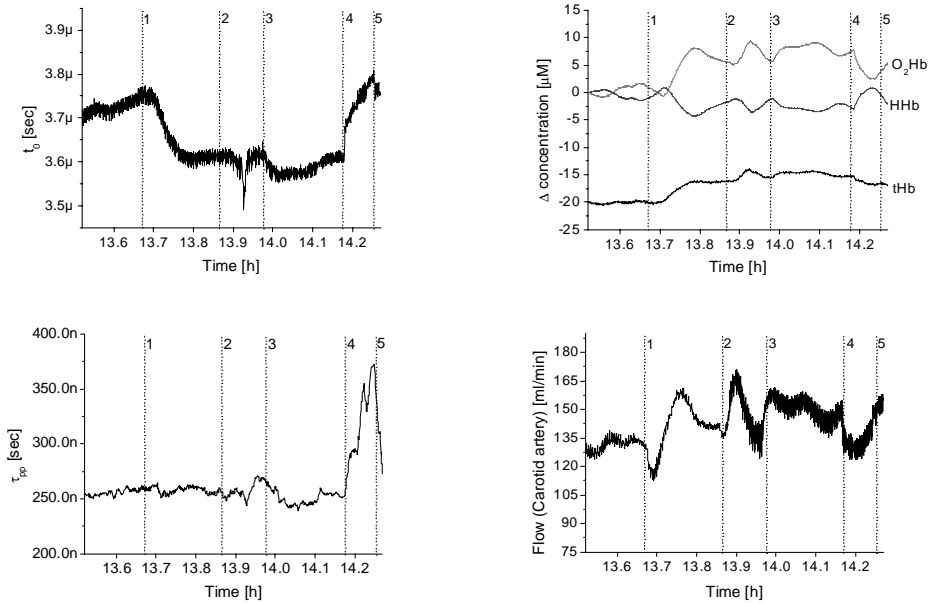
1. Hypercapnia
2. Severe hypercapnia
3. Normocapnia
4. Increasing ventilation frequency
5. Decreasing ventilation frequency

Figure 5.5 *Results of PA and LDF measurements, while monitoring changes in cerebral perfusion. Left panel: peak-to-peak time (τ_{pp} – indicating vessel size) and the zero crossing time (t_0 – indicating position of the vessel) of the photoacoustic signals. Right panel: results of the NIRS measurements - changes in oxy-hemoglobin (O_2Hb), de-oxy-hemoglobin (HHb) and total hemoglobin (tHb) concentration [μM]; the tHb-curve is shifted over 20 μM for clarity. The flow (carotid artery) is also determined during the experiment.*

The peak-to-peak time of the photoacoustic signal is a measure for the diameter of the blood vessel. So when the diameter of the vessel increases (vasodilatation) an increase in peak-to-peak time is expected. The peak-to-peak time does not show significant changes due to hypercapnia, correlating with increasing blood content as measured with NIRS. At a time of 13.93h the peak-to-peak time shows an increase, indicating an increase in vessel size. At this time also the NIRS exhibits an increase in total hemoglobin concentration. This increase is the result of the induced severe hypercapnia. It is striking that this increase is much smaller than the increase in hemoglobin concentration when inducing hypercapnia, which is not visible in the peak-to-peak time. An explanation can be that this vessel does not reflect the behavior of the total brain.

When inducing hypercapnia there is probably not yet a need for this vessel to dilate, whereas severe hypercapnia causes dilatation of this vessel.

5.4.3 Balloon catheter

A single lumen balloon catheter (catheter diameter: 1.3 mm, balloon diameter 6.5 mm, Berman Angiographic Balloon catheter, Arrow International) filled with an optically high-absorbing fluid   (mixture of the dye ICG - Indocyanine green together with graphite; $\mu_a \gg \mu_{a,blood}$) has been used to verify if PA is able to detect signals from relatively large depth positions inside the brain. This balloon catheter was inserted into the brain from aside, through a hole that was drilled in the skull, at a position just above the eye of the piglet.

Changing the volume of fluid inside the balloon changed the dimensions of this balloon catheter. Increasing the amount of fluid created an expansion of the balloon. The almost spherical shape of the balloon was maintained during expansion as well as during contraction of the balloon.

The brain is covered by the dura, a tough membrane. So increasing the size of the balloon compresses the brain tissue. Thus, the surface of the balloon is expected to come closer to the dura while expanding.
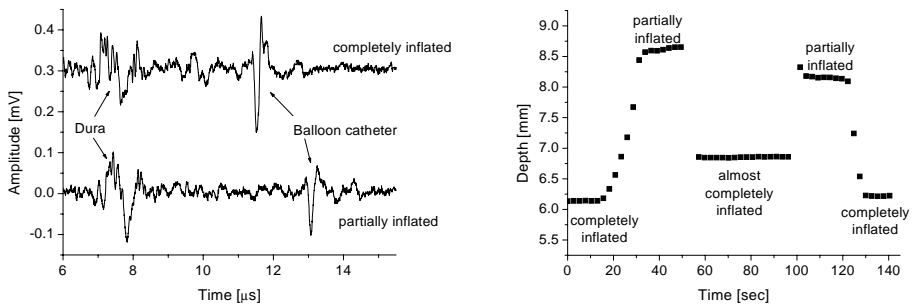
Figure 5.6 *Left panel: Photoacoustic time traces of a balloon catheter filled with an optical absorber, positioned inside the brain. Upper trace: balloon completely inflated; lower trace balloon 50% filled. Right panel: depth position of the signal of the balloon catheter with respect to the dura, while changing the volume of the balloon as a function of time.*

Figure 5.6-left panel shows the photoacoustic time traces when the balloon is partially and completely inflated. The position of the balloon will be closer to the dura in case it is completely inflated, compared with the situation where it is partially inflated. The time traces show that the delay between the signal from the dura and balloon is smaller when the balloon is completely inflated compared to the partially inflated balloon. Multiplying this time delay with the velocity of sound, the depth position of the balloon with respect to the dura can be obtained. This depth is plotted in Figure 5.6-right panel, which shows the depth position of the balloon as a function of time while the volume of the

balloon is being changed. This experiment proves that an optically high-absorbing structure can be detected in real brain at a depth of more than 8 mm, using 800 nm light.

5.4.4 Conclusions

We have shown to be able to image a blood vessel in the upper part of the brain. The diameter and position of the vessel were in agreement with the Doppler ultrasound measurement. Repositioning of the probes caused slight deviations in estimated diameter and depth position, as it was not possible to measure with PA and Doppler ultrasound at the same position at the same time.

Furthermore we have shown that we could detect changes in the position of a blood vessel due to filling the brain with blood. However, this will not be possible in a real situation where the brain is embedded in a rigid structure. In our experiments we had to make a hole in the skull, which enabled the brain to move up and down freely. The peak-to-peak time did not change significantly when inducing hypercapnia, whereas the NIRS showed a distinct increase in total hemoglobin concentration. Inducing severe hypercapnia resulted in a smaller change of total hemoglobin concentration compared to hypercapnia. However, this caused a significant increase in peak-to-peak time, indicating dilatation of the vessel (i.e. increasing diameter of the vessel).

Using a balloon catheter filled with a highly absorbing fluid ($\mu_a >> \mu_{a,blood}$) we demonstrated that we are able to detect absorbing structures in real brain up to a depth of at least 8 mm. Blood vessels at this depth will give a much lower signal amplitude than this highly absorbing medium. So to be able to detect blood vessels at this depth, the amount of energy applied to the tissue has to be increased. In this experiment we used not more than 1 mJ/pulse, which can be increased significantly. When increasing the amount of energy per pulse, also the illumination area has to be increased, not to exceed the safety limits.

5.5 References

1. R.M. Berne, and M.N. Levy, "Physiology", Mosby Inc., St. Louis, 1998.
2. R.C. Little, W.C. Little, "Physiology of heart and circulation", Year Book Medical Publishers Inc., Chicago, 1989.
3. M.C. van der Sluijs, W.N.J.M. Colier, R.J.F. Houston, and B. Oeseburg, "A new and hyighly sensitive continuous wave near infrared spectrophotometer with multiple detectors", in *Photon Propagation in Tissues III*, D.A. Benaron, B. Chance, M. Ferrari Eds., Proc. SPIE vol. 3194, pp. 63-72, 1997.

6 Combined NIRS, LDF and PA instrument

The experiments described in the previous chapter have been carried out using the separate instruments with their own probes. When we would like to combine NIRS, LDF, and PA, a combined probe is preferable. In this chapter the complementarity of the methods is described, followed by an outline of a prototype of a combined probe.

6.1 Complementarity of the methods

In this paragraph the complementarity of NIRS, LDF and PA will be described, comparing the measured parameters, measurement volumes, and similarity of detection methods.

Measurement volume

The measurement volume of NIRS is determined by the fiber separation. The volume that is probed can be approached by a banana-shape (Figure 6.1). This banana contains the paths along which the photons have travelled before they reach the detection fiber. Changes in absorption (due to changes in oxygenation and total hemoglobin content) inside this volume will contribute to the NIRS measurement.

In LDF also fibers are used for the detection of changes in perfusion. If we assume that the tissue is homogeneously perfused, the measurement volume will have a shape identical to the measurement volume of NIRS. If the tissue is not homogeneously perfused, then the regions with high perfusion will predominantly contribute to the LDF signal.

The measurement volume of PA is determined by the opening angle of the sensor (Figure 6.1). We have designed a sensor with a very small opening angle (few degrees). This means that PA will only detect changes in vessel diameter (i.e. blood content) in a narrow cone. When one uses several of these PA-sensors next to each other (linear array), an image of blood content can be obtained. The lateral and depth sensitivity will be very high (~mm) when using PA. In case LDF or NIRS is used, the depth at which the instrument measures will be dependent on the fiber separation. In lateral direction a large region will be probed (Figure 6.1).
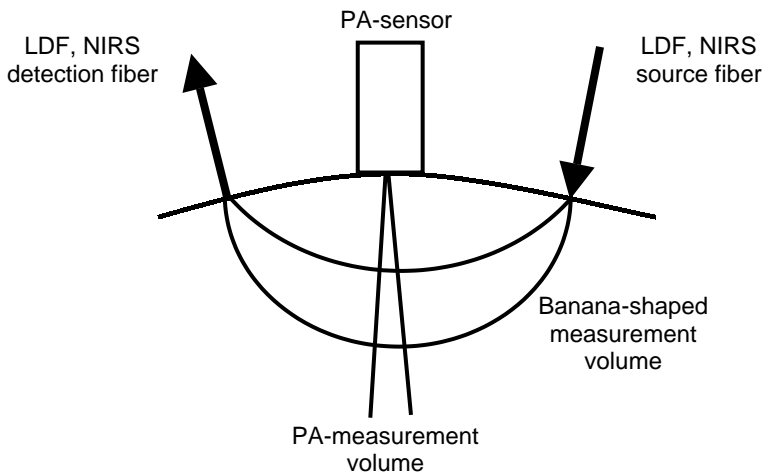

Figure 6.1 *Schematic overview of the measurement volumes of NIRS, LDF and PA.*

Perfusion/flow

Using LDF one is able to detect changes in perfusion of the microcirculatory network. The contribution of flow inside large vessels is dependent on the penetration depth ($1/\mu_{a,blood}$) of the light into these vessels. At a wavelength of 800 nm, this penetration depth is about 1-2 mm. The light has to enter the vessel as well as to exit the vessel to be detected. So the contribution of flow *inside* vessels with a diameter larger than about 1 mm will be small. From these vessels only the outer layer of moving red blood cells will contribute to the LDF measurement.

Blood content

All three instruments are able to measure changes in blood content. Using NIRS changes in absorption due to changes in overall blood content can be measured. In LDF one is able to measure changes in concentration of moving red blood cells (RBCs). As mentioned above, mainly the microcirculation contributes to the LDF measurement. When increasing the LDF-fiber separation, there will be a position at which no changes in RBC concentration will be detected anymore. At this fiber separation all photons arriving at the detection fiber are already Doppler shifted. Thus, changes in RBC concentration will create no additional Doppler shifted photons and no changes in RBC concentration will be detectable any more (chapter 4).

Using PA one is able to detect changes in vessel diameter (i.e. blood content) on a line in depth. Furthermore, bleedings can be detected by PA when these occur inside the measurement volume.

Oxygenation

Changes in oxygenation can be measured using NIRS. It measures the attenuation of the light at several wavelengths. From the ratio of this attenuation the oxygenation can be calculated. This can also be used in PA. If several wavelengths are used to generate the PA-waves, the oxygenation can be determined from the ratio of the amplitudes of the waves. In this research we have not used PA to determine the oxygenation.

Detection method

In LDF and NIRS a very similar detection scheme is used. Both make use of laser diodes. The difference is that LDF requires single-mode laser-diodes to have sufficient coherence length (see also chapter 4). NIRS does not have special requirements for these laser-diodes, so also a stack of diodes can be used, providing larger laser power. In both techniques fibers are used to deliver light from laser-diodes to the tissue. In NIRS the DC-component of the backscattered light at several wavelengths is analysed, whereas in LDF the AC-component of

the light is analysed. As these methods look very similar but measure different parameters, it is obvious to combine these two methods.

The PA method is very different from the other two methods. It is a hybrid technique, using pulsed light to generate acoustic waves, whereas the other two methods are purely optical. Furthermore, PA is able to measure locally where the other methods are measuring in a much larger volume (Figure 6.1).

In Table 6.1 the main characteristics of the three methods are compared, showing the complementary of the three methods. In this table a plus (+) indicates that this technique is capable of measuring this parameter, while a minus (-) indicates that this parameter cannot be measured. In case of sensitivity a plus (+) means that the technique is able to measure locally in the mentioned direction.

Table 6.1 *Comparison of capabilities of LDF, PA, and NIRS.*

	(pulsed-) laser Doppler flowmetry *LDF*	*Photoacoustics* *PA*	*Near-infrared spectroscopy* *NIRS*
Flow/perfusion	++	-	-
Blood content	+/-	++	+
Oxygenation	-	-	++
Depth sensitivity	+/-	++	+/-
Lateral sensitivity	-	++	-

6.2 Design

Based on the complementarity of the three methods, as described in the previous paragraph, a design of prototype of a combined probe will be presented in this section.

As mentioned in the previous paragraph, NIRS and LDF look very similar. Since they both make use of fibers for light delivery and detection, these fibers can easily be combined into one probe. In LDF a 400 μm diameter fiber is used, whereas in NIRS a fiber bundle is used. So the LDF fiber can be inserted into the NIRS fiber bundle. One cannot make use of a fiber bundle to detect Doppler scattered light, as each fiber will produce an independent speckle pattern on the photodetector. All these independent speckle patterns from the fibers inside the fiber bundle will overlap at the detector. This will result in a reduced modulation depth, i.e. a reduced signal-to-noise ratio. So for LDF a single fiber is required. In NIRS just the DC intensity on the photodetector is measured. This information will be maintained when using a fiber bundle.

The PA probe consists of one or more fibers for light delivery together with a piezoelectric element and amplifiers for detection of the ultrasound (see also chapter 2). This is very different from the other two methods.

We propose to develop a combined probe, based on a flexible base material (size about 5 x 8 cm), which can be placed on top of the head. The flexible base can be formed according to the shape of the skull and after that fixated to the head. This base will contain 3 fiber holders in which one source fiber and 2 detector fibers can be placed. Furthermore, there will be a slit in which the PA probe can be positioned. The PA probe can then be moved through this slit over the brain surface to probe different regions in the brain. A schematic drawing of the combined probe is shown in Figure 6.2.
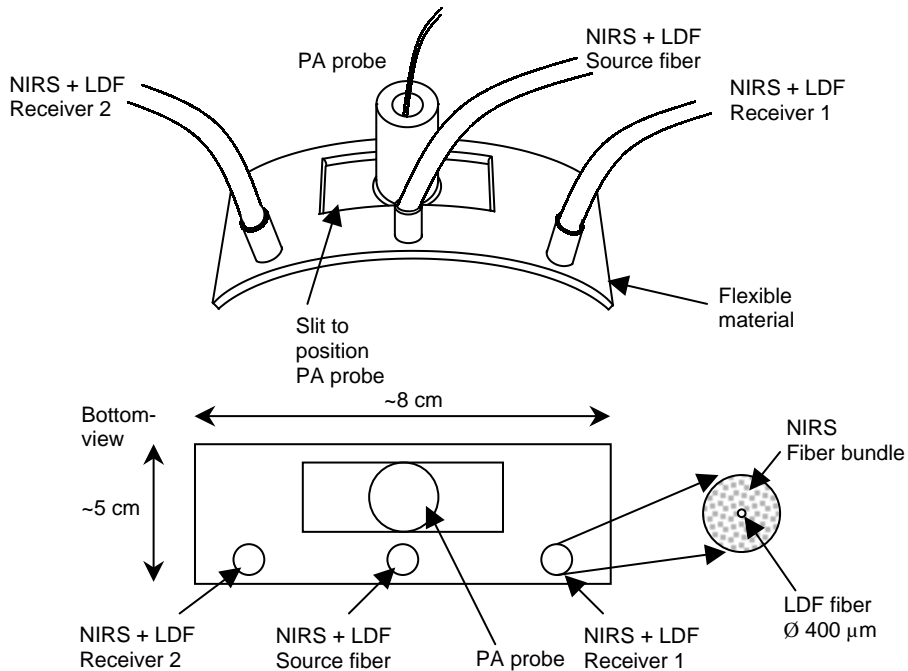
Figure 6.2 *Drawing of a near-infrared/photoacoustic probe for combined non-invasive measurement of cerebral perfusion, oxygenation and blood volume. This probe combines NIRS, LDF and PA.*

All three instruments make use of pulsed light. It has to be avoided that the instruments influence each other. The wavelengths are all in a region of about 700-900 nm. An option is to use optical filters in LDF and NIRS that block the light from the other two instruments. PA will not be influenced by NIRS and LDF as the pulse energies of those instruments are too low to generate PA waves.

Another option is to make the instruments measuring alternating, like was done with NIRS and LDF during the measurements described in chapter 5.
The design of Figure 6.1 combines only the probes of the three techniques and not the instruments themselves. So the light source, detection, and signal processing will still be based on the separate instruments.

The measurement volume of NIRS and LDF is about equal. Using NIRS one obtains information about the oxygenation and total hemoglobin concentration (tHb), i.e. blood content. In LDF mainly the average red blood cell velocity (<RBC-velocity>) is determined. Using LDF at large fiber distances one will not be able to determine changes in red blood cell concentration, as all photons will be Doppler shifted. The information about the blood content obtained by NIRS, and information about the average RBC-velocity obtained by LDF can be used to determine the flow:

$$Flow_{combined-instrument} \sim tHb_{NIRS} \times < RBC - velocity >_{LDF} . \qquad (6.1)$$

So the advantage of combining NIRS and LDF is that together they are able to determine changes in blood flow, whereas the separate instruments could only detect changes in RBC-velocity or blood content and oxygenation.
Using PA one is able to measure local changes in blood content. This information can be used to get better insight in which regions do suffer from a lack of blood. Also it can be used to monitor the occurrence of bleedings in a well-defined region.

A second more advanced version of the combined probe should be made more compact. In the presented design of the probe the NIRS and LDF fibers are placed perpendicular on the tissue-surface. To improve the stability during the measurements, it is preferably to have the fibers perpendicular to the tissue surface, as is already used with NIRS measurements in clinical situations. The stability of the probe can be further improved by designing more compact PA-sensors. Instead of one sensor, then also a linear array of PA-sensors can be used, providing an image of the blood content at a given cross section in the brain.
In the ideal case, all fibers and the PA sensor are integrated in a flexible material with a thickness of several millimeters. Then the probe can be formed according to the shape of the head and can be fixed to the skin. As then there are no parts that stick out of the base material, the position of the probes will be maintained during movements of the patient.

7 Conclusions and outlook

In this chapter the final conclusions of the research described in this thesis are presented. An outlook to future improvements and applications of the instruments will be given.

7.1 **Conclusions**

We have designed and constructed a double ring photoacoustic senor with a very narrow opening angle. This sensor has a very narrow opening angle of 3º for photoacoustic sources that generate signals with peak-to-peak times of 67 ns. Using cross-correlation techniques the effect of side-lobes could be suppressed significantly. Furthermore the opening angle was further reduced to 1.7º. This resulted in a sensor with a pronounced forward directed sensitivity.

With this sensor we were able to image blood vessel in phantoms and *in vivo*. Using the model of a spherical photoacoustic source, the circular cross-section of artificial blood vessels was outstandingly well reconstructed. The diameter of artificial blood vessels estimated with photoacoustics has been found to correlate well with the real diameter.

In *in vivo* experiments we proved that the photoacoustic signal is predominantly generated by blood inside the vessel and not by the vessel wall. Furthermore it has been shown that changes in vessel diameter can be measured. Branching of blood vessels *in vivo* has been imaged.

A pulsed-laser Doppler flowmetry (LDF) method is developed which has the advantage over continuous wave LDF that a higher peak power can be applied to the tissue. As a result it enables deep perfusion probing.

In Monte-Carlo light scattering simulations we showed that with increasing separation between points of illumination and detection the fraction of Doppler shifted photons rapidly increases to 100%. As a consequence it will not be possible to detect changes in red blood cell concentration anymore. Nevertheless, it will still be possible to monitor changes in average red blood cell velocity.

We have shown that changes in average red blood cell velocity can be measured with LDF. The results of these LDF measurements correlated well with the flow measured in the carotid artery. In these experiments it was shown that no changes in concentration could be observed at relatively large fiber distances. Furthermore, we showed that LDF can add information about average red blood cell velocity to data obtained with the NIRS measurements. In this way information can be obtained about oxygenation, blood content as well as blood flow in the brain in a non-invasive way.

A blood vessel in the upper part of the brain has been visualised with photoacoustics. The diameter and position of this vessel were in agreement with a Doppler-ultrasound measurement. Furthermore we were able to detect changes in the position of this blood vessel due to a filling of the brain, in a situation where an artificial fontanel was created in the skull. However, this will not be possible in a real situation where the brain is embedded in a rigid structure.

A balloon catheter filled with an optically high absorbing fluid ($\mu_a \gg \mu_{a,blood}$) has been detected in real brain up to a depth of 8 mm, when using an energy of 1 mJ/pulse.

7.2 Outlook

The sensitivity of the photoacoustic sensor can be improved if the sensor is pre-focused at a certain measurement depth. This pre-focusing can be carried out using a curved sensor surface, as is shown in Figure 7.1.
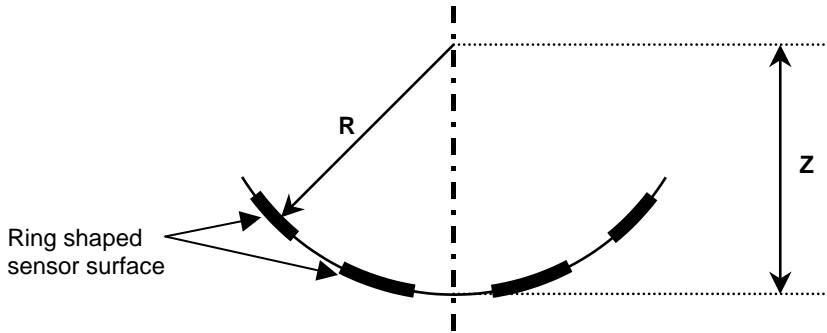

Figure 7.1 *Pre-focused double ring transducer; curvature of sensor surface matches with focusing depth Z.*

The radius R of the curvature of the sensor surface determines the focusing depth Z. All signals originating from sources, located on the centerline of the sensor, at this depth will arrive at the same time at both ring-shaped sensor surfaces. Due to the curvature, there will be no destructive interference on the rings, which enables an enlargement of the sensor surfaces. This enhances the sensitivity of the photoacoustic sensor. For depths different from the focusing depth Z, destructive interference of the acoustic waves will occur at the sensor surface, limiting the sensitivity. So this enhancement of the sensitivity can only be used when the depth at which one wants to measure is known.

The ring-shaped sensor surface can be split in two half rings. When a photoacoustic source is located off-axis of the sensor centerline, then the half-ring at the side of the source will detect the largest signal. In this way it can be distinguished at which side of the centerline of the sensor a source is located. An even better approach will be to divide the ring in 4 quarters. Then it can be determined in which quadrant the source is located. Furthermore this can be used to determine if a source is really located exactly on the centerline. In this case all 4 quadrants of the sensor will detect a signal with equal shape and amplitude.

The cross-correlation algorithm can be extended, in order that it can be used to estimate the actual sound velocity in the tissue, i.e. corrected for inhomogeneities in the tissue. If the sensor surface of both rings is split in 4 quadrants, it can be determined whether a source is located exactly on the centerline. When the source is located on the centerline, the zero-time cross-correlation value can be optimized by adjusting the sound velocity. So the actual sound velocity in the tissue can be determined. This value can then be used in further signal processing.

In the research described in this thesis we have approximated the photoacoustic signals of blood vessels (cylindrical sources) with a model of a spherical source. The obtained results are quite satisfactory, although it is expected that these results can even be better if a model for a cylindrical source is used.

In the experiments described in chapter 5, NIRS is used to determine the oxygenation in the brain. This technique has a large measurement volume. If the photoacoustic measurements are extended with more wavelengths (photoacoustic spectroscopy), then it will be possible to determine the oxygenation locally, i.e. in a very small measurement volume. The distance the sound travels from the photoacoustic source to detector is not dependent on the excitation wavelength of the source. So all acoustic waves will suffer from identical acoustic attenuation. The amount of light reaching the photoacoustic source is dependent on the optical properties of the tissue, which is dependent on the wavelength. If we assume that we can predict the behavior of the scattering as a function of wavelength and that the absorption as a function of wavelength is known (mainly absorption by blood), then it will be possible to determine an *absolute* value for the oxygenation. This will be a large improvement of existing techniques like NIRS, which can detect *changes* in oxygenation only.

When one is able to measure the concentration of oxy- and de-oxyhemoglobin with photoacoustic spectroscopy, in principle also the concentration of other tissue constituents like e.g. glucose can be measured.

As mentioned in chapter 6, the detection scheme of NIRS and LDF is very similar. The photoacoustic method is very different from NIRS and LDF. So a logical step will be to combine LDF and NIRS into one instrument. In this instrument LDF will add information about the average velocity of red blood cells to the information obtained with NIRS.

The pulsed LDF-instrument described in chapter 4 enables deep perfusion probing. When more powerful laser diodes become available, and when the sensitivity of this instrument is further optimized, it will be possible to monitor

continuously the brain perfusion through the skull. This can provide important information in critical care patients about regions in their brain suffering from an impaired perfusion.

In this research we evaluated the ability of photoacoustics to determine changes in blood content by measuring changes in vessel diameter. As this vessel diameter could be determined satisfactory, photoacoustics can also be used in situations that require exact information about the inner diameter of a blood vessel. This can e.g. be in treatment of varicose veins, or after balloon angioplasty to determine if restenosis occurs.

Photoacoustics can also be used for tumor detection. The growth of tumors is attended with the growth of a dense blood vessel network around it (angiogenesis). This dense vessel-network can be detected with photoacoustics in an early stage of tumor development. This makes photoacoustics a powerful tool for cancer-detection in e.g. mammography.

Summary

In medicine there are situations that require continuous bedside monitoring of perfusion and blood volume. Such a situation can occur when children are born prematurely. Those children have a high risk to develop a handicap, which is most likely caused by cerebral damage due to impaired brain perfusion. Monitoring cerebral perfusion can provide information for preventive treatment. In this thesis we have explored the potential of photoacoustics and laser Doppler flowmetry for measurement of changes in blood content and blood flow respectively. An introduction into photoacoustics and laser Doppler flowmetry together with clinical applications is given in chapter 1.

In chapter 2 a background on photoacoustic detection is given, followed by the design of a double-ring photoacoustic sensor. This sensor has a very narrow opening angle of 3° for photoacoustic sources that generate signals with peak-to-peak times of 67 ns. We have shown that this can be further improved using the cross-correlation between the signals of inner and outer ring at zero time shift as weight factors. The opening angle of the sensor is then further reduced to 1.7°. Furthermore it suppresses the effect of sources located off-axis of the sensor. The calculated sensor responses have been verified experimentally. A non-contact optical method for detecting photoacoustic signals is developed, based on a dual-polarization interferometer.

Chapter 3 deals with photoacoustic measurements in phantom as well as in *in vivo* experiments. The selection of a suitable photoacoustic phantom is described. Imaging of artificial blood vessels with various diameters showed that the cross section of the vessels could be reconstructed nicely. We showed that the vessel diameter could be determined from these images. *In vivo* imaging in a rabbit ear demonstrated that changes in vessel diameter could be detected while repeatedly the vessel was occluded and opened. Flushing with saline proved that the photoacoustic signal is predominantly generated by blood inside the vessel and not by the vessel wall. Branching of blood vessels in a rabbit ear as well as in a human arm has been visualised using photoacoustics.

In chapter 4 a pulsed-laser Doppler Flowmetry (LDF) set-up is described. The advantage of pulsing a laser diode is that high peak-powers are allowed without exceeding the safety-limits. We proved that pulsing the laser diode did not affect the results of the LDF measurement. Thus pulsed-LDF enables increasing the spacing between the locations of illumination and detection. Therefore the measurement volume can be enlarged enabling deep perfusion

probing. The effect of increasing spacing between locations of illumination and detection on the LDF measurement has been investigated using Monte-Carlo light scattering simulations. Based on these measurements and simulations a design for a more sophisticated pulsed-LDF set-up is presented.

In chapter 5 we describe experiments in which the combination of results obtained by near-infrared spectroscopy (NIRS), and laser Doppler flowmetry (LDF) or photoacoustics (PA) is explored. These experiments were carried out on the microcirculation in the brain of a piglet. During these experiments the cerebral perfusion has been distorted by inducing hypercapnia (i.e. increased arterial carbon dioxide concentration), closing the carotid arteries and flushing the brain with saline. Photoacoustic images of a blood vessel in the top part of the brain are compared with Doppler ultrasound images.

In chapter 6 the complementarity of the three methods, used in chapter 5, is discussed. Based on this complementarity a design of a combined probe is presented.

Finally in chapter 7 the main conclusions are summarized and an outlook to future developments is given.

Foto-akoestisch & gepulste-laser Doppler monitoren van bloed concentratie en doorbloeding in weefsel

Samenvatting

In de geneeskunde zijn er situaties die een continue meting van doorbloeding en hoeveelheid bloed vereisen. Zo'n situatie kan ontstaan wanneer kinderen prematuur (na minder dan 37 weken zwangerschap) geboren worden. Deze kinderen lopen een groot risico een handicap te ontwikkelen, veroorzaakt door hersenschade ten gevolge van slechte doorbloeding van de hersenen. Het continue meten van de doorbloeding van de hersenen kan belangrijke informatie opleveren voor preventieve behandeling. In dit proefschrift hebben we onderzocht of het mogelijk is om fotoakoestiek en laser Doppler flowmetry te gebruiken om veranderingen te meten in respectievelijk hoeveelheid bloed en stroming van het bloed. In het eerste hoofdstuk worden fotoakoestiek en laser Doppler flowmetry geïntroduceerd en worden klinische toepassingen beschreven.

In hoofdstuk 2 wordt de achtergrond van fotoakoestische detectie beschreven, gevolgd door het ontwerp van een dubbele-ring fotoakoestische sensor. Deze sensor heeft een zeer kleine openingshoek van 3º, voor fotoakoestische bronnen die signalen genereren met een piek-tot-piek tijd van 67ns. We hebben laten zien dat dit kan worden verbeterd door de kruiscorrelatie op tijdverschuiving nul, tussen de signalen van de binnenste en buitenste ring, te gebruiken als gewichtsfactoren. De openingshoek van de sensor wordt dan verder verkleind tot 1.7º. De bijdrage van fotoakoestische bronnen die niet op de as van de sensor liggen wordt zo onderdrukt. De berekende eigenschappen van de sensor zijn experimenteel geverifieerd. Een optische detectie methode is ontwikkeld gebaseerd op een dubbele-polarisatie interferometer. Deze methode kan fotoakoestische signalen meten zonder mechanisch contact met het weefsel.

Hoofdstuk 3 behandelt fotoakoestische metingen in fantomen en in *in vivo* experimenten. De selectie van een geschikt fotoakoestisch fantoom is beschreven. Met het afbeelden van kunstmatige bloedvaten met verschillende diameters hebben we laten zien dat de doorsnede van deze vaten goed gereconstrueerd kon worden. De diameter van deze vaten kon worden bepaald uit de plaatjes. Veranderingen in bloedvat diameter zijn gemeten in het oor van een konijn, terwijl dit vat afwisselend dichtgedrukt en geopend werd. Door een bloedvat te spoelen met fysiologisch zout hebben we bewezen dat het

fotoakoestisch signaal voornamelijk wordt gegenereerd door bloed in het bloedvat en niet door de vaatwand. De splitsing van bloedvaten in een konijnenoor en in een menselijke pols zijn afgebeeld met fotoakoestiek.

In hoofdstuk 4 is een gepulste-laser Doppler flowmetry (LDF) opstelling beschreven. Het voordeel van het gebruiken van een gepulste laser-diode is dat er hoge piek-vermogens gebruikt kunnen worden zonder dat de veiligheidslimieten worden overschreden. We hebben laten zien dat het gebruik van een gepulste laser-diode het resultaat van de LDF metingen niet beïnvloedt. Het is nu dus mogelijk om met gepulste-LDF de afstand tussen de locaties van belichting en detectie te vergroten. Hierdoor zal het meetvolume toenemen, wat het mogelijk maakt om ook informatie te verzamelen over doorbloeding op grotere diepte. Het effect van een toename van de afstand tussen de belichting en detectie locaties is onderzocht met behulp van Monte-Carlo lichtverstrooiings-simulaties. Een ontwerp voor een toekomstig gepulste-LDF apparaat is beschreven, gebaseerd op de metingen en simulaties die gedaan zijn.

In hoofdstuk 5 zijn experimenten beschreven waarin de combinatie van nabij-infrarood spectroscopie (NIRS) en laser Doppler flowmetry (LDF) of fotoakoestiek is onderzocht. Deze experimenten zijn uitgevoerd op de doorbloeding in de hersenen van een biggetje. De doorbloeding is gedurende deze experimenten gewijzigd door een hypercapnie aan te brengen (verhoogde koolstofdioxide concentratie in het bloed), door het sluiten van de carotiden (halsslagaders) en door het spoelen met fysiologisch zout. Met behulp van fotoakoestiek hebben we een bloedvat in de hersenen afgebeeld. Dit plaatje is vergeleken met een plaatje gemaakt met een kleuren-Doppler ultrageluid apparaat.

In hoofdstuk 6 zijn de overeenkomsten van de drie methodes die we in hoofdstuk 5 hebben gebruikt beschreven. Gebaseerd op deze overeenkomsten is een ontwerp gemaakt voor een gecombineerd meetinstrument.

Tenslotte zijn de belangrijkste conclusies samengevat in hoofdstuk 7 en wordt een blik geworpen op toekomstige ontwikkelingen.

Nawoord

Het werk dat beschreven is in dit proefschrift, doe je natuurlijk niet alleen. Daarom wil ik op deze plaats graag iedereen bedanken die op enige wijze heeft bijgedragen aan de totstandkoming van dit proefschrift. Het is niet mogelijk om iedereen te noemen, maar een aantal mensen wil ik toch graag even apart noemen. Allereerst Frits, als dagelijks begeleider was je altijd bereikbaar voor vragen. Je enthousiasme was een belangrijke drijfkracht in het project.

Jan, als promotor heb je met je kritische blik ervoor gezorgd dat tijdens het schrijven van dit proefschrift de puntjes op de i werden gezet.

Erwin, als technicus op dit project heb je ervoor gezorgd dat ik de metingen kon doen door telkens weer de nodige elektronica en programmatuur te leveren. Je inbreng tijdens experimenten en de gezellige sfeer heb ik erg gewaardeerd.

René en Wiendelt, jullie inbreng in de vorm van adviezen en nuttige discussies tijdens metingen en werkbesprekingen hebben voor een belangrijk deel bijgedragen aan het succes van de experimenten.

Christoph, als grondlegger van de fotoakoestiek in Twente, heb jij me aan het begin van mijn project wegwijs gemaakt in de fotoakoestiek.

Met de mensen uit de Biomedische Optica groep, Alexei, Andrei, Anna, Ester, Folkert, Johan, Magdalena, Sasha, Srirang en Ton, heb ik de afgelopen jaren met veel plezier samengewerkt.

De samenwerking met onze projectpartners van het Universitair Kinderziekenhuis St. Radboud in Nijmegen, John, Jeroen en Han heb ik als erg prettig ervaren. Zij hebben gezorgd voor de klinische kant in ons project en zonder hun inbreng waren de dierexperimenten niet mogelijk geweest.

Het afstudeerwerk van Ralph, Marloes, Paul, Alma, Hylke, Cecile, Rik en Sven heeft voor een belangrijk deel bijgedragen aan de totstandkoming van dit proefschrift.

Sylvia, als centraal aanspreekpunt, "woman who has all the answers", heb je gezorgd voor de benodigde hoeveelheid kantoorartikelen, het regelen van reizen naar conferenties, maar ook voor een flinke dosis gezelligheid.

Frans was altijd bereid tot het verrichten van allerlei hand-en-spandiensten, Kirsten en Yvonne hebben gezorgd voor de ondersteuning in het chemisch lab.

En natuurlijk wil ik graag alle BFT-ers bedanken voor de prettige sfeer in de vakgroep.

Mijn ouders, Marloes en Bjorn wil ik bedanken voor hun interesse in mijn werk gedurende de afgelopen jaren.

<div align="center">

Bedankt!

Roy.

</div>

Curriculum vitae

Roy Kolkman werd geboren op 22 juli 1974 te Lichtenvoorde. In 1991 behaalde hij zijn HAVO diploma aan het Marianum te Groenlo, gevolgd door het VWO diploma in 1993. Hij studeerde van 1993 tot 1998 Technische Natuurkunde aan de Universiteit Twente. Het afstudeeronderzoek werd verricht bij de leerstoel Bio-Fysische Techniek (BFT). Dit onderzoek omvatte het bestuderen van lichtverstrooiingsgedrag van gedeformeerde rode bloedcellen. Onder leiding van dr. ir. F.F.M. de Mul en prof. dr. J. Greve is hij in 1998 begonnen aan een OIO-project, gefinancierd door de Technologiestichting STW. Het onderzoek, in samenwerking met het Klinisch Fysisch Laboratorium van het Universitair Kinderziekenhuis St. Radboud in Nijmegen, betrof het ontwikkelen van een instrument dat veranderingen in doorbloeding, bloedvolume en oxygenatie in één keer kan meten. De resultaten van dit werk leidden tot dit proefschrift.